

# UNIVERSITY OF NAPLES FEDERICO II

Department of Structures  
for Engineering and Architecture



*Master of Science in Structural and Geotechnical Engineering*

*Candidate:*

*Massimino Gnazzo (matr. M56000930)*

***Design optimization of high-rise buildings equipped  
with Shear Link Bozzo (SLB) devices using the PBSD approach***

Master's Degree Thesis  
Academic Year 2021/2022

*Supervisor:*

*Prof. Eng. Giorgio Serino*

*Co-supervisors:*

*Prof. Eng. Luis Bozzo*

*Dr. Eng. Rodrigo Alva*

---

## ABSTRACT

Over the past decades, the number of applications of earthquake-resistant devices, such as passive control systems, has steadily increased in civil engineering due to their ability to provide higher levels of safety to the structure. As an example, Shear Link Bozzo (SLB) devices, metallic dampers belonging to the family of passive energy dissipation systems, are widely used. These devices are used for new and retrofitted reinforced concrete and steel buildings, especially in America (e.g., Mexico, Perú, Ecuador). This thesis, developed during the Erasmus Traineeship at the engineering company “Luis Bozzo Estructuras y Proyectos S.L.” in Barcelona, Spain, deals with the optimization of the structural design of reinforced concrete buildings equipped with Shear Link Bozzo (SLB) devices. The use of SLB devices increases the stiffness of the structure, reducing the interstory drift during an earthquake and providing an additional source of energy dissipation, reducing the structural damage in both structural elements (e.g., beams and columns) and non-structural components. The aim of the study is to highlight the benefits associated with the application of the SLB devices to the seismic structural behavior and, furthermore, to evaluate the advantages of the Performance Based Seismic Design Approach (PBSD) over prescriptive building codes. For this purpose, the design of the entire structure is carried out considering the addition of SLB devices. Alternately, a simulated design of the bare frame structure, without seismic protection devices, is carried out with the aim of comparing the pros and cons of the two proposed solutions.

Chapter 1 introduces the topic of seismic protection of buildings through the use of various types of dissipation devices (passive energy dissipation systems, semi-active and active systems).

Chapter 2 deals with passive energy dissipation systems. The basic principles of these devices and their classification are introduced, with a more detailed focus on metallic dampers such as the Shear Link Bozzo devices.

Chapter 3 describes the main features of the SLB devices. The main results of the experimental campaigns of the four SLB generations are presented, which have led to the definition of a design table containing the mechanical properties of the proposed

---

devices. In particular, tests concerning the last generation devices, where the ultimate displacement is approximately 60 mm, show a much higher deformation capacity, thus energy dissipation, compared to previous generations.

Chapter 4 is dedicated to the modelling and design methods of SLB. First, the physical and mathematical modelling of the SLB device and the support, generally consisting of decoupled reinforced concrete walls or steel braces, is presented and then the corresponding finite element modelling is described. The design of the dissipator is generally conducted by means of *linear response spectrum analyses* (RSA) with two different methods: the direct iteration method and the inverse interaction method. The design of SLB involve iterative procedures. Changing the devices properties alter the stiffness of the structure and require recalculating the seismic forces on the structure accordingly to a RSA. For this reason, nonlinear time history analyses are highly recommended to verify the structural behavior of the building equipped with SLB.

Chapter 5 presents the main aspects of PBSD. This approach allows to make exceptions to specific prescriptive code-based approaches, so the focus of the structural design changes from a prescriptive “check list” of code provisions to a verification of building performance required at multiple seismic hazard levels using linear and advanced nonlinear analyses. Therefore, PBSD stands in contrast to common analysis and design methodologies such as *Equivalent Lateral Force* (ELF) analysis and *Response Spectrum analysis* (RSA) and results very useful especially for high-rise buildings.

Chapter 6 is dedicated to the geometric and mechanical nonlinear modelling of reinforced concrete structures. The various types of models for plastic hinges are introduced, focusing mainly on distributed and concentrated plasticity models, the most frequently used for nonlinear analyses. The importance of P- $\Delta$  effects and their influence in the analysis of structures is illustrated, taking as example a simple one-degree-of-freedom structure. Finally, the main theoretical aspects of linear and nonlinear dynamic analyses are introduced, including numerical integration methods and the damping modelling by means of the Rayleigh damping method.

Chapter 7 describes the case study of the thesis: a new high-rise reinforced concrete building located in Acapulco, Mexico. Firstly, the design of the SLB devices is carried out using the direct and inverse iteration methods in order to define the optimal

---

dimensions of the dissipators. Then, the design of the steel reinforcement and the verification of the structure is carried out using the performance PBSB by ensuring that the global and local acceptance criteria of the building codes are met. Finally, a comparison between the bare frame structure and the structure equipped with SLB is made, highlighting the pros and cons of the two proposed solutions.

Chapter 8 is dedicated to the conclusions of the thesis.



---

**LIST OF CONTENTS**

<b>1</b>	<b><i>Introduction</i></b>	<b>1</b>
<b>2</b>	<b><i>Passive Energy Dissipation Systems</i></b>	<b>3</b>
2.1	<b>Introduction</b>	<b>3</b>
2.2	<b>Basic principles</b>	<b>3</b>
2.2.1	Energy balance equation	6
2.3	<b>Classification of PED systems</b>	<b>9</b>
2.4	<b>Metallic dampers</b>	<b>12</b>
2.4.1	Adas damper	12
2.4.2	Buckling Restrained Brace (BRB) device	14
2.4.3	Shear Link device	16
<b>3</b>	<b><i>Shear Link Bozzo Device</i></b>	<b>18</b>
3.1	<b>Description of the Shear Link Bozzo (SLB) device</b>	<b>19</b>
3.2	<b>Experimental campaign of SLB Device</b>	<b>22</b>
3.2.1	First generation	22
3.2.2	Second generation	27
3.2.3	Third generation	32
3.2.4	Fourth generation	38
3.3	<b>Design table for Shear Link Bozzo device</b>	<b>41</b>
<b>4</b>	<b><i>Modelling and Design of SLB Device</i></b>	<b>43</b>
4.1	<b>SLB device mathematical modelling</b>	<b>43</b>
4.2	<b>SLB device finite element modelling</b>	<b>45</b>
4.2.1	Wen plasticity model	46
4.2.2	Link properties	47
4.3	<b>Iterative design methodology</b>	<b>49</b>
4.3.1	Direct iteration method	50
4.3.2	Inverse iteration method	52
<b>5</b>	<b><i>Performance Based Seismic Design Approach</i></b>	<b>56</b>
5.1	<b>Introduction</b>	<b>56</b>
5.2	<b>Performance objectives and levels</b>	<b>56</b>
5.3	<b>Acceptance criteria in ASCE 41-13</b>	<b>58</b>

<b>5.4</b>	<b>Site specific seismic hazard assessment</b>	<b>61</b>
5.4.1	Site response spectra	61
5.4.2	Time series record selection	62
<b>5.5</b>	<b>PBSD approach procedure</b>	<b>65</b>
<b>6</b>	<b><i>Nonlinear Modelling of Structures</i></b>	<b>69</b>
<b>6.1</b>	<b>Fiber modelling approach</b>	<b>70</b>
6.1.1	Fiber model for RC beams	71
6.1.2	Fiber model for RC columns	72
6.1.3	Fiber model for walls	73
6.1.4	Limitations of fiber models (Graham H. Powell, 2010)	73
6.1.5	Inelastic shear behavior in beams and columns	74
<b>6.2</b>	<b>Plastic hinge modelling approach</b>	<b>75</b>
6.2.1	Plastic hinge model for RC beams	75
6.2.2	Plastic hinge model for RC columns	76
6.2.3	Moment-Rotation relationship in ASCE 41-13	78
<b>6.3</b>	<b>Nonlinear time-history analysis</b>	<b>81</b>
6.3.1	Proportional damping	82
6.3.2	Time integration parameters	83
6.3.2.1	Newmark method	83
6.3.3	Geometric nonlinearity	85
6.3.3.1	P- $\Delta$ effect	85
<b>7</b>	<b><i>Case Study: Baia Project</i></b>	<b>90</b>
<b>7.1</b>	<b>Description of the building</b>	<b>90</b>
<b>7.2</b>	<b>Reference code</b>	<b>92</b>
7.2.1	Code requirements	92
<b>7.3</b>	<b>Load combinations</b>	<b>94</b>
7.3.1	Gravity loads	94
7.3.2	Seismic loads	95
7.3.2.1	Site response spectra	95
7.3.2.2	Time Series record selection	101
<b>7.4</b>	<b>Modelling assumptions for the analyses</b>	<b>104</b>
<b>7.5</b>	<b>Bare frame structure design</b>	<b>107</b>
7.5.1	Modal analysis	107
7.5.2	Service Level Earthquake evaluation	108

---

7.5.3	Considerations of wind demand	109
7.5.4	Reinforcement design	110
7.5.5	MCE analyses results	112
<b>7.6</b>	<b>Structure with SLB design</b>	<b>116</b>
7.6.1	SLB design	116
7.6.2	Modal analysis	120
7.6.3	Service Level Earthquake evaluation	121
7.6.4	Reinforcement design	121
7.6.5	MCE analyses results	123
<b>7.7</b>	<b>Comparison of Bare frame structure and Structure with SLB</b>	<b>129</b>
7.7.1	Structural behavior comparison	129
7.7.2	Economic comparison	135
<b>8</b>	<b>Conclusions</b>	<b>140</b>
	<b>References</b>	<b>141</b>
	<b>Acknowledgements</b>	<b>143</b>

---

**LIST OF FIGURES**

<i>Figure 2.1 Effect of Energy Dissipation Systems on Force-Deformation curves of a structure</i>	5
<i>Figure 2.2 Scheme of a Passive Control System</i>	6
<i>Figure 2.3 Structural scheme for energy balance equation</i>	6
<i>Figure 2.4 Idealized force-displacement loops of hysteretic energy dissipation devices</i>	9
<i>Figure 2.5 Idealized force-displacement loops of viscoelastic energy dissipation devices</i>	10
<i>Figure 2.6 Idealized force-displacement loops of other energy dissipating devices</i>	10
<i>Figure 2.7 Implementation of PED in North America for seismic applications (Soong and Spencer, 2002)</i>	12
<i>Figure 2.8 Geometry of the device</i>	13
<i>Figure 2.9 Conventional localization of the connection in a frame</i>	13
<i>Figure 2.10 ADAS (left) and TADAS (right) device</i>	14
<i>Figure 2.11 ADAS and TADAS force-displacement relationship, 1<sup>st</sup> vs 100<sup>th</sup> cyclic load</i>	14
<i>Figure 2.12 BRB device</i>	15
<i>Figure 2.13 Force-displacement relationship of the BRB device</i>	15
<i>Figure 2.14 Details of BRB (Ozcelik et al., 2017)</i>	16
<i>Figure 2.15 Shear link device (left) and force-displacement relationship (right)</i>	17
<i>Figure 3.1 Traditional application with steel braces</i>	18
<i>Figure 3.2 SLB application with decoupled reinforced concrete walls</i>	18
<i>Figure 3.3 Geometry of Shear Link Bozzo device</i>	19
<i>Figure 3.4 Installation of 4<sup>th</sup> gen. SLB device in decoupled walls (left) and in chevron braces (right)</i>	19
<i>Figure 3.5 Working modes of SLB device: (a) shear and (b) bending, (Nuzzo et al., 2015)</i>	20
<i>Figure 3.6 Shear Link Bozzo typical hysteretic curves, (Nuzzo et al., 2015)</i>	20
<i>Figure 3.7 Fourth generations of SLB device</i>	21
<i>Figure 3.8 Prototype of the SLB 1<sup>st</sup> generation</i>	23
<i>Figure 3.9 Experimental force-displacement hysteretic curve (ISMES, 1997)</i>	23
<i>Figure 3.10 Dimensions of the SLB device</i>	24
<i>Figure 3.11 SL tested at ISMES, Italy (2001)</i>	24
<i>Figure 3.12 Von Mises stresses for the Dissip3SL30_2 and Disip4SL30_2 devices</i>	25
<i>Figure 3.13 Nonlinear monotonic force-displacement relationship</i>	25
<i>Figure 3.14 Experimental vs numerical monotonic force-displacement relationship</i>	27
<i>Figure 3.15 Hysteretic curve for device with (left) and without (right) slippage of the bolts</i>	27
<i>Figure 3.16 Geometry of the tested 2<sup>nd</sup> generation SLB device</i>	28
<i>Figure 3.17 Boundary condition for SLB devices</i>	29
<i>Figure 3.18 Monotonic test #4 damage scenario: (a) initial condition, (b) yielded phase, (c) onset of buckling, (d) global buckling</i>	29

Figure 3.19 Cyclic test #10 damage scenario: (a) initial condition, (b) yielded phase, (c) onset of tearing, (d) distribution of tearing	30
Figure 3.20 Example of cyclic and monotonic F-x curves obtained from tests	30
Figure 3.21 Stress distribution in FNF configuration: (a) principal maximum normal stress; (b) shear stress	31
Figure 3.22 Strain distribution at failure for FNF (left) and FF (right) configuration	32
Figure 3.23 Geometry of the reinforced concrete frame, UNAM laboratory	32
Figure 3.24 Geometry of 3 <sup>rd</sup> generation SLB device	33
Figure 3.25 Dimensions in mm (left) and SLB connection type 1 (right)	33
Figure 3.26 Dimensions in mm (left) and SLB connection type 2 (right)	34
Figure 3.27 Bare concrete frame, hysteresis curve (left) and skeleton curve (right)	34
Figure 3.28 Concrete frame with SLB connections type 1, hysteresis curve (left) and skeleton curve (right)	35
Figure 3.29 Concrete frame with SLB connections type 2, hysteresis curve (left) and skeleton curve (right)	35
Figure 3.30 Mesh configuration of FE model of the test	36
Figure 3.31 Load-displacement relationship of bare concrete frame - Experimental test vs numerical modelling	36
Figure 3.32 Comparison between experimental and numerical hysteresis loop of SLB connections type 1	37
Figure 3.33 Von Mises stresses for the SLB connection type 1	37
Figure 3.34 Comparison between spring supports and fixed supports in numerical model	38
Figure 3.35 Geometries of the devices proposed for the tests	38
Figure 3.36 Steel reinforcement details in the concrete wall	39
Figure 3.37 Experimental tests	40
Figure 3.38 Force-displacement relationship for SLB device (Bozzo et al., 2021)	41
Figure 4.1 Force-displacement relationship of the SLB device	43
Figure 4.2 Elasto-plastic force-displacement relationship	43
Figure 4.3 SLB device mathematical modelling	44
Figure 4.4 Scheme of the system device - decoupled concrete wall	45
Figure 4.5 Wen Plasticity Property Type for Uniaxial Deformation	46
Figure 4.6 Definition of parameters for the Wen Plasticity Property	47
Figure 4.7 SLB modelling as NLink element in ETABS	48
Figure 4.8 Assignment of the lateral stiffness of the Nlink for the local axis - ETABS	49
Figure 4.9 Flowchart for the design of SLB dissipators using DISSIPALB plugin for ETABS	50
Figure 4.10 Flow chart of direct iteration method	50
Figure 4.11 Direct iteration method - Dissipa plug-in for ETABS	51
Figure 4.12 Inverse iteration method - Dissipa plug-in for ETABS	52
Figure 4.13 Flow chart of inverse iteration method	54

Figure 5.1 Structural Performance Objective Illustration (Golesorkhi et al., 2019)	57
Figure 5.2 Performance Levels of Code-Based Buildings at Various Risk Category Levels as described in ASCE 41 (Golesorkhi et al., 2019)	58
Figure 5.3 Component Force vs Deformation Curves	59
Figure 5.4 Acceptance Criteria for Force-Deformation Relationships	61
Figure 5.5 Spectrally matched time series (Golesorkhi et al., 2019)	63
Figure 5.6 Spectrally scaled time series (Golesorkhi et al., 2019)	64
Figure 5.7 Typical flowchart of PBSO approach (Golesorkhi et al., 2019)	66
Figure 5.8 Equivalent viscous damping versus building height (TBI Guidelines, 2017)	67
Figure 6.1 Comparison of nonlinear model types for reinforced concrete element	70
Figure 6.2 Stress-strain curve for concrete (a) and steel (b) for uniaxial fiber model	71
Figure 6.3 Fiber section of a reinforced concrete beam (Powell, 2010, Mazhar H. et al., 2021)	72
Figure 6.4 Fiber section of a reinforced concrete column ((Powell, 2010, Mazhar H. et al., 2021)	72
Figure 6.5 Fiber section for in-plane bending behavior of a reinforced concrete wall	73
Figure 6.6 Plastic hinge model of a 2D frame subjected to lateral earthquake loading	75
Figure 6.7 Plastic hinge modelling of beams (Powell, 2010)	76
Figure 6.8 Yield surface for reinforced concrete columns (Powell, 2010)	77
Figure 6.9 Force vs. Deformation curve for the plastic hinge definition – Acceptance Criteria Illustration	78
Figure 6.10 ASCE 41 force-deformation relationship	80
Figure 6.11 Rayleigh damping	83
Figure 6.12 Average acceleration method - Newmark's method equations	84
Figure 6.13 Static scheme of the cantilever beam (CSI Reference Manual., 2017)	85
Figure 6.14 Moment diagrams for cantilever beam with and without P- $\Delta$ effect	86
Figure 6.15 Single degree of freedom model (Fenwick R.C. et al., 1992)	87
Figure 6.16 P- $\Delta$ effects in a structure subjected to monotonically increasing lateral displacement (Fenwick R.C. et al., 1992)	88
Figure 7.1 Bare frame 3D model	91
Figure 7.2 Plan of the building	91
Figure 7.3 Location of the study site in relation to the seismic regionalization of Mexico (MOC-CFE, 2015)	96
Figure 7.4 Site response spectrum - Design Earthquake Level	97
Figure 7.5 MCE, DBE and SLE site response spectra	98
Figure 7.6 Elastic design response spectrum	100
Figure 7.7 Design Response Spectra	101
Figure 7.8 MCE matched seismic signal 1	102
Figure 7.9 MCE matched seismic signal 2	102
Figure 7.10 MCE matched seismic signal 3	102
Figure 7.11 MCE matched seismic signal 4	103

Figure 7.12 MCE matched seismic signal 5	103
Figure 7.13 MCE matched seismic signal 6	103
Figure 7.14 MCE matched seismic signal 7	104
Figure 7.15 Acceleration response spectra of matched seismic signals	104
Figure 7.16 Concrete C45 - Material stress-strain relationship	106
Figure 7.17 Concrete C55 - Material stress-strain relationship	107
Figure 7.18 Steel A615Gr60 - Material stress-strain relationship	107
Figure 7.19 1 <sup>st</sup> mode	108
Figure 7.20 2 <sup>nd</sup> mode	108
Figure 7.21 3 <sup>rd</sup> mode	108
Figure 7.22 Max Interstory Drift at Service Level Earthquake (RSA)	109
Figure 7.23 Max Story Shears - Service Level Earthquake vs Wind Load	110
Figure 7.24 Subdivision of the beam for the reinforcement design	111
Figure 7.25 Damping coefficients for Nonlinear time history analysis - ETABS	113
Figure 7.26 Max interstory Drift at MCE level - Dir. X	114
Figure 7.27 Max Interstory Drift at MCE level - Dir. Y	114
Figure 7.28 Residual Interstory Drift at MCE level - Dir. X	115
Figure 7.29 Residual Interstory Drift at MCE level - Dir. Y	115
Figure 7.30 Example of the plastic hinge hysteretic cycle of a beam	116
Figure 7.31 Structure with SLB 3D model	117
Figure 7.32 Plan of the building	117
Figure 7.33 Decoupled wall FEM model - ETABS	117
Figure 7.34 1 <sup>st</sup> mode	120
Figure 7.35 2 <sup>nd</sup> mode	120
Figure 7.36 3 <sup>rd</sup> mode	120
Figure 7.37 Max Interstory Drift at Service Level Earthquake (RSA)	121
Figure 7.38 Damping coefficients for Nonlinear time history analysis - ETABS	124
Figure 7.39 Max interstory Drift at MCE level - Dir. X	125
Figure 7.40 Max Interstory Drift at MCE level - Dir. Y	125
Figure 7.41 Residual Interstory Drift at MCE level - Dir. X	126
Figure 7.42 Residual Interstory Drift at MCE level - Dir. Y	127
Figure 7.43 Example of plastic hinge hysteretic cycle	128
Figure 7.44 Example of SLB device hysteretic cycle	128
Figure 7.45 Max Interstory Drift - Service Level Earthquake (RSA)	130
Figure 7.46 Max Story Shears at SLE - Structure with and w/o SLB	132
Figure 7.47 Max Interstory Drift - Mean values for MCE level	133
Figure 7.48 Comparison of hysteretic cycles of the most stressed plastic hinges	134
Figure 7.49 Residual Interstory Drift - MCE	135

---

**LIST OF TABLES**

<i>Table 2.1 Summary of the main aspects of Passive Energy Dissipation systems (Constantinou et al., 2008)</i>	11
<i>Table 3.1 Design Table for 4th generation of Shear Link Bozzo devices</i>	42
<i>Table 5.1 Damage Control and Building Performance Levels from ASCE 41-13</i>	57
<i>Table 5.2 Examples of Possible Deformation-Controlled and Force-Controlled Actions</i>	60
<i>Table 5.3 Reinforced concrete effective stiffness values</i>	68
<i>Table 6.1 Modelling Parameters and Numerical Acceptance Criteria for</i>	80
<i>Table 6.2 Modelling Parameters and Numerical Acceptance Criteria for</i>	81
<i>Table 7.1 Geometric and mechanical properties of RC sections for Baia Project</i>	91
<i>Table 7.2 Seismic parameters values for the elastic design response spectrum</i>	99
<i>Table 7.3 Reinforced concrete effective stiffness values</i>	105
<i>Table 7.4 Modal analysis results for Bare frame structure</i>	108
<i>Table 7.5 Reinforcement design for Bare frame structure - Beam sections</i>	111
<i>Table 7.6 Reinforcement design for Bare frame structure - Column sections</i>	112
<i>Table 7.7 Mean and Maximum D/C ratios for Collapse Prevention (CP) - Bare structure</i>	116
<i>Table 7.8 Geometric and mechanical properties of decoupled concrete walls</i>	118
<i>Table 7.9 Design Table for 4<sup>th</sup> generation of Shear Link Bozzo devices</i>	119
<i>Table 7.10 Modal analysis results for SLB structure</i>	120
<i>Table 7.11 Reinforcement design for structure with SLB - Beam sections</i>	122
<i>Table 7.12 Reinforcement design for structure with SLB - Column sections</i>	123
<i>Table 7.13 Mean and Maximum D/C ratios for Collapse Prevention (CP) - Structure with SLB</i>	128
<i>Table 7.14 Modal analysis results comparison</i>	129
<i>Table 7.15 SLE Interstory Drift comparison</i>	131
<i>Table 7.16 Max Interstory Drift - Mean values for Maximum Considered Earthquake (MCE)</i>	133
<i>Table 7.17 Collapse Prevention D/C ratios for structure with and w/o SLB</i>	134
<i>Table 7.18 Material costs for Baia project</i>	135
<i>Table 7.19 Amount of concrete for the structures</i>	136
<i>Table 7.20 Amount of steel reinforcement for bare frame structure - beam sections</i>	137
<i>Table 7.21 Amount of steel reinforcement for bare frame structure - column sections</i>	137
<i>Table 7.22 Amount of steel reinforcement for structure with SLB - beam sections</i>	138
<i>Table 7.23 Amount of steel reinforcement for structure with SLB- column sections</i>	138
<i>Table 7.24 Reinforcement design comparison - Bare frame structure vs Structure with SLB</i>	138
<i>Table 7.25 Economic comparison between the two solutions</i>	139



# 1 INTRODUCTION

Historically, the aseismic design of structures has been based upon a combination of strength and ductility. For small and frequent seismic disturbances, the structure is expected to remain in the elastic range, with all stresses well below yield levels. However, it is not reasonable to expect that a traditional structure will respond elastically when subjected to a major earthquake. Instead, the design engineer relies upon the inherent ductility of buildings to prevent catastrophic failure, while accepting a certain level of structural and non-structural damage. This philosophy has led to the development of aseismic design codes featuring lateral force methods and inelastic design response spectra. With this approach the structure is designed to resist to an equivalent static load.

However, in recent years new and innovative concepts of structural protection have been advanced and are at various stages of development. Modern structural protective systems can be divided into three major groups (Constantinou et al., 1998):

- **Seismic isolation systems**

A seismic isolation system is typically placed at the foundation of the structure, and, thanks to its flexibility and energy absorption capability, it partially reflects and partially absorbs a part of the earthquake input energy before this one can be transmitted to the structure. The net effect is a reduction of energy dissipation demand on the structural system.

- **Passive energy dissipation systems**

Research and development of passive energy dissipation devices for structural applications have nearly 50 years history. The basic function of these devices, when incorporated into the superstructure of a building, is to absorb a portion of the seismic input energy thus reducing energy dissipation demand on primary structural members and minimizing possible structural damage. Unlike seismic isolation, these devices can also be effective against wind induced motions as well as those due to earthquakes.

- **Semi-active and Active systems**

Semi-active and active structural control is an area of structural protection in which the motion of a structure is controlled or modified by means of the action

of a control system through some external energy supply. The difference between semi-active and fully active systems is that the first type of devices cannot add energy to the structure.

This thesis work focuses mainly on passive energy dissipation systems with particular attention on metallic hysteretic devices, to which Shear Link Bozzo device belongs. For this reason, chapter 2 deals only with this type of devices where their basic principles and classification are introduced, with a more detailed focus on the Shear Link Bozzo device in chapters 3 and 4.

Chapter 5 presents the main aspects of Performance Based Seismic Design (PBSD) approach and its advantages if compared to the traditional prescriptive code-based approaches.

Chapter 6 is dedicated to the geometric and mechanical nonlinear modelling of reinforced concrete structures. In this chapter, the various types of models for plastic hinges are introduced, focusing mainly on distributed and concentrated plasticity models, the most frequently models for nonlinear analyses.

Chapter 7 describes the case study of the thesis: a new high-rise reinforced concrete building located in Acapulco, Mexico. The aim of the study is twofold: firstly, it is intended to highlight the benefits associated with the application of the Shear Link Bozzo devices to the structure and the advantages of using the Performance Based Seismic Design Approach instead prescriptive building codes. In addition, a comparison with the bare frame structure designed according to a traditional seismic approach is proposed.

Chapter 8 lists the conclusions of the thesis, highlighting the benefits in the employment of SLB device.

## **2 PASSIVE ENERGY DISSIPATION SYSTEMS**

### **2.1 Introduction**

This chapter presents the principles of operation of passive energy dissipation systems (Constantinou et al., 1998, Alehashem et al., 2008, Soong T.T. et al., 2002). Passive energy dissipation systems for seismic applications

have been under development for several years with a rapid increase in implementations starting in the mid of 1990s. The principal function of a passive energy dissipation system is to reduce the inelastic energy dissipation demand on the framing system of a structure. The result is reduced damage to the framing system. The most common devices used for seismic protection of structures include viscous fluid dampers, viscoelastic solid dampers, friction dampers and metallic dampers. The growth in application and development of passive energy dissipation devices has led to a number of publications that present detailed discussions on the principles of operation and mathematical modelling of such devices, analysis of structures incorporating such devices and their applications to various structural systems (e.g., Constantinou et al. 1998, Soong and Dargush 1997, Hanson and Soong 2001). In addition, a state of the art and state of the practice paper was published on the general topic of supplemental energy dissipation where passive and active structural systems were considered (Soon and Spencer 2002).

### **2.2 Basic principles**

In conventional seismic design, acceptable performance of a structure during earthquake shaking is based on the lateral force resisting system being able to absorb and dissipate energy in a stable manner for a large number of cycles. Energy dissipation occurs in specially detailed ductile plastic hinge regions of beams and columns at the base of the structure, which also constitute part of the gravity load carrying system. Plastic hinges are regions of concentrated damage to the gravity frame, which often is irreparable. This conventional design approach is based on the prevention of the structural collapse of the building and loss of human lives in case of strong earthquakes. There are situations in which the conventional design approach is

not applicable, for example when a structure must remain functional after an earthquake as in the case of important and strategic buildings (e.g., hospitals). In these cases, the structure may be designed with sufficient strength so that inelastic action is prevented or at least minimal, but this would be a very expensive approach. For this reason, alternative design procedures have been developed which incorporate earthquake protection systems, such as seismic isolation systems or additional energy dissipation devices, into the structure. The behavior and effects of these systems may be studied with the consideration of the distribution of energy within the structure. During a seismic event, a finite quantity of energy is input into a structure (Soong and Dargush, 1997). This input energy is converted into both kinetic and potential (strain) energy which must be either absorbed or dissipated through heat. Without damping vibrations would exist for all the time. In any case, in the structures there is always some level of intrinsic damping which withdraws energy from the system and therefore reduces the amplitude of vibration. To improve the structural performance is possible to insert some supplemental device into the structure that can absorb a portion of the input energy. This is made clear by considering the conservation of energy relationship (Uang and Bertero, 1988):

$$E = E_S + E_K + E_D + E_H \quad (2.1)$$

where, at a given instant in time  $t$ ,  $E$  is the absolute input energy from the earthquake motion,  $E_K$  is the absolute kinetic energy,  $E_S$  is the recoverable elastic strain energy stored by the structure,  $E_H$  is the irrecoverable energy dissipated by the structural system through its inelastic behaviour and  $E_D$  is the energy dissipated by supplemental damping devices. The absolute energy input  $E$  represents the work done by the total base shear force at the foundation of the structure. It, thus, contains the effect of the inertia forces of the structure.

In the conventional design approach, acceptable structural performance is accomplished by the occurrence of inelastic deformations. This assumption has two different effects, one direct and one indirect. The direct effect consists in an increase of energy  $E_H$ , meanwhile the indirect effect is that the occurrence of inelastic deformations results in softening of the structural system which itself modifies the absolute input energy from the earthquake. The increased flexibility of the structures acts as a filter which reflects a portion of the earthquake energy.

Another approach to improving earthquake response performance and damage control is that of supplemental energy dissipation systems. In these cases, mechanical devices are incorporated into the frame of the structure and dissipate energy throughout the height of the structure. In addition to increasing the energy dissipation capacity of the structure, some energy dissipation systems also increase the strength and the stiffness. These systems include the following types of energy dissipation devices: metallic-yielding, friction and viscoelastic. Viscous fluid dampers devices will not generally increase the strength or stiffness of the structure, unless the excitation frequency is high. In general, all these systems provide a reduction in drift and, therefore, reduction of structural damage, thanks to energy dissipation, and an increase in the total lateral forces, thanks to increased strength and/or stiffness).

Figure 2.1 shows force-deformation curves of a simple one-story structure with and without energy dissipation systems (EDS).

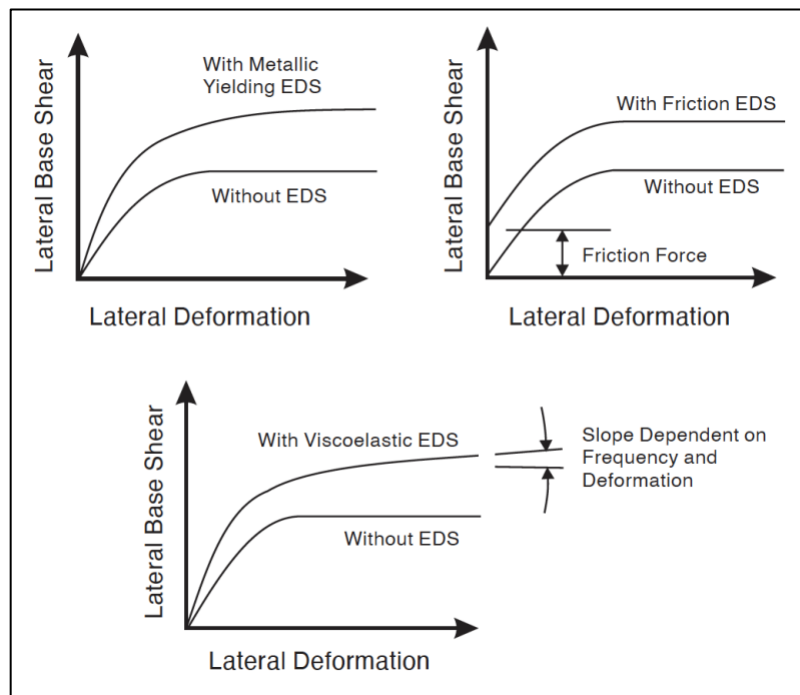


Figure 2.1 Effect of Energy Dissipation Systems on Force-Deformation curves of a structure

Energy dissipation systems are classified as earthquake protection systems since their function is to mitigate earthquake hazard; in any case, these devices are also useful in reducing dynamic response under wind horizontal loads.

Figure 2.2 depicts the elements of a passive control system. It is important to understand that its operation is activated by motion of the structure during dynamic excitation and does not require an external source of energy, while active or semi-active system does.

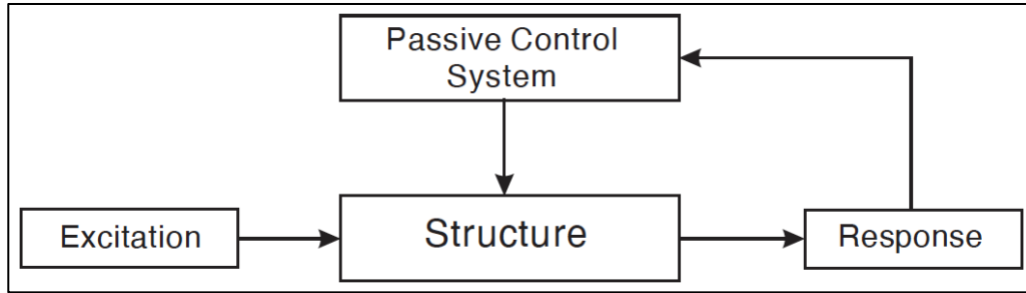


Figure 2.2 Scheme of a Passive Control System

### 2.2.1 Energy balance equation

In this paragraph, basic principles of passive energy dissipation are explained using the simple single degree of freedom (SDOF) structural system displayed in Figure 2.3. The structure consists in a simple frame of mass  $m$  subjected to an earthquake load at its base represented by a given ground acceleration  $\ddot{x}_g(t)$ , (Serino and Occhiuzzi, 1994, Losanno, 2015). The frame is provided with a linear viscous damper, thus the viscous damping force – velocity relationship is linear and proportional to the damping coefficient  $C_d$ .

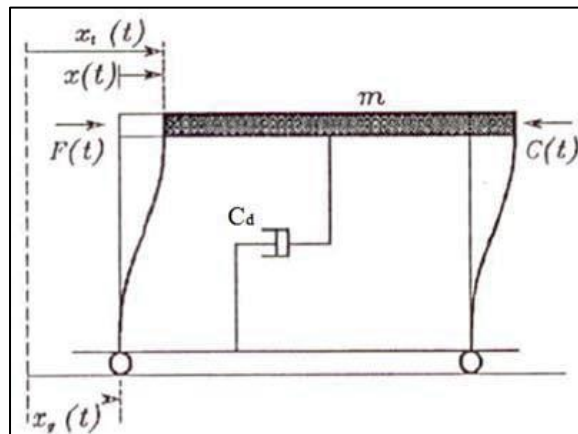


Figure 2.3 Structural scheme for energy balance equation

Indicating with  $x(t)$  the displacement of the mass relative to the base and with  $f_R(x, \dot{x}, t, \dots)$  the total restoring force acting in the columns, not necessarily elastic or linear, the equation of motion that describes the problem is:

$$m\ddot{x}(t) + C_d\dot{x}(t) + f_R(x, \dot{x}, t, \dots) = -m\ddot{x}_g(t) \quad (2.2)$$

The viscous damping force  $C_d\dot{x}(t)$  takes into account all the inherent damping dissipating mechanisms. It is important to note that generally these dissipating mechanisms are not really viscous and velocity dependent, but this modelling is accepted in structural engineering for mathematical convenience. The viscous damping force is, thus, defined as equivalent.

Considering the absolute displacement, evaluated with respect to a fixed reference system, of the mass  $x_t(t) = x(t) + x_g(t)$  and multiplying both sides of eq. (2.2) by  $dx = \dot{x}(t)dt$  and integrating between the initial condition  $t = 0$ , for which the structure is supposed to be at rest, so  $x(0) = 0$  and  $\dot{x}(0) = 0$ , and a generic time  $\bar{t}$ :

$$\int_0^{\bar{t}} m\ddot{x}_t(t)dx + \int_0^{\bar{t}} C_d\dot{x}(t)dx + \int_0^{\bar{t}} f_R(x, \dot{x}, t, \dots)dx = 0 \quad (2.3)$$

The first term on the left side of the eq. (2.3) can be written as follows:

$$\int_0^{\bar{t}} m\ddot{x}_t(t)dx = \int_0^{\bar{t}} m\ddot{x}_t(t)dx_t - \int_0^{\bar{t}} m\ddot{x}_t(t)dx_g \quad (2.4)$$

where:

$$\int_0^{\bar{t}} m\ddot{x}_t(t)dx_t - \int_0^{\bar{t}} m\ddot{x}_t(t)dx_g = \frac{1}{2}m\dot{x}_t^2(\bar{t}) - \int_0^{\bar{t}} m\ddot{x}_t(t)dx_g \quad (2.5)$$

Therefore, as displayed in (2.5), the first term on the left side of the eq. (2.3) can be written as the sum of the absolute kinetic energy of the mass and the work done by the total input force acting at the base of the structure, that in other terms is the seismic

input energy. In conclusion, the integral form of the energy balance equation at time  $t$  can be written as:

$$E_k(t) + E_D(t) + E_R(t) = E_I^e(t) \quad (2.6)$$

where:

- $E_K(t) = \frac{1}{2}m\dot{x}_t^2(t)$ , is the absolute kinetic energy;
- $E_D(t) = \int_0^t C_d\dot{x}(t)dx$ , is the equivalent viscous damping dissipated energy;
- $E_R(t) = E_H(t) + E_S(t) = \int_0^t f_R(x, \dot{x}, t, \dots)dx$ , is the restoring force adsorbed energy;
- $E_I^e(t) = \int_0^t m\ddot{x}_t(t)dx_g$ , is the seismic input energy.

The seismic input energy has a true physical meaning, since it represents the work done by the total base shear. It is important to highlight the difference between dissipated energy and adsorbed energy: the first one is an irrecoverable amount of energy (e.g., converted in material plastic deformation), while the second one can be partially or totally recovered. The restoring force adsorbed energy can be split into two quantities: the irrecoverable hysteretic energy  $E_H(t)$  and the recoverable elastic strain energy  $E_S(t)$ .

$$E_k(t) + E_D(t) + E_H(t) + E_S(t) = E_I^e(t) \quad (2.7)$$

In conclusion, the eq. (2.7) gives an important indication about the possible seismic design strategies, that can be summarized as follows:

- reduce the seismic input energy  $E_I^e$ ;
- increase the equivalent viscous damping dissipated energy  $E_D$ ;
- increase the irrecoverable hysteretic energy  $E_H$ .

For example, the seismic input energy can be reduced adopting the base isolation solution. Actually, in that way the input energy that reaches the superstructure is significantly reduced because the dissipation is mainly concentrated in the isolators.



The dissipated energy can be increased adding supplemental damping systems, that led to an increase of the quantities  $E_D$  and (or)  $E_H$ .

### 2.3 Classification of PED systems

According to the American FEMA 273 (Federal Emergency Management Agency) "NEHRP Guidelines for the seismic rehabilitation of buildings", energy dissipation devices are classified as either displacement-dependent, velocity-dependent, or others. Displacement-dependent devices may exhibit either rigid-plastic (friction devices), bilinear (metallic yielding devices) or trilinear hysteresis. The response of displacement-dependent devices is independent of velocity and/or frequency of excitation. The simplest model of hysteretic behavior involves algebraic relations between force and displacement. Figure 2.4 shows typical force-displacement loops of hysteretic energy dissipation systems.

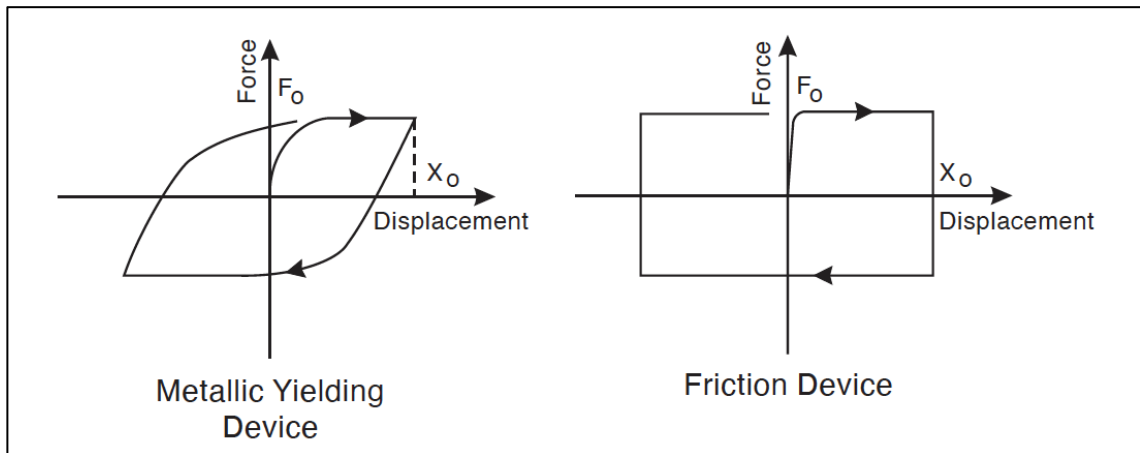


Figure 2.4 Idealized force-displacement loops of hysteretic energy dissipation devices

Velocity-dependent devices include solid and fluid viscoelastic devices, and fluid viscous devices. Figure 2.5 shows force-displacement loops of these devices. Typically, these devices exhibit stiffness and damping coefficients which are frequency dependent; the damping force in them is proportional to velocity due to their viscous behavior. These devices are classified as viscoelastic devices; a purely viscous device is a special case of viscoelastic device with zero stiffness and frequency independent properties.

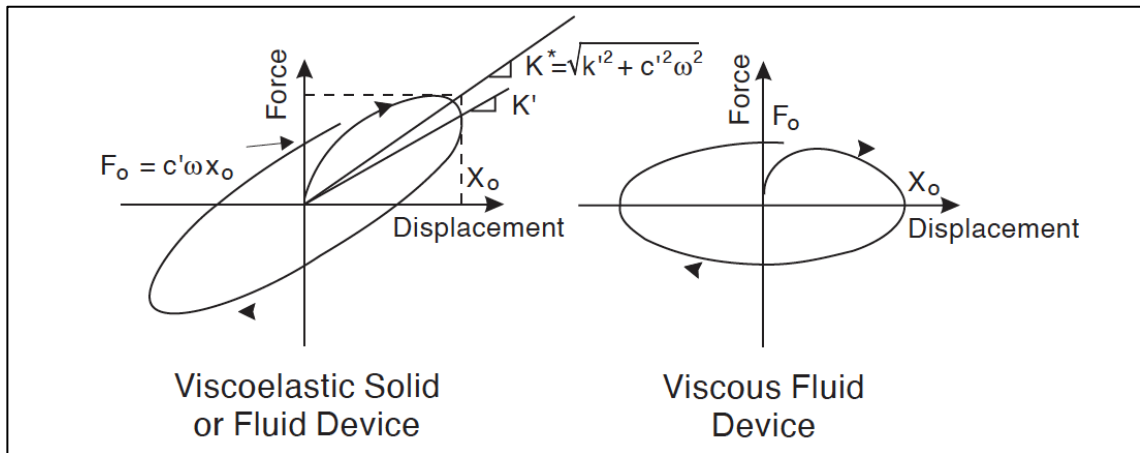


Figure 2.5 Idealized force-displacement loops of viscoelastic energy dissipation devices

Energy dissipation devices which cannot be classified as either displacement or velocity dependent are classified as other systems. Example of other devices include frictional-spring device with recentering capability, fluid restoring force-damping devices. Figure 2.6 depicts the behavior of these devices.

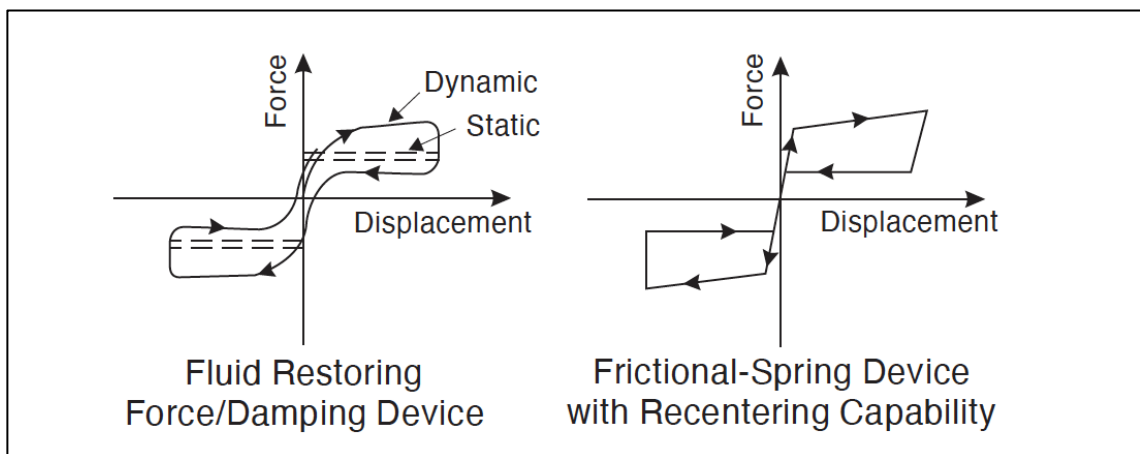
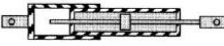

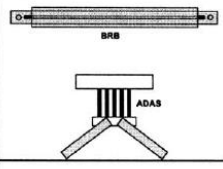

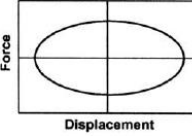
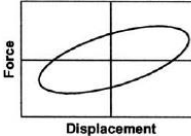
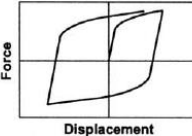
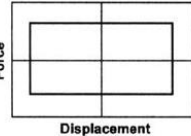
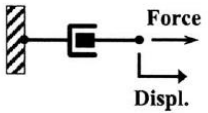
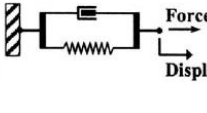
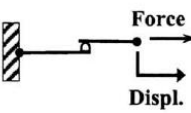


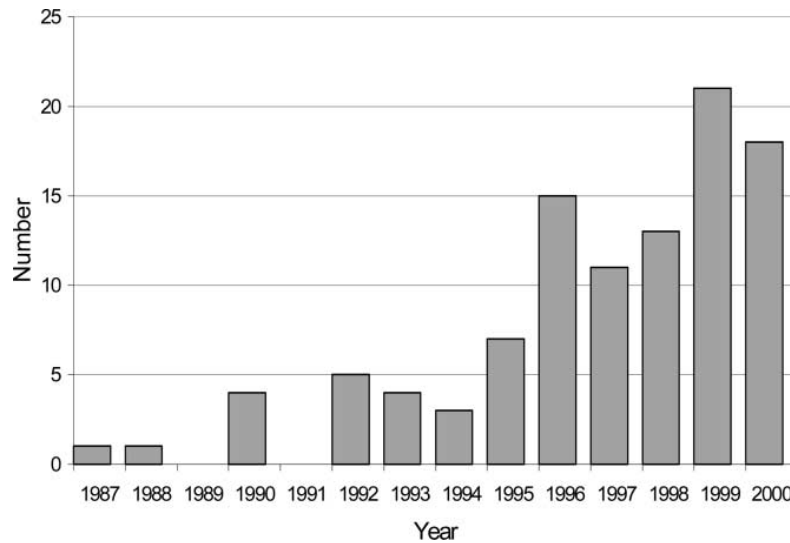
Figure 2.6 Idealized force-displacement loops of other energy dissipating devices

The following Table 2.1 summarizes the main aspects of most common energy dissipation devices used in North America.

Table 2.1 Summary of the main aspects of Passive Energy Dissipation systems  
(Constantinou et al., 2008)

	Viscous Fluid Damper	Viscoelastic Solid Damper	Metallic Damper	Friction Damper
<b>Basic Construction</b>				
<b>Idealized Hysteretic Behavior</b>				
<b>Idealized Physical Model</b>			Idealized Model Not Available	
<b>Advantages</b>	<ul style="list-style-type: none"> <li>- Activated at low displacements</li> <li>- Minimal restoring force</li> <li>- For linear damper, modeling of damper is simplified.</li> <li>- Properties largely frequency and temperature-independent</li> <li>- Proven record of performance in military applications</li> </ul>	<ul style="list-style-type: none"> <li>- Activated at low displacements</li> <li>- Provides restoring force</li> <li>- Linear behavior, therefore simplified modeling of damper</li> </ul>	<ul style="list-style-type: none"> <li>- Stable hysteretic behavior</li> <li>- Long-term reliability</li> <li>- Insensitivity to ambient temperature</li> <li>- Materials and behavior familiar to practicing engineers</li> </ul>	<ul style="list-style-type: none"> <li>- Large energy dissipation per cycle</li> <li>- Insensitivity to ambient temperature</li> </ul>
<b>Disadvantages</b>	<ul style="list-style-type: none"> <li>- Possible fluid seal leakage (reliability concern)</li> </ul>	<ul style="list-style-type: none"> <li>- Limited deformation capacity</li> <li>- Properties are frequency and temperature-dependent</li> <li>- Possible debonding and tearing of VE material (reliability concern)</li> </ul>	<ul style="list-style-type: none"> <li>- Device damaged after earthquake; may require replacement</li> <li>- Nonlinear behavior; may require nonlinear analysis</li> </ul>	<ul style="list-style-type: none"> <li>- Sliding interface conditions may change with time (reliability concern)</li> <li>- Strongly nonlinear behavior; may excite higher modes and require nonlinear analysis</li> <li>- Permanent displacements if no restoring force mechanism provided</li> </ul>

A large number of passive control systems or PED devices have been developed and installed in structures for improve the structural performance under earthquake loads. Figure 2.7 depicts the number of buildings within devices have been implemented during the years in North America.



*Figure 2.7 Implementation of PED in North America for seismic applications (Soong and Spencer, 2002)*

The following paragraphs describe some of the most common types of metallic dampers used in structural engineering.

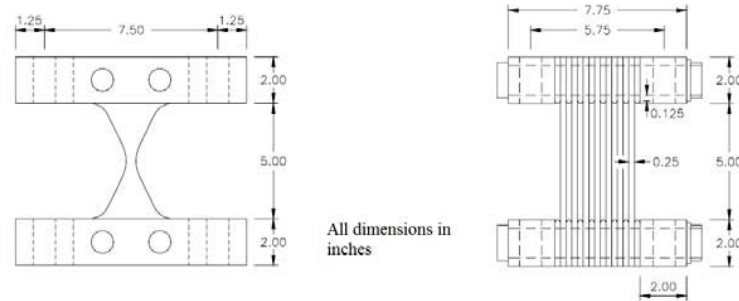
## **2.4 Metallic dampers**

Many different steel dampers have been proposed and investigated in literature, exploring different materials, geometric shapes, manufacturing process and connection configurations to the structure. These devices dissipate the seismic input energy through inelastic deformation of metal. They are usually made by mild steel plates with triangular or X shapes so that yielding is spread almost uniformly throughout the material. Generally, the metallic devices display a stable hysteretic behavior, low-cycle fatigue property, long term reliability and relative insensitivity to environmental temperature.

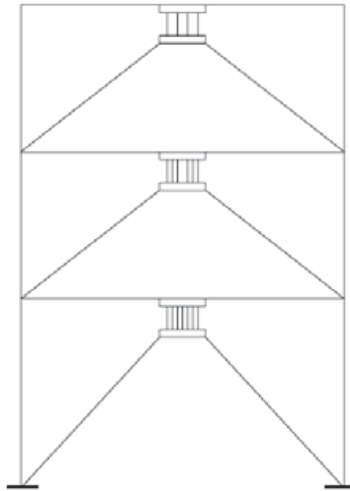
### **2.4.1 Adas damper**

The Adding Damping and Stiffness (ADAS) is a known yielding steel damper that consists of a series of steel plates wherein the bottom of the plates is attached to the top of a chevron bracing arrangement and the top of the plates are attached to the beams above the bracing, as shown in Figure 2.9. To ensure the correct behavior of

the device, the chevron bracing needs to be very stiff; in addition, the dampers should be designed so that at their yielding, axial loads in the bracing systems are lower than their capacity calculated accordingly to both plasticity and buckling theories.



*Figure 2.8 Geometry of the device*



*Figure 2.9 Conventional localization of the connection in a frame*

ADAS dampers are activated by interstory drifts and, as the level above the device deforms laterally, the device is subjected to a shear force that induces bending moments over the height of the plates. Due to the geometrical configuration of the plates, the bending moments produce a uniform flexural stress distribution inside the device. For this reason, also the inelastic action occurs uniformly inside the damper. Generally, the plates can be fixed-pinned, so the geometry is triangular (Figure 2.10, left) or the plates can be fixed-fixed and in that case the geometry is an hourglass shape (Figure 2.10, right). In practical applications, it is difficult to separate the effects of added stiffness and added damping on the structural response, but in general both tend

to reduce the displacements of the structure. The consequence is that metallic hysteretic dampers, in addition to increasing the damping, modify in a significant way the dynamic characteristics of the structure. In most of cases, the introduction of the devices led to a stiffer structure, because they reduce the fundamental period, and this results in an increase of the base shear.

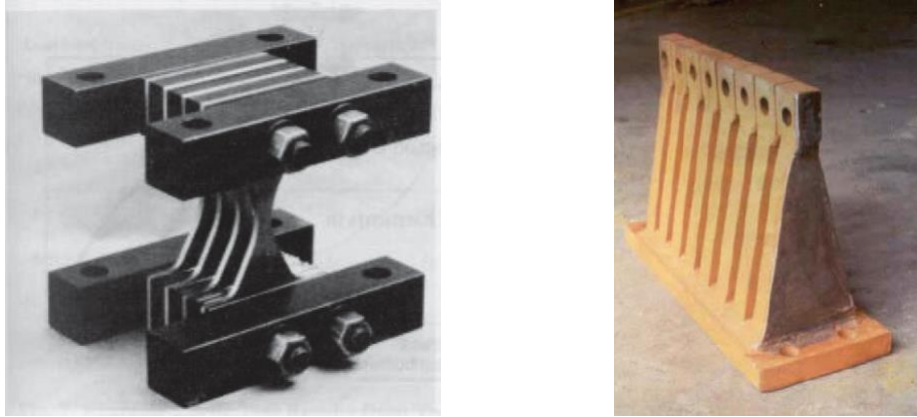


Figure 2.10 ADAS (left) and TADAS (right) device

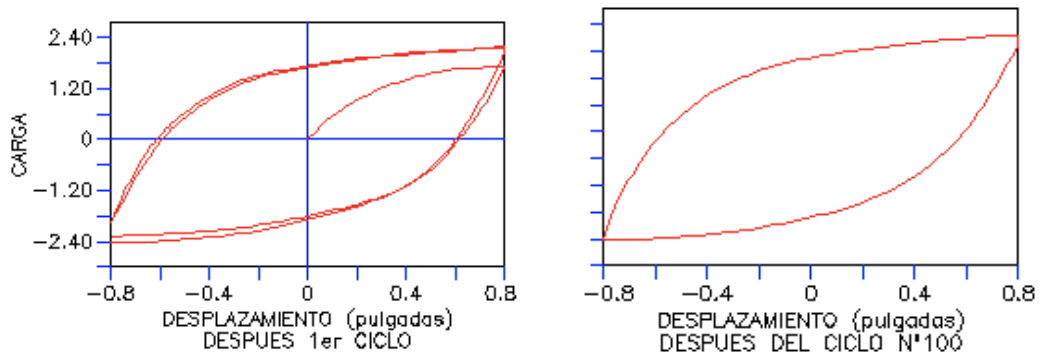


Figure 2.11 ADAS and TADAS force-displacement relationship, 1<sup>st</sup> vs 100<sup>th</sup> cyclic load

## 2.4.2 Buckling Restrained Brace (BRB) device

Another device belonging to the metallic dampers is the tension/compression yielding brace, also known as unbonded brace (Ozcelik et al., 2017). An unbonded brace is a bracing member consisting of a core steel plate encased in a concrete-filled steel tube. In order to reduce friction, a special coating is provided between the core plate and concrete.

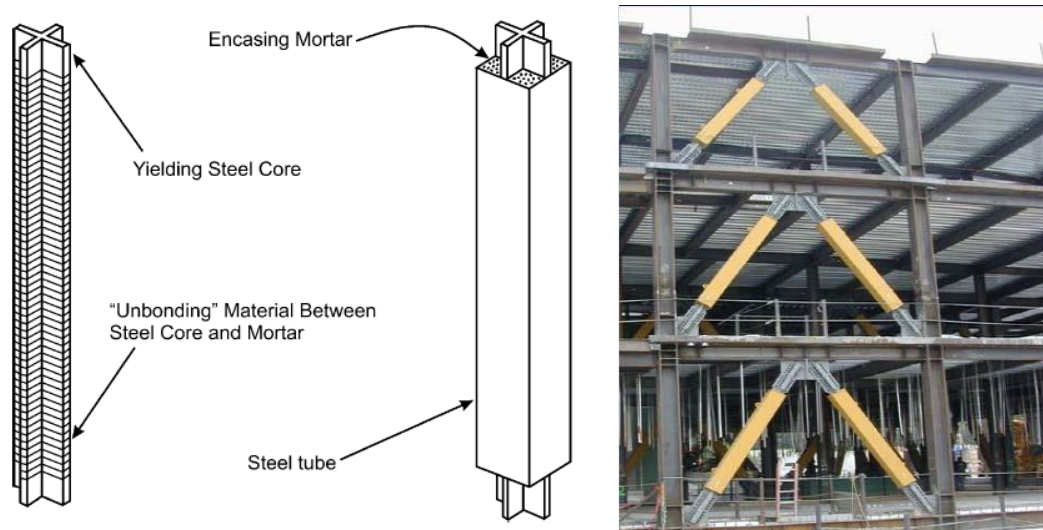


Figure 2.12 BRB device

The core steel plate provides stable energy dissipation through the yielding under the axial loading, both in tension and compression, due to the surrounding concrete-filled steel tube that avoids the compression buckling phenomenon of the device. For this reason, the tension and compression hysteretic cycles of the damper are essentially the same, as depicted in Figure 2.13.

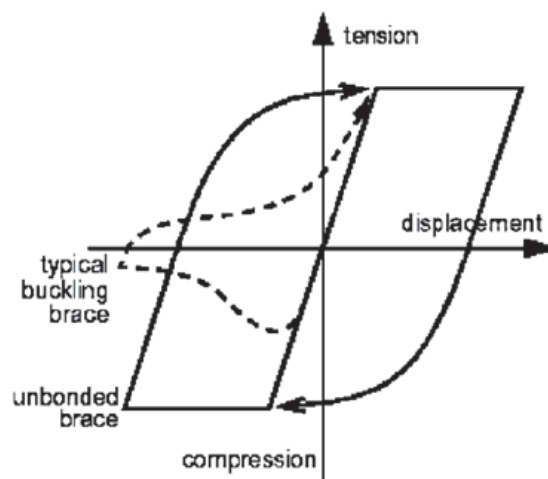


Figure 2.13 Force-displacement relationship of the BRB device

During the initial elastic response of the BRB damper, the device provides only stiffness to the structure. As the BRB starts to yield, the stiffness reduces and energy dissipation occurs due to inelastic hysteretic response.

BRB device can be generally divided into three different parts: an unrestrained elastic zone, a restrained elastic one and a restrained plastic one. The unrestrained elastic zone is designed to provide a connection between the BRB and the gusset plate and is also capable of resisting axial demands without buckling when the restrained plastic zone yields in tension and compression. The restrained elastic zone is a transition part of the core plate between elastic and plastic behavior. Although this zone is characterized by an elastic behavior under tension and compression, the casing member prevents it from buckling. The restrained plastic zone carries the tension and compression forces elastically and plastically.

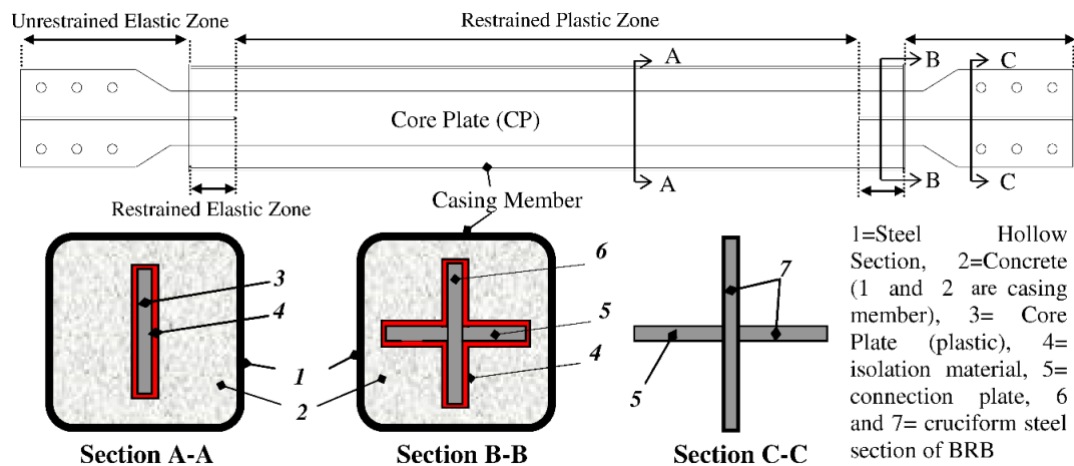


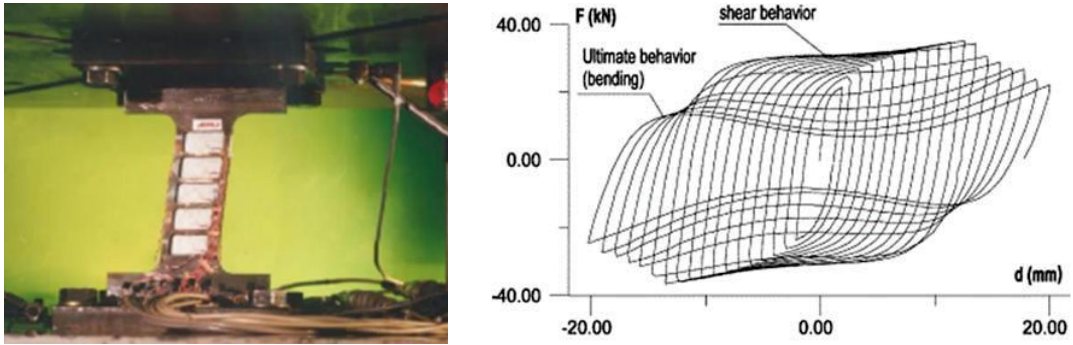
Figure 2.14 Details of BRB (Ozcelik et al., 2017)

### 2.4.3 Shear Link device

The shear link device represents a more recent application in the field of metallic dampers. The classical application of the shear link device consists in a device attached to diagonal or chevron braces, such as for ADAS and TADAS devices. More recently, an alternative application, that consists in one or more devices attached to a decoupled concrete wall, had been developed. A particular shear link device is the SLB (Shear Link Bozzo), that is a low-cost metallic hysteretic device obtained from a hot



laminated steel plate, which is made thinner by a milling process. This process results in thinner windows that yields under shear stress in a stable way, due to the transverse and longitudinal stiffeners.

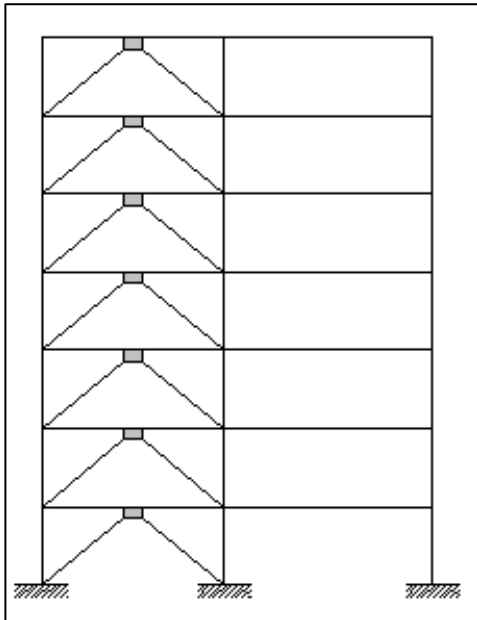


*Figure 2.15 Shear link device (left) and force-displacement relationship (right)*

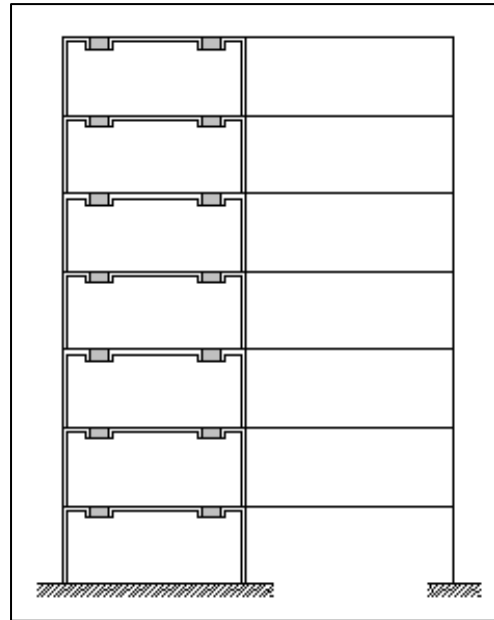
The Shear Link Bozzo device is described in more details in the next dedicated chapters 3 and 4, since its study represents one of the fundamental topics of this thesis.

### 3 SHEAR LINK BOZZO DEVICE

This chapter describes the main aspects of the Shear Link Bozzo device, that is an energy dissipation device suitable for seismic protection. It consists of a metallic yielding device first developed at the University of Girona, Spain, in 1997. This device is particularly advantageous due to its flexibility in covering a wide range of force capacities, that makes it adaptable to different levels of demand. The basic idea behind the SLB device is providing local ductility, while avoiding local buckling in a simple, manufactured controlled and cheap way. The simplicity of SLB devices geometry makes them particularly suitable to be adapted within the structure. Figure 3.1 shows the classic application with steel braces, that limit the force transferred to the diagonal and dissipators. Figure 3.2 shows an alternative application through decoupled concrete walls characterized by a thickness of 15-30 cm and with SLB connections. It is important to highlight another peculiarity of SLB device, which consists in the fact that these devices do not need to be aligned vertically since the current connection does not transfer axial load.



*Figure 3.1 Traditional application with steel braces*



*Figure 3.2 SLB application with decoupled reinforced concrete walls*

### 3.1 Description of the Shear Link Bozzo (SLB) device

The Shear Link Bozzo (SLB) device belongs to the family of hysteretic passive control devices. The SLB system consists of a metallic hysteretic damper obtained from a hot laminated steel plate which is generally modelled to realize an I-shape. Figure 3.3 shows the current general geometry of SLB energy dissipator and its particular connection system, generally defined as battlement (or “toothed”) connection, which does not transmit axial load.

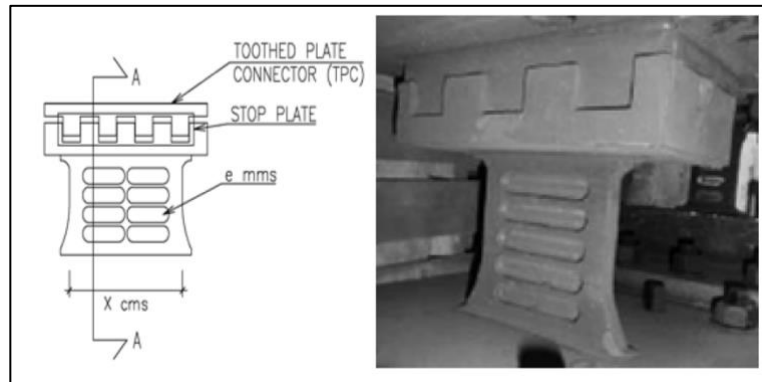


Figure 3.3 Geometry of Shear Link Bozzo device

The main shape is obtained from a rectangular hot laminated element in structural steel, which is reduced, in some part of it, by a milling machine. In this way, without any welded part, it is possible to obtain some “windows” of thinner thickness along the web of device. The flanges of the device represent the stiffer parts and are employed to realize the connection to structural elements.

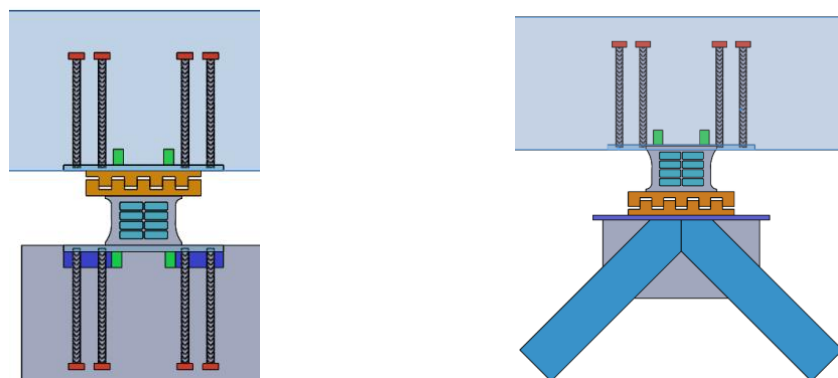


Figure 3.4 Installation of 4<sup>th</sup> gen. SLB device in decoupled walls (left) and in chevron braces (right)

The dissipation capacity of the SLB device depends from the height, width and thickness of the dissipative windows and web stiffeners. A proper design of the SLB guarantees two working stages for the device: before milled areas yielding, it works according to a “shear mode”, so it is characterized by an approximative linear element’s deformation, uniform shear distribution and uniform “windows” plasticization (Figure 3.5a).

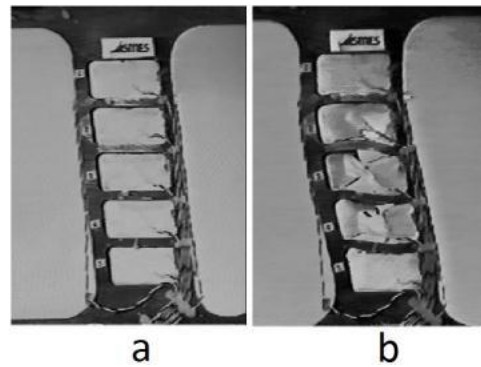


Figure 3.5 Working modes of SLB device: (a) shear and (b) bending, (Nuzzo et al., 2015)

After yielding and web buckling, the thinner parts of the device are subjected to degradation, however the device continues to dissipate energy through a “bending mode” (Figure 3.5b) with a reduced stiffness, if compared to the “shear mode” stiffness, as shown in Figure 3.6.

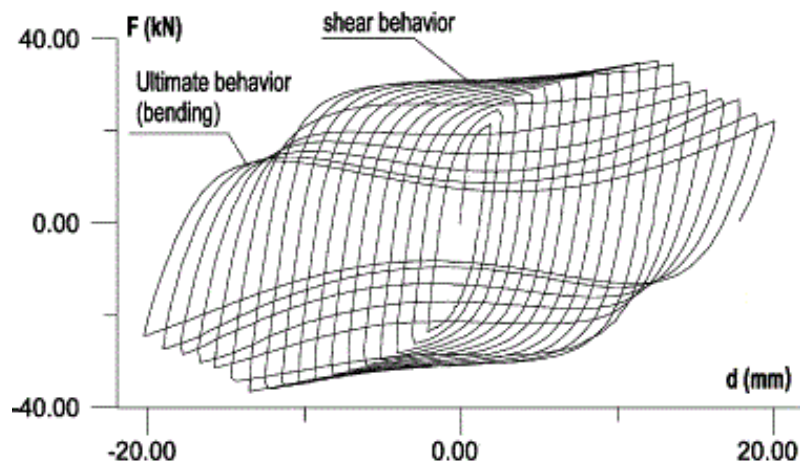


Figure 3.6 Shear Link Bozzo typical hysteretic curves, (Nuzzo et al., 2015)

Stable hysteretic curves imply that the SLB energy dissipation device must be designed so that yielding is reached before the buckling of the thinner “windows”, since buckling causes a significant reduction of the dissipative capacity. For this reason, these devices are characterized by horizontal and vertical stiffeners between milled areas.

Designing a shear link energy dissipation device means to define several parameters, the most important are steel grade of the material, total height, dissipative height, width, thicknesses, position and dimension of stiffeners.

For this reason, different generations of SLB, described in the following paragraphs, have been proposed and investigated both numerically and experimentally during last 20 years (Figure 3.7) with the aim to optimize their mechanical behavior.

1<sup>st</sup> generation2<sup>nd</sup> generation3<sup>rd</sup> generation4<sup>th</sup> generation

*Figure 3.7 Fourth generations of SLB device*

The first generation is characterized by four dissipative windows in the web, divided in two columns, and a bolted connection. The second generation, as the previous one, is characterized by the same height and thickness of the stiffeners and a bolted connection as well. The bolted connection prevents the device from being welded, also

---

allows an easier installation and replacement of the SLB during the lifetime of the building. The main difference of the second generation is the number of dissipative windows, always distributed in two columns, that is increased from a total of four to eight, reducing their height but significantly increasing their width in order to enhance ductility as well as to improve buckling resistance. A further innovation is the adoption of slotted holes for connection on one side, with the aim to avoid axial load transferred from the upper beam to the device and vice versa. The third generation introduces a very important innovation, compared to previous generations, that is the battlement connection. This connection avoids transferring axial force to the device allowing an important architectural advantage, because the dissipator can be freely placed into the structure in height and plan. The fourth generation presents the same battlement connection of the 3<sup>rd</sup> one, but an increased deformation capacity of the device due to an increase of the height of the device, from the 155 mm of the 3<sup>rd</sup> generation to the 270 mm of the 4<sup>th</sup> one, and an increase of the width of the dissipative windows, in order to avoid buckling phenomena, from 25 mm to 50 mm.

## **3.2 Experimental campaign of SLB Device**

A large experimental campaign has been carried out over the past 20 years in order to investigate and improve the behavior of SLB device. Each generation has been tested leading to the calibration of the analytical and numerical models based on the results obtained from the tests.

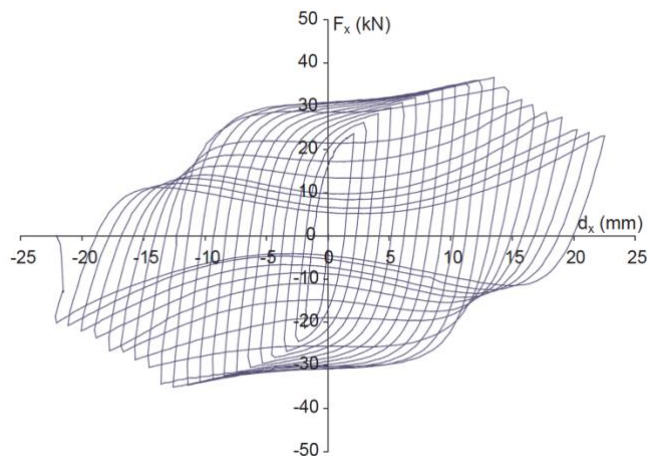
### **3.2.1 First generation**

The first experimental studies were performed at ISMES S.p.A., in Bergamo (Italy) in 1997, where the prototype (Figure 3.8) of the first generation of SLB devices was tested (Nuzzo et al., 2018).



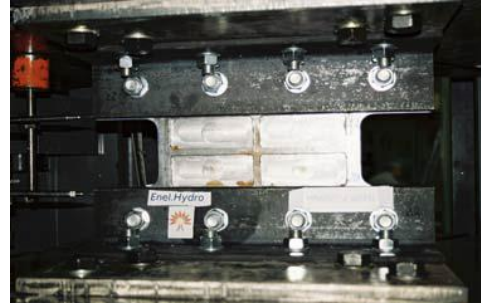
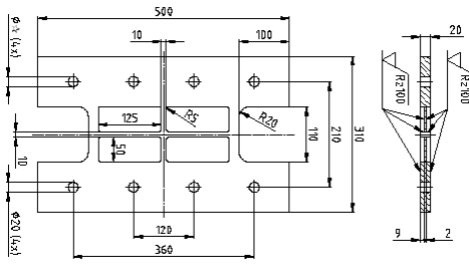
*Figure 3.8 Prototype of the SLB 1<sup>st</sup> generation*

The flanges of the devices were welded to horizontal thick plates, constituting elements of connection to the machine, through high strength bolts. In the web, there was a unique column of dissipative windows with thicknesses between 1.5 and 2.0 mm, while flanges and other stiffeners were 15 mm thick. Four devices with different types of transition zone between the web and stiffeners were cyclically tested, all performing stable hysteretic behavior with significant strain hardening. It is important to note that after severe damage of the dissipative windows, the SLB devices continued to exhibit a stable behavior even with lower hysteretic curves corresponding to a flexural dissipative behavior as shown in Figure 3.9.



*Figure 3.9 Experimental force-displacement hysteretic curve (ISMES, 1997)*

A further device belonging to the first SL generation (see Figure 3.10 and Figure 3.11) has been tested again at ISMES S.p.A. in 2001 with the aim to generalize its mechanical properties for many different yielding force levels.



*Figure 3.10 Dimensions of the SLB device*      *Figure 3.11 SL tested at ISMES, Italy (2001)*

To define the optimum shape and characteristics of the dissipator, four basic devices have been compared. All of them are characterized by two columns of dissipative windows in the web; all the devices have in common two vertical stiffeners (20 mm width) at both lateral ends, the width is 300 mm, the web thickness is 2 mm and the initial plate thickness is 20 mm. The connection to the equipment is just bolted and the role of the tolerance between holes and bolts has been analyzed through a parametric analysis. In the case of tolerances of 2 or 4 mm, tests were not concluded successfully because the slippage was too high. Otherwise, specimens with 1 mm of hole tolerance showed stable hysteretic curves with strain hardening, performing shear and flexural mode behaviors, similarly to what shown in Figure 3.9. Anyway, even in this case significant slippage was registered, observing collapse in correspondence of the vertical bolted connection. In this case the plastic nonlinear analysis has been performed using the computer program ANSYS (Bozzo et al., 2008). The model for all the cases corresponds to the isotropic hardening one giving the complete stress-strain material relation. Figure 3.12 shows the Von Mises stresses for a given imposed relative displacement of 20 mm for two of the four preliminary devices.



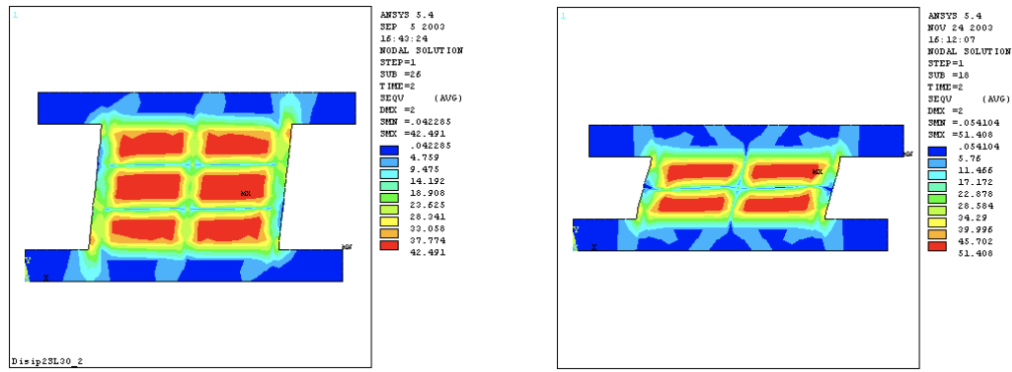


Figure 3.12 Von Mises stresses for the Dissip3SL30\_2 and Dissip4SL30\_2 devices

These stresses are uniformly distributed in all the dissipative windows, indicating a maximum profit of the material. Besides this indicates that the stiffeners do not affect significantly the dissipation.

Figure 3.13 shows the force-displacement relationship for the preliminary 200 mm vertical height proposed devices. In this step, the main objective was to study the influence of the stiffeners in the yielding strength and post-yielding slope. The increase in stiffeners involves a small increment in the yielding strength, although the post-yielding slope is maintained constant in all the cases. Thus, the total dissipated energy is increased as the number of stiffeners increases, although the milled area is reduced by them. This result is explained by the stiffness increase. For design purposes, however, all the devices tested had very similar performances regarding the force-displacement relationship.

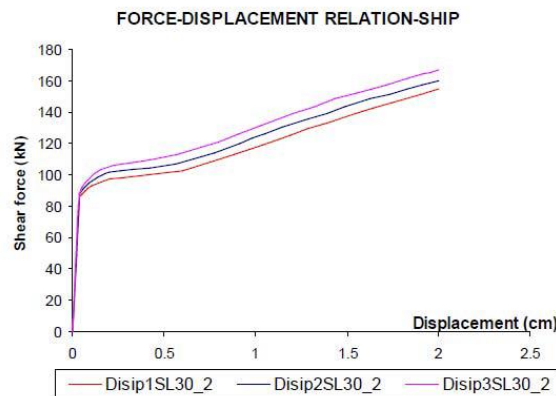


Figure 3.13 Nonlinear monotonic force-displacement relationship

---

The device, indicated as SL30\_2, has been compared to the first one tested in 1997 (prototype) and is characterized by two columns of dissipative windows in the web. The connection to the equipment was just bolted and the role of the tolerance between holes and bolts has been analyzed through a parametric analysis. In the case of tolerances of 2 or 4 mm, tests were not concluded successfully because the slippage was too high. Otherwise, specimens with 1 mm of hole tolerance showed stable hysteretic curves with strain hardening, performing shear and flexural mode behaviors, similarly to what shown in Figure 3.9. Anyway, even in this case significant slippage was registered, observing collapse in correspondence of the vertical bolted connection. In order to continue the test, the damaged connection was welded to the horizontal plate, but after a high number of cycles even the weld connection failed. In any case, slippage was not considered a good response characteristic since, in general, is difficult to consider its influence. For this reason, the tolerance was reduced as much as possible to avoid this problem.

In order to develop a design table for SLB devices, a numerical-experimental calibration test has been performed. Figure 3.14 resumes this calibration demonstrating that a good correlation can be obtained using a relatively simple isotropic hardening plasticity model. This aspect represents an advantage of the device if compared to other ones based on friction or viscous-elastic response that require a more difficult modelling.

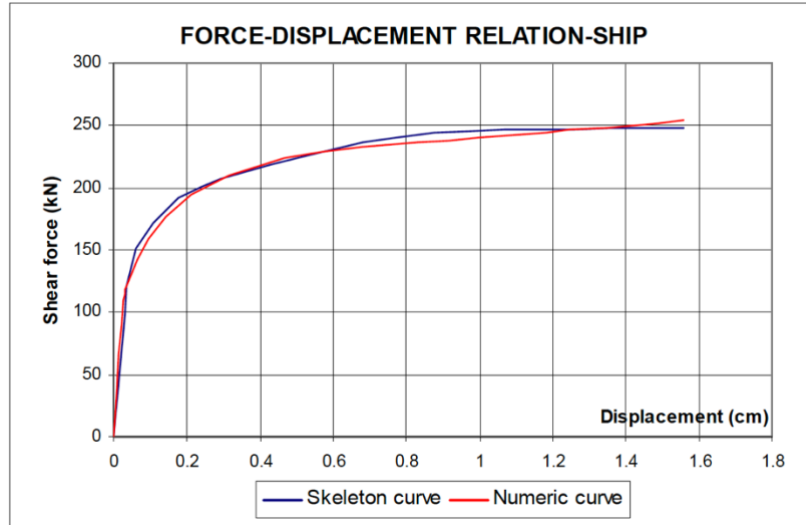


Figure 3.14 Experimental vs numerical monotonic force-displacement relationship

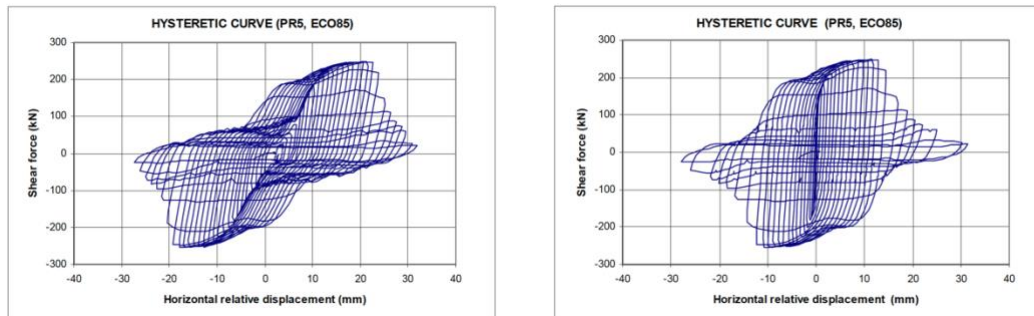


Figure 3.15 Hysteretic curve for device with (left) and without (right) slippage of the bolts

A further device belonging to this generation was tested at the laboratory of the Pontificia Universidad Católica del Perú in Lima, in 2015. The geometry was similar to the SL30\_2, but smaller, with a total web's width  $L$  of 25 cm, for that reason it is indicated as SL25\_2. A horizontal actuator was used to apply a quasi-static load history to the device through the interposition of a square hollow element under controlled displacement. During the test, the specimen suffered an out-of-plane failure mechanism, that caused a premature interruption of the experiment.

### 3.2.2 Second generation

The performance of the second SLB generation has been tested at the laboratory of the University of Naples Federico II in collaboration with University of Naples Parthenope, in 2016 (Nuzzo et al., 2018). A total of 10 devices of 5 different

geometries have been tested, disposing of 2 samples for each typology. Each device is generally indicated as SL X\_Y, where X is the web width in cm and Y is the dissipative windows thickness in mm. Total height (310 mm), height of the web (110 mm) and thickness of the plate (19 mm) are the same for all the devices. The thickness of the dissipative windows is 3 or 5 mm, while the web width is 300, 400 or 500 mm. Seven devices have been tested with cyclical loads, the remaining three ones have been subjected to monotonic load.

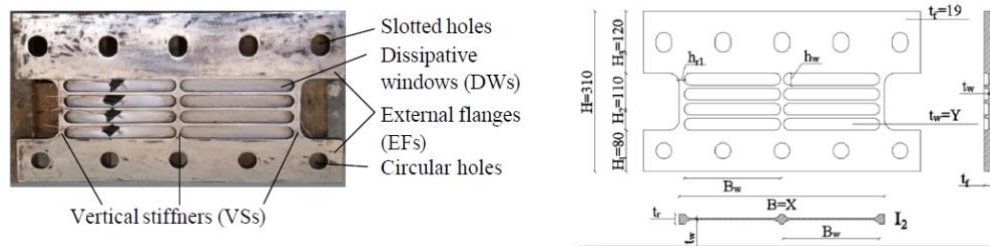


Figure 3.16 Geometry of the tested 2<sup>nd</sup> generation SLB device

The connection of the tested devices is made by means of M30 high strength bolts. On one side, there are circular 30.5 mm holes, while on the other one 30.5 x 38 mm slotted holes have been realized. Bolts in circular holes have been always fully tightened to achieve a fixed configuration without slippage. In order to understand the role of the boundary conditions in the mechanical response of the device, bolts in slotted holes have been fully tightened in some configurations, indicated a FF (fixed-fixed), and in other cases they have not been tightened at all, obtained a FNF (fixed-non fixed) configuration. In particular, the slotted holes had been thought to avoid the axial stress in the device due to deflection of the beam under gravity loads. In conclusion, due to free or restrained rotations at slotted holes, the device can be roughly studied as a cantilever in the FNF configuration and as fixed at both ends in the FF configuration, as depicted in Figure 3.17

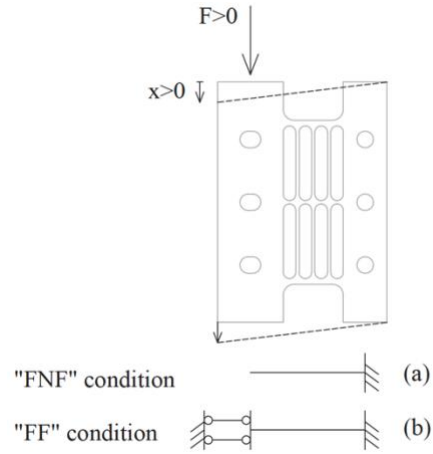


Figure 3.17 Boundary condition for SLB devices

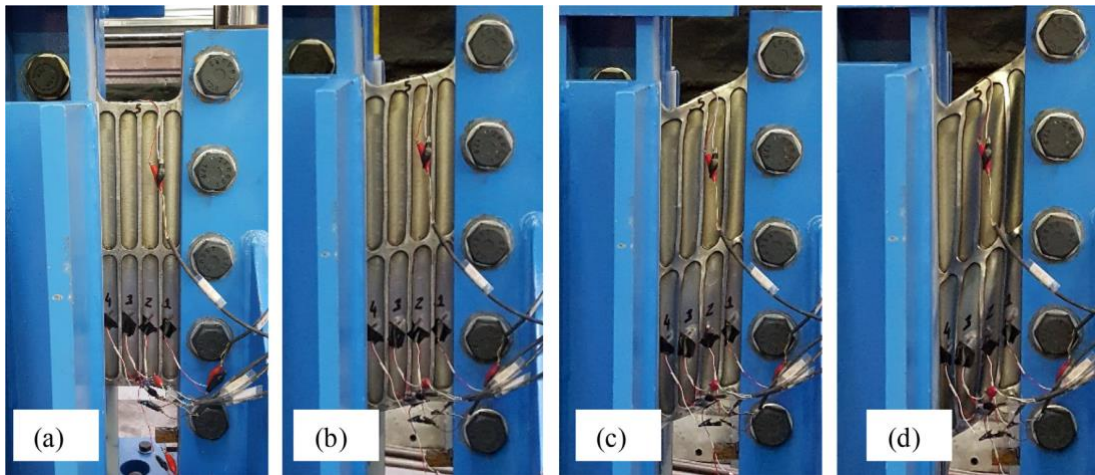


Figure 3.18 Monotonic test #4 damage scenario: (a) initial condition, (b) yielded phase, (c) onset of buckling, (d) global buckling

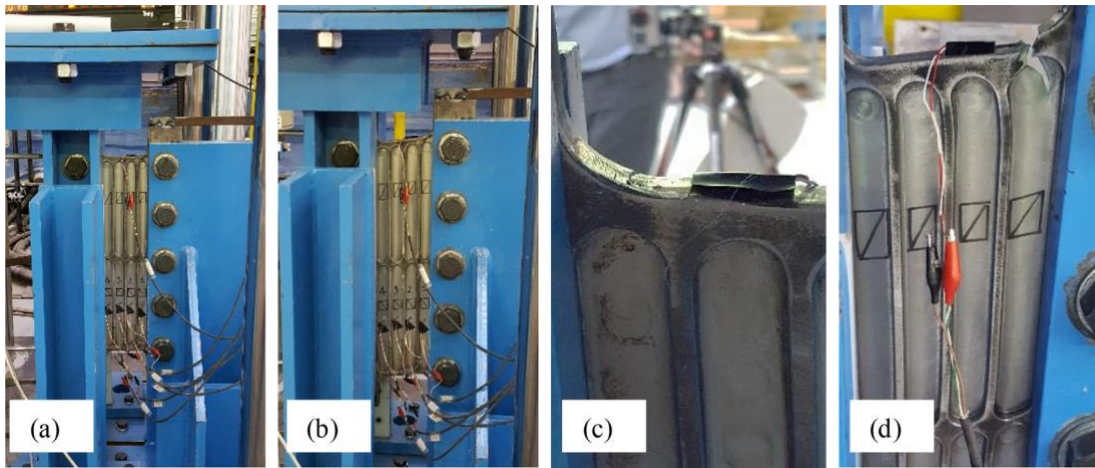


Figure 3.19 Cyclic test #10 damage scenario: (a) initial condition, (b) yielded phase, (c) onset of tearing, (d) distribution of tearing

Test results in terms of force-displacements response showed smoother curves for FF configuration devices, as expected, while the ones in the FNF configuration are more irregular due to the sliding of bolts within the slotted holes.

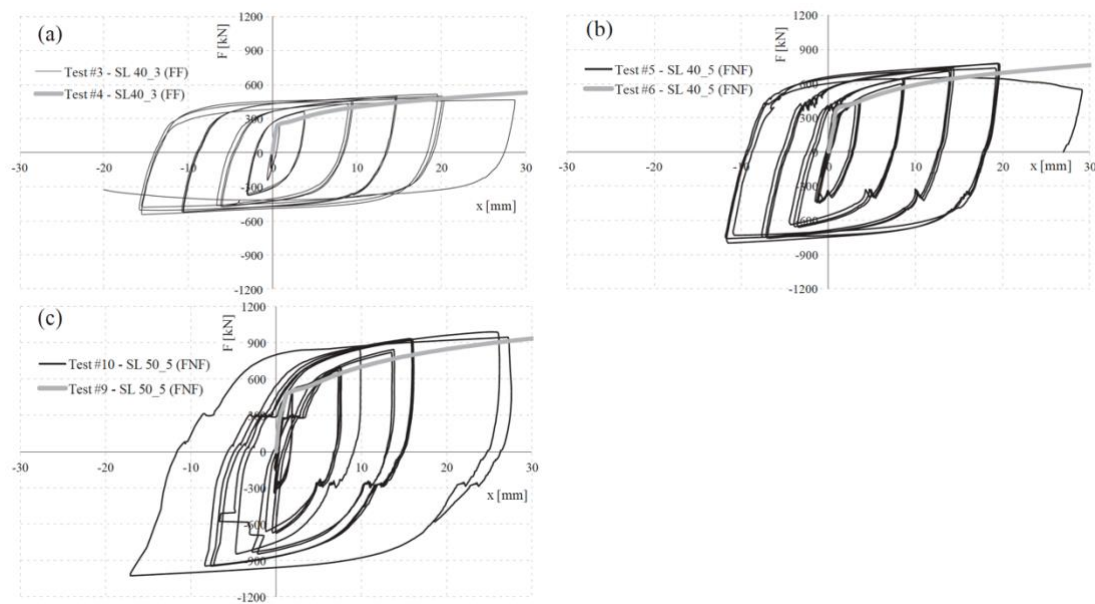


Figure 3.20 Example of cyclic and monotonic  $F$ - $x$  curves obtained from tests

Due to different boundary conditions, it can be observed that SL devices in FF configuration usually provide higher values of initial stiffness and yielding force than FNF case, although with no significant discrepancy. The same SL device provided almost the same maximum peak force for both cyclic and monotonic tests. However,



they occurred for different amount of displacement. Actually, the envelope of the loops registered for cyclic tests provided higher values of force with respect to the monotonic test on the same device. In conclusion, collapse phenomenon in the cyclic tests was due to tearing in the external stiffeners, while in monotonic tests samples suffered from web buckling. In terms of tightening configuration for the same device, the main difference between FF and FNF specimens arises from sliding at connections due to slotted holes. In addition, due to slippage at connections, non-symmetric hysteretic loops were obtained, especially under FNF configuration.

Finally, the finite element analysis of the SLB device has been performed using ABAQUS (Nuzzo et al., 2020) and analyzing both the FF and FNF configurations in monotonic and cyclic load conditions. For the monotonic analysis, the plastic behavior is defined through an isotropic hardening model, while for cyclic analysis the plastic behavior has been characterized through the Chaboche model, also known as “combined hardening model” implemented in ABAQUS. The assumption of this model is justified by the experimental hysteretic behavior of the device, that is affected by both kinematic and isotropic hardening, which are respectively responsible for the translation and expansion of the yielding surface. An ABAQUS analysis example of stress distribution at failure for one of the specimens is presented in Figure 3.21. The results demonstrate that the windows are characterized by a uniform shear stress distribution, confirming a global energy dissipation mechanism through the windows.

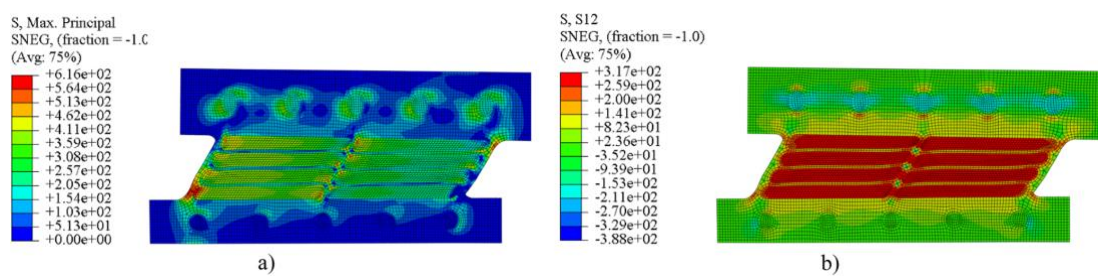


Figure 3.21 Stress distribution in FNF configuration: (a) principal maximum normal stress; (b) shear stress

Figure 3.22 shows the strain distribution at failure. In the FNF configuration (Figure 3.22, left) the maximum strain occurs in the stiffeners, while in the FF configuration

(Figure 3.22, right) is concentrated in the windows, demonstrating a great consistency with the experimentally observed failure mechanisms.

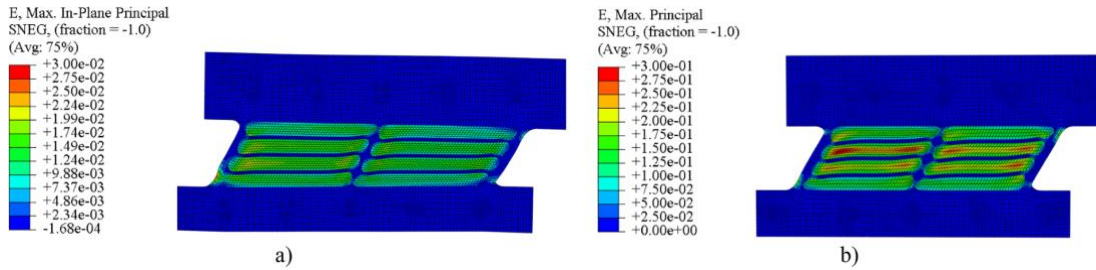


Figure 3.22 Strain distribution at failure for FNF (left) and FF (right) configuration

### 3.2.3 Third generation

The third generation of Shear Link Bozzo has been tested at the UNAM laboratory, Mexico, 2018 (Pantoja et al., 2020). The main objective of the work was to study the structural behavior of the SLB connections for a cyclic loading test, in order to compare an experimental and a numerical model of uncoupled reinforced concrete walls equipped with the SLB devices.

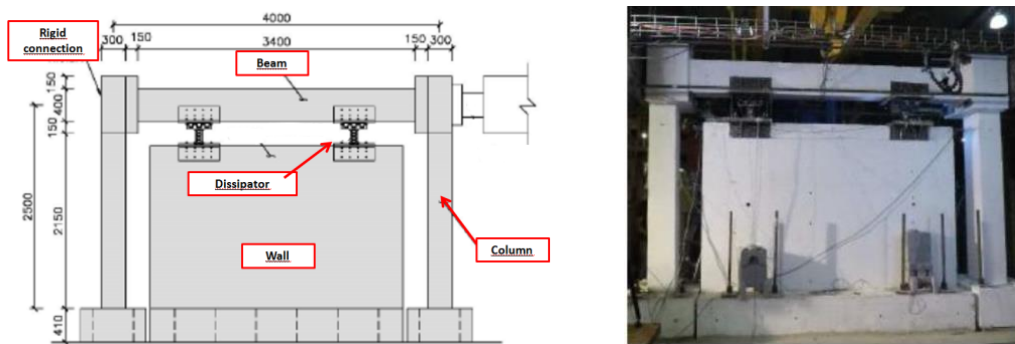


Figure 3.23 Geometry of the reinforced concrete frame, UNAM laboratory

The main significant feature of this generation of the device is the battlement connection, that avoids transferring axial force to the dissipator. Since these devices do not transfer axial load, this solution is called “uncoupled” concrete walls. The combination of reinforced concrete frames and uncoupled walls with dissipators increases stiffness and ductility, but most importantly, allows the walls not to be necessarily aligned in height, resulting in important architectural advantages.



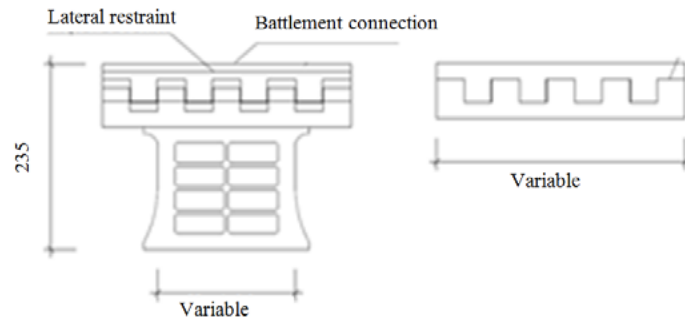


Figure 3.24 Geometry of 3<sup>rd</sup> generation SLB device

In order to understand the structural behavior of the SLB connections, three 1:1-scale tests were performed: a bare reinforced concrete frame, a reinforced concrete frame with 50 kN SLB devices (Type 1, see Figure 3.25) on uncoupled walls and a reinforced concrete frame with 100 kN SLB devices (Type 2, Figure 3.26) on the same wall support system. The test results have been used to validate numerical simulations of the system through ABAQUS CAE, a Finite Element Analysis (FEM) software.

The SLB connection type 1 has an initial yielding strength of 125 kN, while the type 2 has an initial yielding force of 250 kN. The material of the steel connections is structural steel ASTM 36, with a nominal strength of 250 MPa.

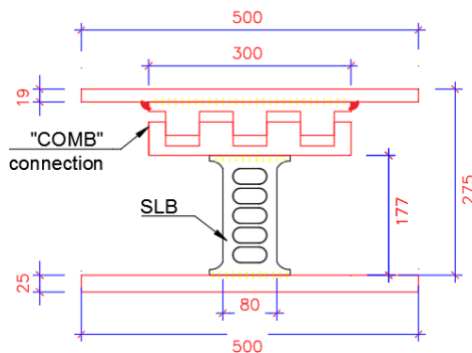


Figure 3.25 Dimensions in mm (left) and SLB connection type 1 (right)

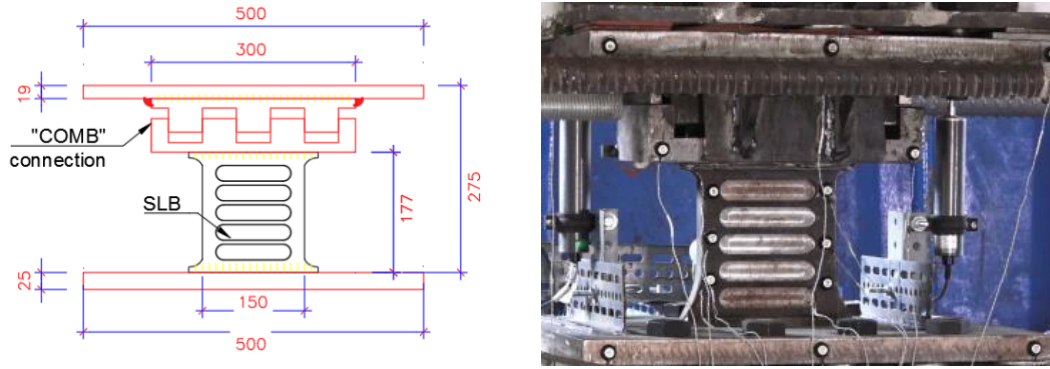


Figure 3.26 Dimensions in mm (left) and SLB connection type 2 (right)

The experimental results of the bare frame exhibit an approximately linear elastic behavior without significant dissipated energy by concrete frame plasticity, as shown in Figure 3.27.

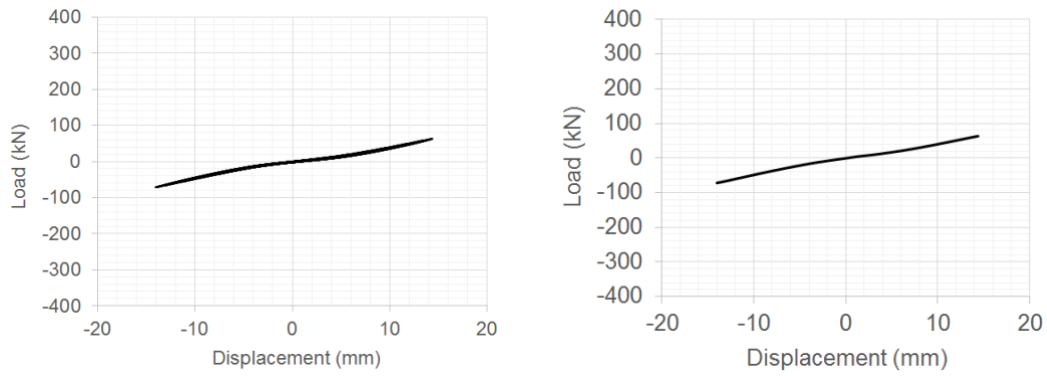


Figure 3.27 Bare concrete frame, hysteresis curve (left) and skeleton curve (right)

Figure 3.28 and Figure 3.29 show hysteresis and skeleton curves for the concrete frame with SLB connections type 1 (Figure 3.28) and type 2 (Figure 3.29).

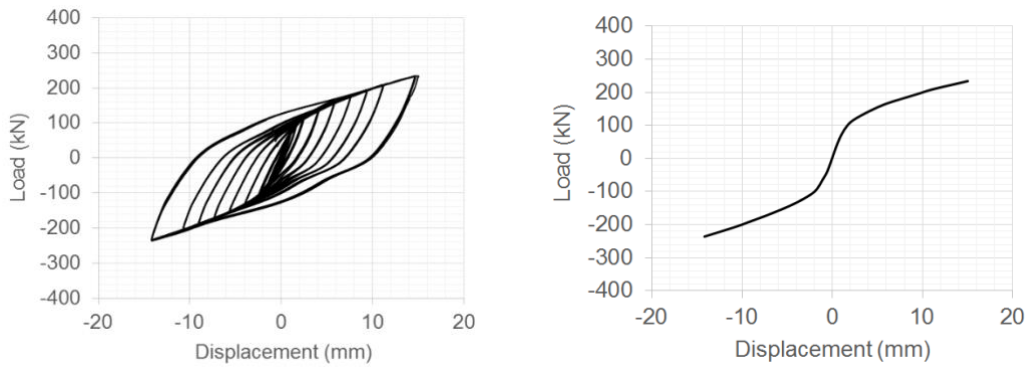


Figure 3.28 Concrete frame with SLB connections type 1, hysteresis curve (left) and skeleton curve (right)

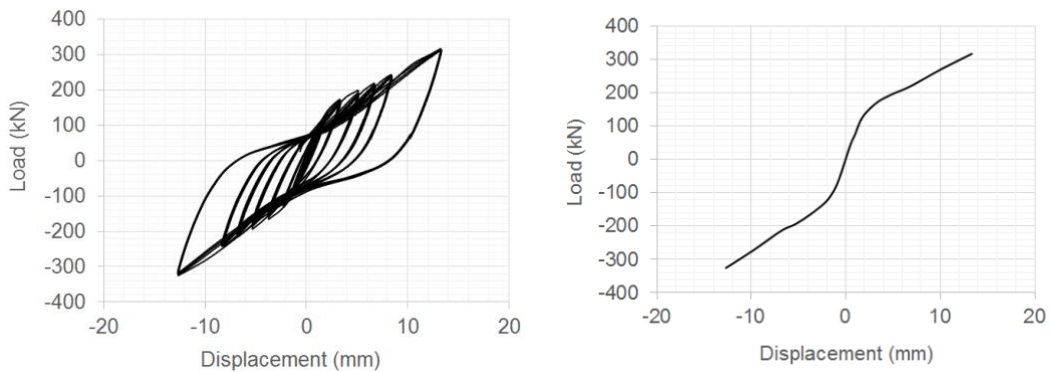


Figure 3.29 Concrete frame with SLB connections type 2, hysteresis curve (left) and skeleton curve (right)

The hysteresis curve shows that structural behavior of concrete frame with SLB connections type 1 exhibit steady hysteresis loops without loss of strength and stiffness degradation, while SLB connections type 2 exhibit hysteresis loops without loss of strength, but with some stiffness degradation.

The finite element analysis software ABAQUS CAE was used to simulate the experimental results of the tests through modeling, analysis, assembling, and visualization of structural components considering only the frame without SLB connections and the frame with SLB connections Type 1, since the one with SLB connections Type 2 showed an unexpected behavior due to the excessive displacements of the connecting plates.

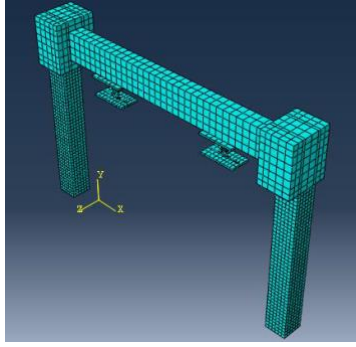


Figure 3.30 Mesh configuration of FE model of the test

Firstly, the bare concrete frame was modelled in order to calibrate the model, and then the uncoupled frame with SLB connections type 1 was modelled until achieving the right behavior of the SLB connections.

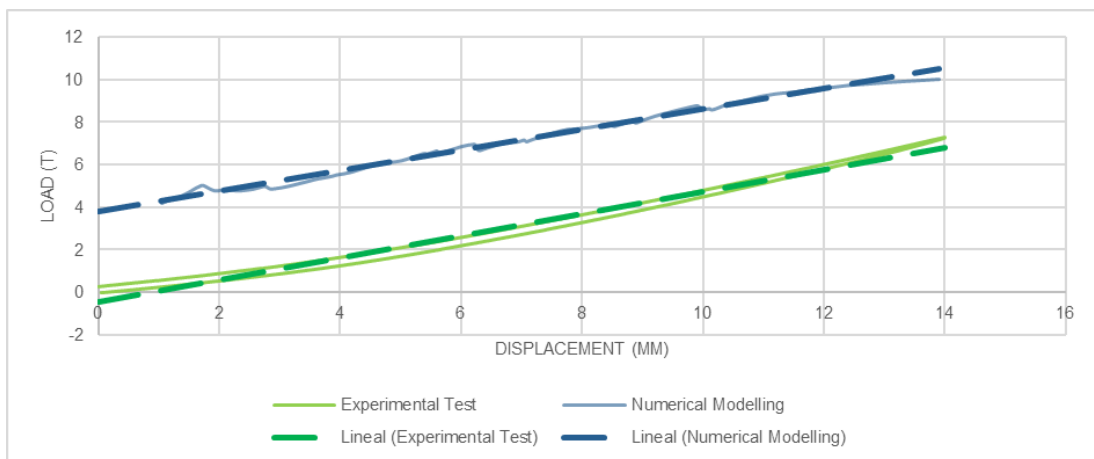


Figure 3.31 Load-displacement relationship of bare concrete frame - Experimental test vs numerical modelling

Regarding the uncoupled frame with SLB connections type 1, through several iterations had been possible to obtain a numerical model that displays a similar behavior to the experimental test. Figure 3.32 shows comparisons between experimental and numerical hysteresis loops.

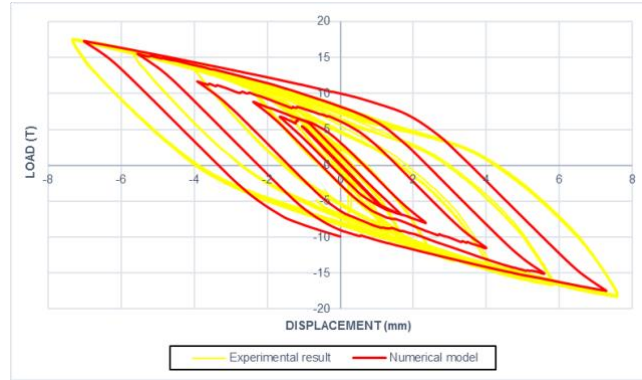


Figure 3.32 Comparison between experimental and numerical hysteresis loop of SLB connections type 1

Figure 3.33 shows that the stress distribution in the SLB connection type 1 is mainly distributed in the “windows” which are the thinner sections; however, it is important to consider that also the upper part of the frames presents high stress levels. Furthermore, the welding sections are subject to minimum levels of stress. On the other hand, sections like steel plate and steel teeth (located over the SLB connection) do not display significant stress distribution.

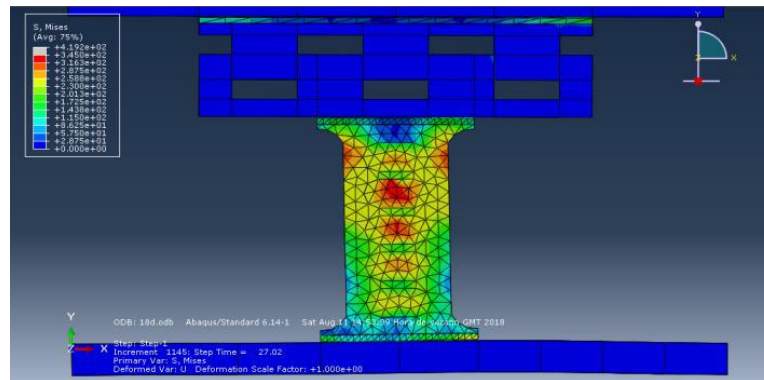


Figure 3.33 Von Mises stresses for the SLB connection type 1

Finally, a model using fixed supports was implemented as shown in Fig. 19 and it shows that using good connections between the reaction wall and the SLB devices, the behavior of the SLB connections is improved significantly, reaching values of 140% of the load capacity of the model using spring supports. For this reason, the connection stiffness represented a significant parameter for future tests.

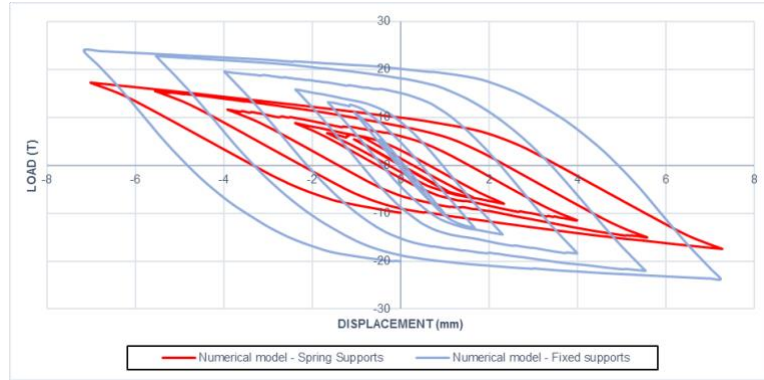


Figure 3.34 Comparison between spring supports and fixed supports in numerical model

### 3.2.4 Fourth generation

The tests of the 4<sup>th</sup> generation of SLB devices were performed at the University of Cantabria, Spain in November 2020 (Bozzo Guillermo, 2021). The main objective of the 4<sup>th</sup> generation was to increase the deformation capacity of the device. For this reason, the height of the device had been increased from the 155 mm of the previous generation to the 270 mm and the width of the dissipative windows from 25 mm to 50 mm, in order to avoid buckling problems. The two geometries of the devices proposed for the tests are shown in Figure 3.35.

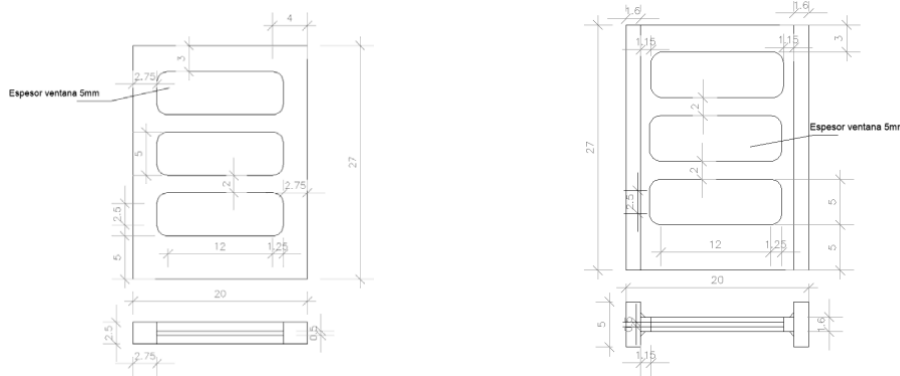
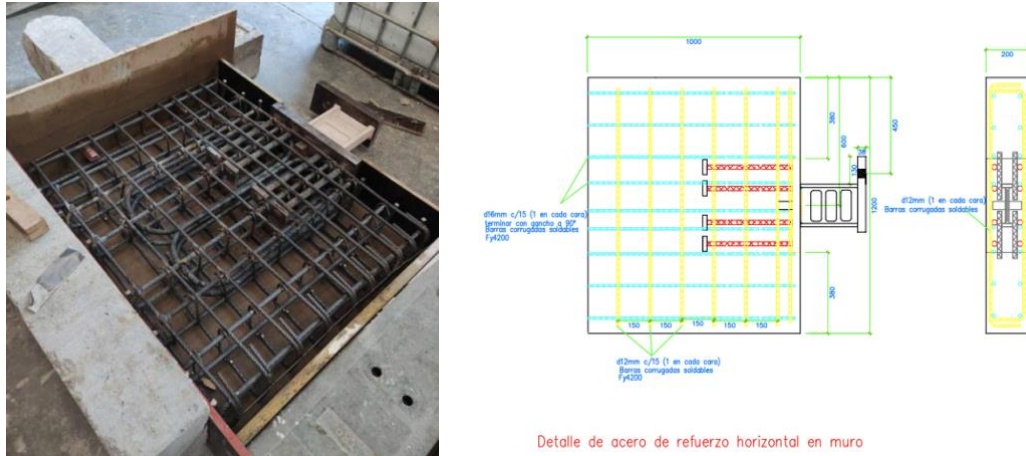


Figure 3.35 Geometries of the devices proposed for the tests

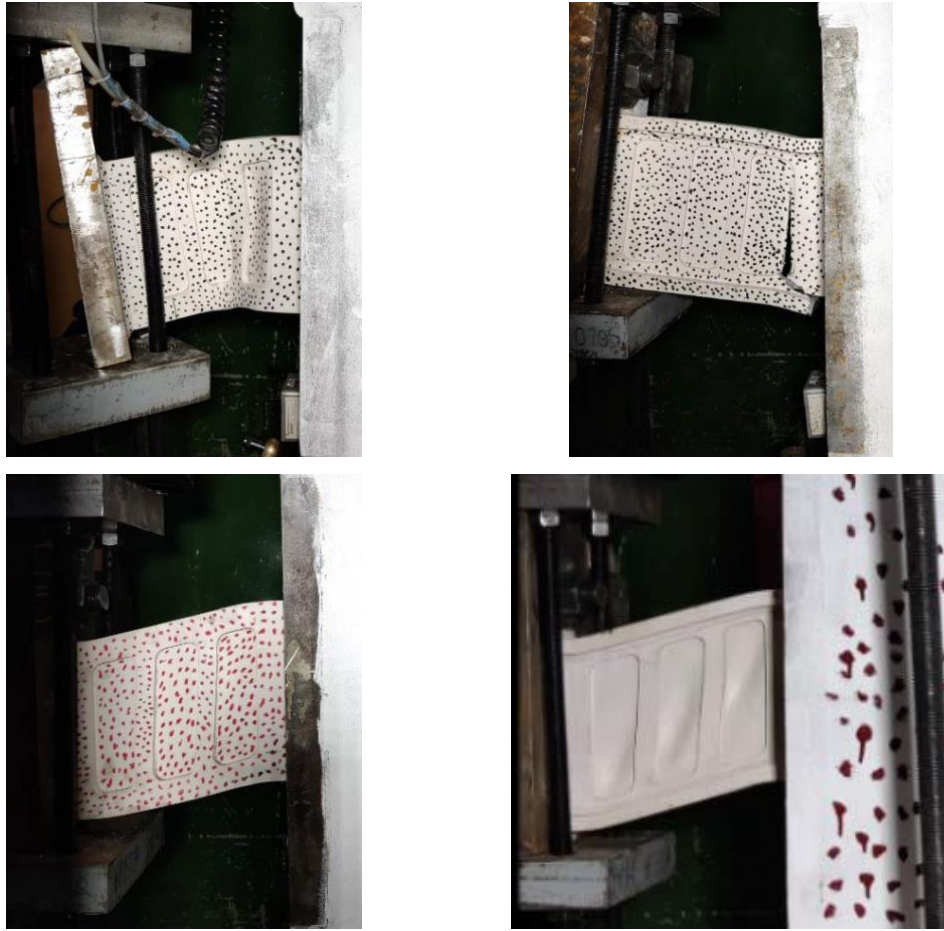
The tests configuration of the device consisted in a dissipator connected to a concrete wall and subjected to cyclic loads applied to the free end of it. The device is welded to a steel plate anchored to the wall through steel rebars, designed accordingly to the ACI 318-19.



*Figure 3.36 Steel reinforcement details in the concrete wall*

A total of four experimental tests had been carried out, involving the two alternatives of SLB in Figure 3.35. The results obtained had been used for the calibration of the finite element model defined in Diana FEA software in order to study the behavior of the devices.





*Figure 3.37 Experimental tests*

Although four tests have been carried out, the numerical-experimental correlation had been obtained using only the results of the second and third test, that were the most representative of the two proposed geometry alternatives. Figure 3.38 compares the hysteretic behavior of the specimen with the results of the finite element model showing a good agreement. In particular, the comparison shows that a simple Von Mises isotropic hardening model is enough to model the behavior of the device.



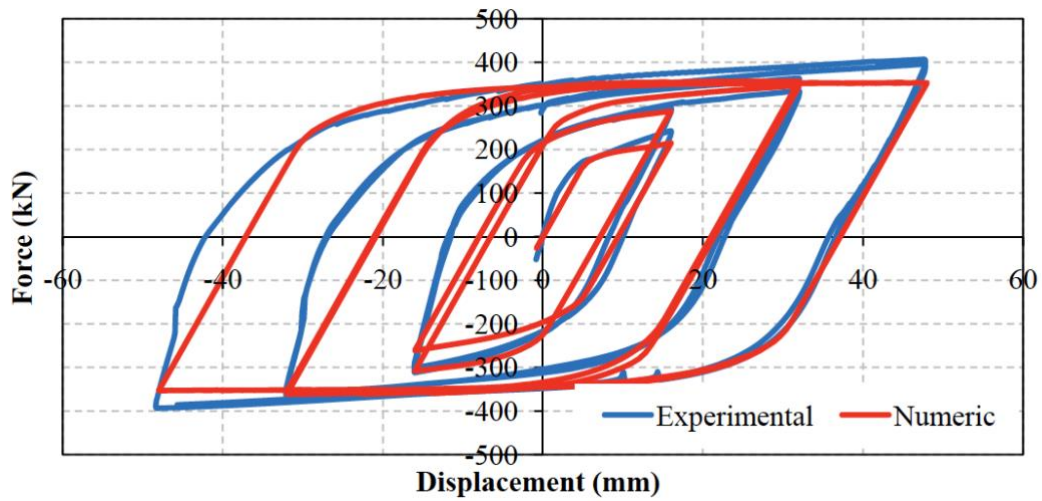


Figure 3.38 Force-displacement relationship for SLB device (Bozzo et al., 2021)

### 3.3 Design table for Shear Link Bozzo device

The experimental campaign led to the definition of a design table for each generation of the device. Following Table 3.1 gives the geometric and mechanical properties of the 4<sup>th</sup> generation dissipator, where  $K_1$  is the initial elastic stiffness,  $K_2$  is the post-elastic stiffness after the yielding,  $D_y$  is the yield displacement of the device,  $F_y$  is the corresponding yielding force and  $F_{\max}$  is the maximum force acting in the SLB.

*Table 3.1 Design Table for 4th generation of Shear Link Bozzo devices*

Device	$K_1$ (KN/cm)	$K_2$ (KN/cm)	$D_y$ (mm)	$F_y$ (KN)	$F_{max}$ (KN)
SLB4_10_5	2026.65	21.62	0.749	151.79	250.00
SLB4_10_6	2163.53	22.90	0.742	160.54	265.78
SLB4_15_5	2472.60	24.85	0.720	177.92	293.72
SLB4_15_6	2761.73	26.96	0.706	195.09	320.62
SLB4_15_7	3021.88	28.76	0.697	210.76	345.09
SLB4_20_6	3361.00	33.09	0.687	230.93	381.61
SLB4_20_7	3700.15	35.28	0.673	248.98	410.70
SLB4_25_6	4260.80	42.53	0.654	278.74	468.96
SLB4_25_7	4767.68	46.51	0.638	304.31	512.31
SLB4_25_8	5238.65	50.43	0.626	327.73	552.76
SLB4_30_7	5785.96	57.25	0.619	358.28	611.14
SLB4_30_8	6419.52	62.36	0.608	390.28	665.17
SLB4_30_9	6994.22	66.79	0.601	420.37	716.61
SLB4_30_10	7535.22	70.90	0.596	449.29	764.52
SLB4_40_7	7797.49	78.07	0.596	464.68	807.56
SLB4_40_8	8718.88	86.41	0.588	512.48	890.20
SLB4_40_9	9580.18	93.66	0.582	557.71	966.06
SLB4_40_10	10439.63	101.20	0.576	601.31	1043.20
SLB4_40_11	11253.53	109.93	0.571	643.06	1117.73
SLB4_40_12	12033.64	115.64	0.570	685.73	1191.30
SLB4_50_9	12289.99	120.57	0.578	709.95	1236.23
SLB4_50_10	13421.60	130.96	0.572	768.20	1340.09
SLB4_50_11	14537.41	141.39	0.569	827.48	1443.52
SLB4_50_12	15599.37	150.54	0.567	884.08	1540.02
SLB4_60_5	8891.13	91.74	0.598	531.45	932.94
SLB4_60_6	10457.28	106.25	0.586	613.19	1078.09
SLB4_60_11	17684.45	174.36	0.562	993.08	1746.50
SLB4_60_12	19029.62	185.88	0.560	1065.32	1868.98
SLB4_65_11	19829.08	194.60	0.562	1113.76	1957.04
SLB4_65_12	21326.70	209.74	0.560	1194.73	2103.54
SLB4_65_13	22872.65	223.05	0.558	1276.57	2245.62
SLB4_65_14	24379.36	235.06	0.556	1356.52	2382.04
SLB4_65_15	25869.86	249.17	0.554	1433.77	2519.93
SLB4_65_16	27331.55	261.77	0.553	1511.96	2654.85
SLB4_65_18	30180.37	286.67	0.554	1671.12	2912.47
SLB4_65_20	32951.18	306.56	0.553	1822.60	3157.88

## 4 MODELLING AND DESIGN OF SLB DEVICE

### 4.1 SLB device mathematical modelling

The Shear Link Bozzo device is characterized by a high initial elastic stiffness and a high plastic deformation capacity. Therefore, the device exhibits a ductile behavior, as depicted in the force-displacement relationship in Figure 4.1.

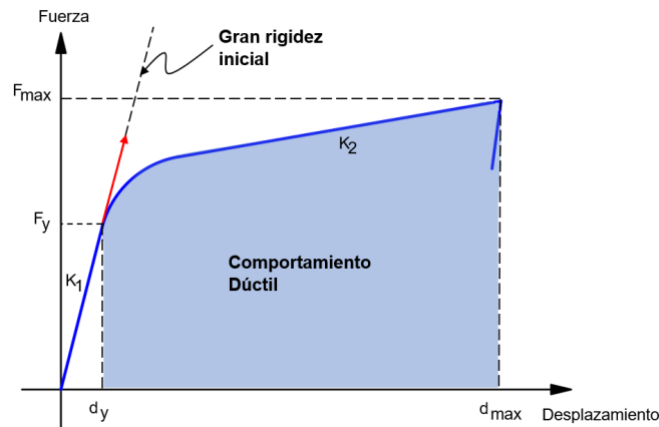


Figure 4.1 Force-displacement relationship of the SLB device

For its mathematical modelling, the SLB device can be easily modelled as an elasto-plastic element through the definition of an elastic stiffness  $K_1$  and a post-elastic one  $K_2$  after the yielding, as shown in Figure 4.2.

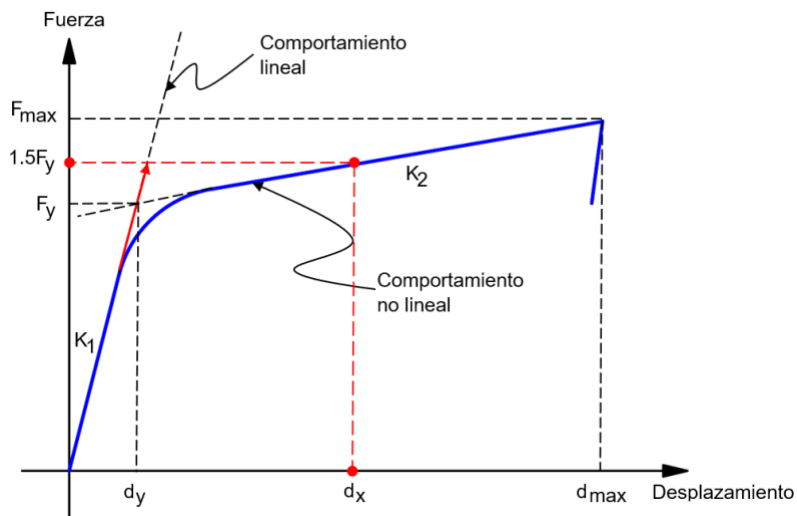


Figure 4.2 Elasto-plastic force-displacement relationship

Considering the force-displacement relationship in Figure 4.2, the SLB device can be represented as two springs in parallel, respectively of stiffness  $K_{sec}$  and  $(K_1 - K_{sec})$ , where the second spring works in series with a rigid-plastic device characterized by a yielding force  $F_y$ .

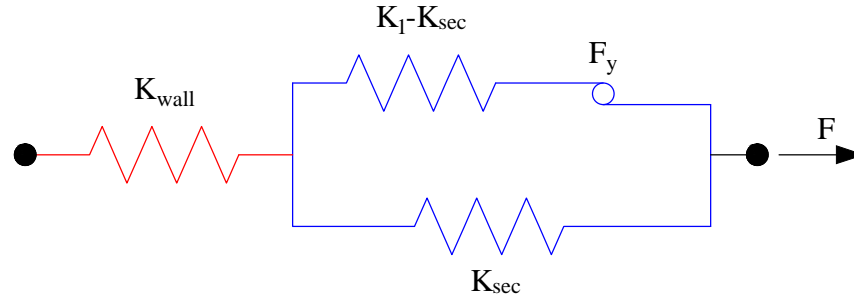


Figure 4.3 SLB device mathematical modelling

Therefore, the equivalent stiffness of the device is equal to:

$$\begin{aligned} K_{eq,SLB} &= K_1 \quad \text{for } F \leq F_y \\ K_{eq,SLB} &= K_{sec} \quad \text{for } F > F_y \end{aligned} \quad (4.1)$$

where  $K_{sec}$  is the secant stiffness, that depends from the displacement of the device, and can be calculated accordingly to the following expression:

$$K_{sec} = K_2 + (K_1 - K_2) \cdot \frac{d_y}{d} \quad (4.2)$$

The decoupled wall can be considered as a spring that works in series with the SLB device. Thus, the equivalent stiffness of the system device-supporting wall can be calculated with the following expression:

$$\frac{1}{K_{eq}} = \frac{1}{K_{eq,SLB}} + \frac{1}{K_{wall}} \rightarrow K_{eq} = \frac{K_{eq,SLB} \cdot K_{wall}}{K_{eq,SLB} + K_{wall}} \quad (4.3)$$

The stiffness of the wall can be calculated with the following expression:

$$K_{wall} = \frac{E \cdot t_w}{4 \left( \frac{h_w}{l_w} \right)^3 + 3 \left( \frac{h_w}{l_w} \right)} \quad (4.4)$$

where  $E$  is the concrete Young's modulus,  $h_w$ ,  $l_w$  and  $t_w$  are respectively the height, length and thickness of the wall.

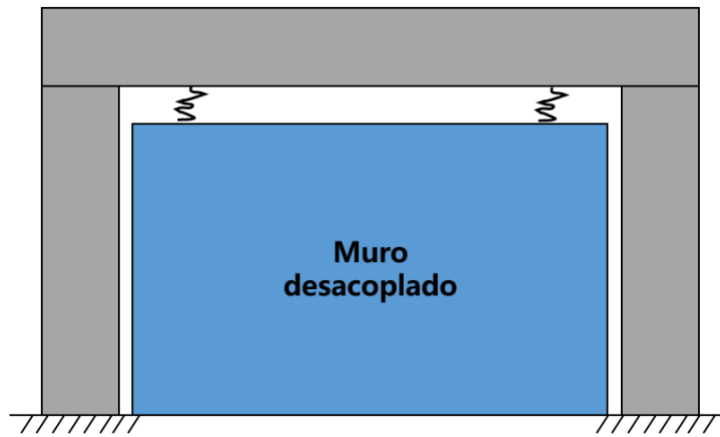


Figure 4.4 Scheme of the system device - decoupled concrete wall

## 4.2 SLB device finite element modelling

The behavior of SLB device can be numerically characterize by using FRAME or NLINK elements. Usually, the first analysis with these devices is a spectral modal linear analysis, so both elements are correct to start with, anyway the NLINK elements provide similar results of FRAME ones and also leave the model prepared for later nonlinear time history analysis. Programs such as SAP2000 or ETABS offers different types of NLINK models. To represent steel yielding dissipators such as SLBs, the plasticity model used is based on a hysteretic behavior proposed by Wen, which simulates the behavior of such devices with great precision. In this thesis, the analyses are carried out using the software ETABS, in particular considering the SLB application to the structure through decoupled concrete walls. For this reason, the following paragraphs describe the modelling and design of SLB dissipators with particular reference to this application.

### 4.2.1 Wen plasticity model

The plasticity model is based on the hysteretic behavior proposed by Wen (1976) and it is represented in Figure 4.5 (CSi Reference Manual., 2017).

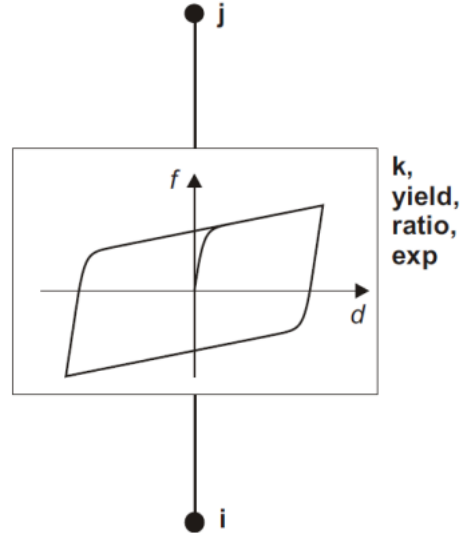


Figure 4.5 Wen Plasticity Property Type for Uniaxial Deformation

For each deformational degree of freedom, it is possible to specify independent uniaxial plasticity properties. All internal deformations are independent, so the yielding at one degree of freedom does not affect the behavior of the other deformations. When nonlinear properties for a degree of freedom are not specified, that degree of freedom is considered linear using the effective stiffness.

The non-linear force-deformation relationship in the Wen plasticity model is given by the following expression:

$$f = \alpha \cdot k \cdot d + (1 - \alpha) \cdot f_y \cdot z \quad (4.5)$$

where  $k$  is the elastic spring constant,  $f_y$  is the yield force,  $\alpha$  is the specified ratio of post-yield stiffness to elastic stiffness ( $k$ ) and  $z$  is an internal hysteretic variable that has a range of  $|z| \leq 1$ , with the yield surface represented by  $|z| = 1$ . The initial value of  $z$  is zero, and it evolves according to the following differential equation:

$$\dot{z} = \frac{k}{f_y} \cdot \dot{d}(1 - |z|^n) \quad \text{if} \quad \dot{d} \cdot z > 0$$

$$\dot{z} = \frac{k}{f_y} \cdot \dot{d} \quad \text{otherwise}$$
(4.6)

where  $n$  is an exponent greater than or equal to unit. Larger values of this exponent increase the sharpness of yielding as shown in Figure 4.6. The practical limit for this exponent is about 20, but for the particular case of the SLB dissipator, it is recommended to use an exp value equal to 2.

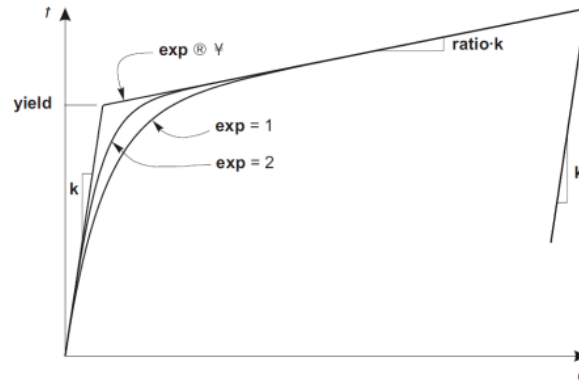


Figure 4.6 Definition of parameters for the Wen Plasticity Property

### 4.2.2 Link properties

The most useful methodology to define the SLB device in a FEM software (e.g., ETABS) consists in the use of a link (Bozzo et al., 2019). In particular, ETABS allows to define the device as an NLINK element, using the elastic properties of the element for linear analyses and the Wen plasticity model introduced in section 4.2.1 for the nonlinear analyses. With regard to the definition of the NLINK element, an important parameter is the so-called “shear deformation location” or “null moment point”. It is defined in ETABS, as shown in Figure 4.7, as the distance to the inflection point or where the moment due to shear on the link is zero. This distance needs to be measured from the end point of the link. It is important to highlight that in the case of the SLB device, the “null moment point” corresponds to the battlement connection, therefore this distance is equal to zero or to the height of the device, depending on how the link is defined or inserted. Therefore, depending on the battlement connection, the NLINK

must be directed up or down. Specifically, in the case of decoupled walls SLB devices are modelled as a link with properties on local axis 2 and their insertion point, or joint i, of the NLINK corresponds to the upper end of the wall and joint j corresponds to the beam base, where there is the null moment point of the link.

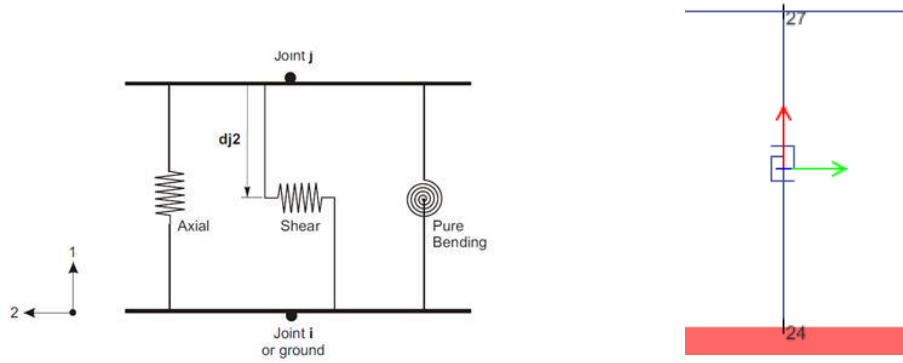


Figure 4.7 SLB modelling as NLink element in ETABS

In local directions 1 and 3, the displacement of the link could be restricted using the “fixed” sections, but it is recommended to assign a sufficiently low stiffness to limit the displacement (e.g., 10 kN/cm) or better still calculate it according to the connection plates, without affecting the result globally.



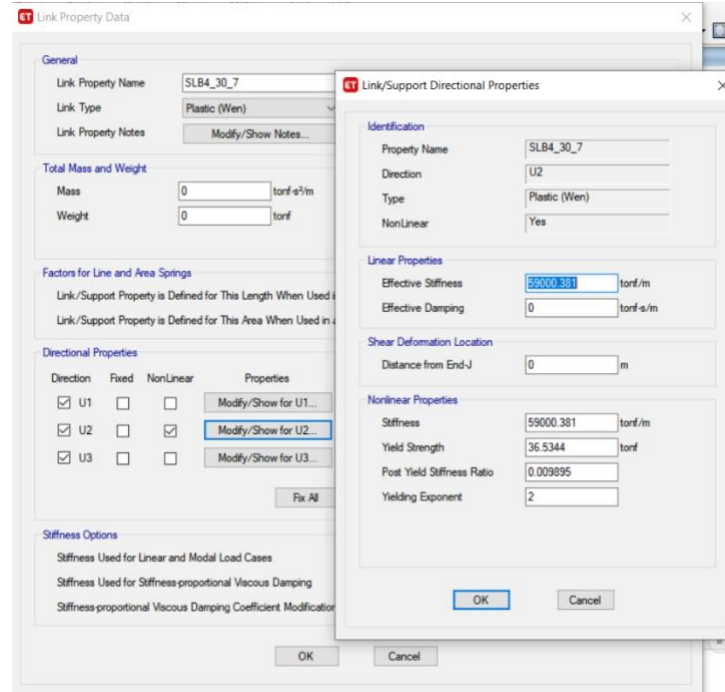


Figure 4.8 Assignment of the lateral stiffness of the Nlink for the local axis - ETABS

In the “DISSIPATE-SLB” plugin the values of lateral stiffness are incorporated in the loaded tables and are calculated based on the upper connection plates.

### 4.3 Iterative design methodology

The following paragraphs present two different design methods, the direct iteration method and the inverse iteration method, of SLB devices. These procedures have been also implemented in the ETABS software through the “DISSIPATE-SLB” plugin. Both of them are based on elastic modal analysis, which replace procedures that make use of nonlinear time history analysis, thus achieving significant savings in computational time for the solution. This is particularly useful in preliminary design, where most important decisions are taken.

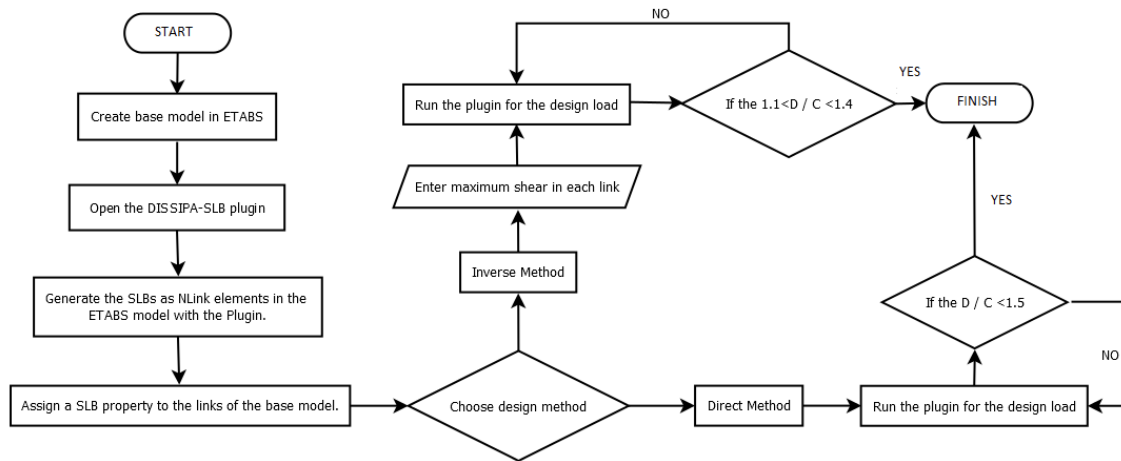


Figure 4.9 Flowchart for the design of SLB dissipators using DISSIPALB plugin for ETABS

### 4.3.1 Direct iteration method

The direct method consists in iterating a group of devices, that were previously defined, by means of a series of a spectral modal linear analysis seismic analysis, until reaching a shear demand ratio compatible with the capacity of the device. More specific, it is required that the ratio between the acting shear and the yield force of the device be less or equal than a certain demand/capacity ratio typically assumed as 1.5. This value is considered correct by various cumulative factors such as the kinematic hardening of the steel or its greater resistance to dynamic loads; these factors could be considered only through nonlinear time history analysis, which it is highly recommended to perform at the end of the design procedure to verify the structural behavior of the building.

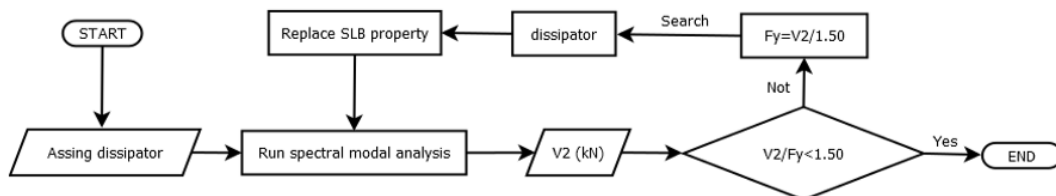


Figure 4.10 Flow chart of direct iteration method

The design process is iterative because changing the devices involves a variation in the stiffness of the structure and implies the need to recalculate seismic forces on the structure to verify again the demand/capacity ratio.

The screenshot shows the 'DISSIPATA SLB v2020.0.0' software window. The 'Direct Iteration' tab is active. On the left, there are settings: 'Load Combination' set to 'ENVE', 'Type of Dissipator' set to 'SLB', 'D/C Ratio' set to '1.5', 'Mode Ejecute' set to 'Automatic', and 'Number of iterations' set to '1'. The main table displays the results of the iteration process.

	$V_{max}$ (kN)	Dissipator ETABS	$F_y$ (kN) ETABS	$F_y$ max (kN) ETABS	$V_2$ (kN) It.	D/C It.	Dissipator It.
	12.39	SLB3 25_5	319.00	592.39	449.30	1.41	Ok!
	16.49	SLB3 25_4	279.60	526.49	417.30	1.49	Ok!
	1.01	SLB2 6_2	35.60	69.01	0.04	0.00	Ok!
	12.39	SLB3 25_5	319.00	592.39	472.81	1.48	Ok!
	16.49	SLB3 25_4	279.60	526.49	415.98	1.49	Ok!
	15.63	SLB3 25_6	357.10	655.63	521.38	1.46	Ok!
	15.63	SLB3 25_6	357.10	655.63	511.00	1.43	Ok!
	1.01	SLB2 6_2	35.60	69.01	0.09	0.00	Ok!
	6.83	SLB3 25_7	394.50	716.83	564.46	1.43	Ok!
	15.63	SLB3 25_6	357.10	655.63	514.00	1.44	Ok!
	16.40	SLB3 25_8	430.70	776.40	613.01	1.42	Ok!
	16.40	SLB3 25_8	430.70	776.40	604.05	1.40	Ok!
	1.01	SLB2 6_2	35.60	69.01	0.08	0.00	Ok!
	18.79	SLB3 30_7	461.30	838.79	650.89	1.41	Ok!
	16.40	SLB3 25_8	430.70	776.40	596.14	1.38	Ok!
	15.50	SLB3 30_8	508.00	915.50	702.25	1.38	Ok!
	18.79	SLB3 30_7	461.30	838.79	678.50	1.47	Ok!

Figure 4.11 Direct iteration method - Dissipa plug-in for ETABS

Once defined the dimensions of SLB devices, it is possible to design the walls considering the maximum force value that could act on them. The shear capacity of a structural concrete wall according to the ACI code can be calculated with the following expression (units in MPa):

$$V_d = 0.75 \cdot 0.83 \cdot \sqrt{f_{ck}} \cdot L \cdot t \quad (4.7)$$

where:

- $f_{ck}$  is the compressive strength of the concrete;
- $L$  is the length of the wall;
- $t$  is the thickness of the wall.

The shear capacity of each concrete wall, calculated with the eq. (4.7), must be greater than the maximum force that could act on the devices. The iterative iteration procedure usually increases the size of the dissipator at each iteration, for this reason has been developed the inverse iteration procedure, which is described in the next paragraph.

### 4.3.2 Inverse iteration method

The “fixed force” or “reverse” iterative procedure is an alternative to the “direct iteration” one to limit the thicknesses of the decoupled walls and size of the devices since the direct procedure consecutively increases its dimensions. Actually, thicknesses of uncoupled concrete walls greater than 300 mm are usually excessive due to architecture and cost. According to the ACI code, as shown in the eq. (4.7), the shear capacity of a concrete wall, considering a certain value of  $f_{ck}$ , length and thickness, is fixed and, according to this capacity, is also fixed the maximum force that could act on the devices. It is important to highlight that due to the fact that the special battlement connection does not transfer axial force, there is a direct isostatic equilibrium relation between the dissipators shear force and the shear at the supporting concrete wall. Unlike the direct iteration procedure, which usually increases the size of the dissipator at each iteration, as well as its shear force, in the iterative reverse procedure, the value of the shear force in the dissipator is set and, therefore, the method consists in reducing the size of the device in the numerical model, but not in reality, in order to calibrate such transferred shear force.

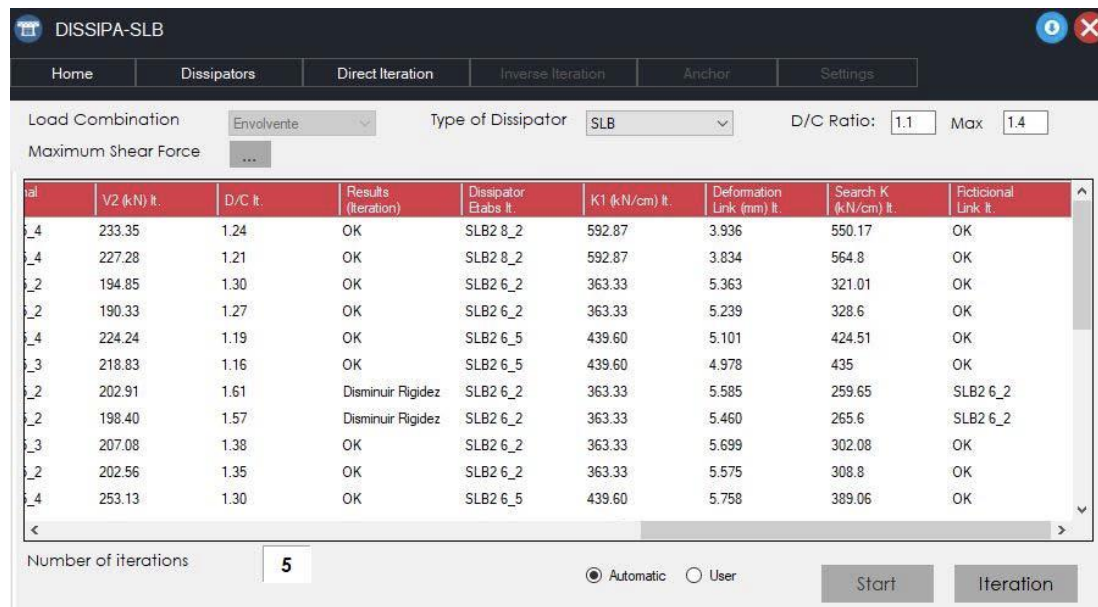


Figure 4.12 Inverse iteration method - Dissipa plug-in for ETABS

The selection procedure of the SLB devices is always performed by means of a spectral modal linear analysis that allows a reduced computation time and can be summarized in the following steps:

1. Definition of a type of SLB device (e.g., SLB 30\_3) and a preliminary wall thickness (e.g., 150 mm).
2. A direct iteration procedure is initially implemented in order to verify the design parameters to be controlled, usually the inter-story drift. If necessary, it is possible to increase the number of devices or the thickness of the decoupled walls in order to reduce the inter-story drift to verify the local design requirements; in other cases, it may be necessary to increase the number of decoupled walls. Moreover, it is necessary to check the capacity ratio limits in the range 1.1-1.4 to proceed to modify the selected devices in the analysis.
3. The total shear force in the decoupled wall should be checked at each step according to the expression:

$$V_d = 1.5 \cdot F_y \cdot n_{SLB} \quad (4.8)$$

where  $F_y$  is the yield strength of each device, 1.5 is an additional safety factor to those corresponding to ELUs and  $n_{SLB}$  is the number of the devices on the wall.

4. The maximum shear force in the decoupled wall, evaluated with the eq. (4.8), must comply with its shear capacity, that can be evaluated according to the ACI code and which depends on the length and thickness of the wall and the resistance of concrete (units in MPa):

$$V_d = 0.75 \cdot 0.83 \cdot \sqrt{f_{ck}} \cdot L \cdot t \quad (4.9)$$

For steel braces the expression is similar, but depends on the buckling strength of the diagonals, so the system is similar to the BRB or "Buckle Restrained Braces".

5. In the case that the wall thickness cannot be increased, as in the second instance the concrete resistance of the wall, it necessary to proceed with the reverse iteration procedure with the aim to limit the force on the decoupled wall.
6. The shear capacity of the wall is fixed as previously established (eq. (4.9)) and considering this the following expression is developed to calculate the maximum force in each wall device:

$$F_{max,SLB} = \frac{0.75 \cdot 0.83 \cdot \sqrt{f_{ck}} \cdot (L \cdot t)_{wall}}{1.5 \cdot n_{SLB}} \quad (4.10)$$

This is the maximum target force which corresponds to a specific type of device and which would be the one finally employed in the design.

7. Therefore, the device is selected using the table of SLB devices in such a way that its  $F_y$  is the one immediately below  $F_{max,SLB}$ . There is usually more than one option for this selection, for this reason it is recommended to choose the device with the highest window thickness for its lower cost. At this point the inter-story drift must be verified again because it could be that the force is too low and the drift limit of the design code is not met.
8. Since the spectral modal analysis is linear, the acting force in each device has no limit, so when the device is selected in the step 7 and the analysis is repeated, the acting shear will change and most likely exceed the demand/capacity limit established from 1.1-1.4. One solution is to “fictitiously” reduce the size of the device in the RSA numeric model and repeat the analysis until a shear force is obtained within the established range.

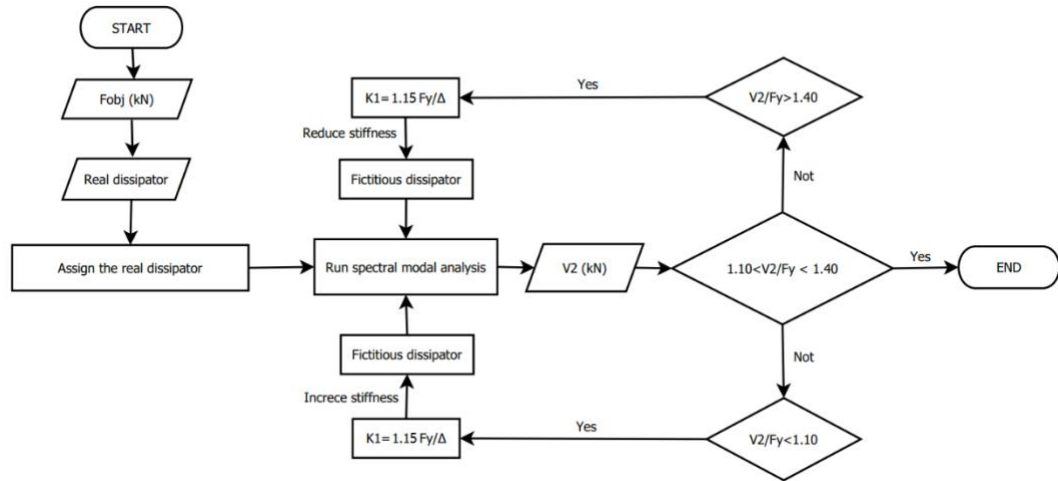


Figure 4.13 Flow chart of inverse iteration method

Actually, the inverse iteration procedure has two important stages: first, the target force is fixed on each device and through linear spectral modal analysis it is iterated with “fictitious” dimensions until a demand capacity shear ratio within the range of 1.1-1.4. The force in the device must be greater than its  $F_y$  to ensure its influence in a seismic event. Moreover, the upper limit to demand-capacity ratio of 1.4 is established

---

because the analysis used is linear elastic, therefore the shear difference between the one obtained with the spectral modal analysis and the shear capacity transferred by the devices is equivalent to a lower actual stress in the rest of the structure. This result is not correct since each device transfers a shear limit that is not counted by a linear spectral modal analysis. The procedure is iterative because the shear force in the device depends largely on its rigidity. Therefore, the change of the device implies a change in the shear force acting in it. The iteration will be repeated until a convergence condition is reached, which usually required only 3 or 4 iterations. This procedure has been implemented in ETABS through the DISSIPATE-SLB plugin. The second stage of this procedure consists in verifying the results by means of a non-linear history time analysis as described in chapters 5 and 6 of this thesis. As indicated, it is always important to remember that the spectral modal analysis, which is used in the first stage of the design, is a linear analysis, so it is not possible to consider the maximum shear force that the device can transfer to the support wall. Therefore, the difference between the shear force acting in the device accordingly to the modal analysis and its maximum capacity will be absorbed by the structure causing a non-conservative situation. For this reason, it is important to verify a maximum force factor of 1.4 between the actual capacity of the device and the shear force acting on its when performing the response spectrum linear analysis. In order to evaluate the actual seismic performance of structures equipped with SLB devices in severe seismic events and validate the design procedure mentioned in the first stage, nonlinear time history analysis (second stage) is performed, but with real devices according to the adopted shear target.

## 5 PERFORMANCE BASED SEISMIC DESIGN APPROACH

### 5.1 Introduction

Performance Based Seismic Design (PBSD) is a structural design methodology that provides greater design flexibility to structural engineers, especially for the design of high-rise buildings. In practice the PBSD approach allows to make exceptions to specific prescriptive code-based approaches, so the focus of the structural engineer changes from a prescriptive “check list” approach of code provisions to requiring more effort in the analysis and design stages, with verification of building performance required at multiple seismic hazard levels using linear and advanced nonlinear analyses. Therefore, PBSD stands in contrast to common analysis and design methodologies such as *Equivalent Lateral Force* (ELF) analysis and *Response Spectrum analysis* (RSA). These are both traditional linear analysis methodologies that use seismic reduction factors to account for energy dissipation through nonlinear behavior. In other words, these methods require to make assumptions about the level of energy dissipation through the definition of a seismic reduction factor ( $R$  factor). The  $R$  factor assumption implies a reasonably well distributed level of energy dissipation in the entire structure. However, this has been shown to be correct for buildings of modest height and conventional geometry, but for high-rise buildings damage levels and locations are not always well predicted by linear methodologies (Golesorkhi et al., 2019).

### 5.2 Performance objectives and levels

The first important consideration when applying PBSD approach is to establish the performance objectives of the structure. Performance objectives can be defined according to specific guidelines, such as ASCE 7 and ASCE 41. ASCE 7 performance objectives are primarily related to minimum life-safety in Design Earthquake (DE) level event associated to the specific Risk Category of the building. ASCE 41 identifies a series of performance objective targets that can be related to specific levels of seismic intensities. In particular, ASCE 41-13 reports the descriptions of anticipated levels of



structural and non-structural damage under each performance objectives, as show in Table 5.1.

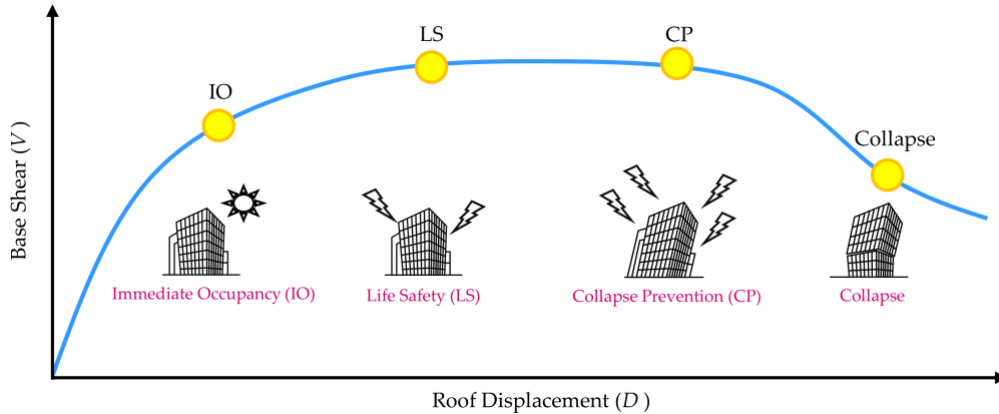


Figure 5.1 Structural Performance Objective Illustration (Golesorkhi et al., 2019)

Table 5.1 Damage Control and Building Performance Levels from ASCE 41-13

Target Building Performance Levels				
	Collapse Prevention Level (5-D)	Life Safety Level (3-C)	Immediate Occupancy Level (1-B)	Operational Level (1-A)
Overall damage	Severe	Moderate	Light	Very light
Structural components	Little residual stiffness and strength to resist lateral loads, but gravity load-bearing columns and walls function. Large permanent drifts. Some exits blocked. Building is near collapse in aftershocks and should not continue to be occupied.	Some residual strength and stiffness left in all stories. Gravity-load-bearing elements function. No out-of-plane failure of walls. Some permanent drift. Damage to partitions. Continued occupancy might not be likely before repair. Building might not be economical to repair.	No permanent drift. Structure substantially retains original strength and stiffness. Continued occupancy likely.	No permanent drift. Structure substantially retains original strength and stiffness. Minor cracking of facades, partitions, and ceilings as well as structural elements. All systems important to normal operation are functional. Continued occupancy and use highly likely.
Nonstructural components	Extensive damage. Infills and unbraced parapets failed or at incipient failure.	Falling hazards, such as parapets, mitigated, but many architectural, mechanical, and electrical systems are damaged.	Equipment and contents are generally secure but might not operate due to mechanical failure or lack of utilities. Some cracking of facades, partitions, and ceilings as well as structural elements. Elevators can be restarted. Fire protection operable.	Negligible damage occurs. Power and other utilities are available, possibly from standby sources.
Comparison with performance intended for typical buildings designed to codes or standards for new buildings, for the design earthquake	Significantly more damage and greater life safety risk.	Somewhat more damage and slightly higher life safety risk.	Less damage and low life safety risk.	Much less damage and very low life safety risk.

In the PBS D approach three levels of seismic shaking are considered:

- Risk Targeted Maximum Considered Earthquake ( $MCE_R$ );
- Design Earthquake ( $DE$ );
- Service Level Earthquake ( $SLE$ ).

The  $MCE_R$  shaking level corresponds to the most severe earthquake expected to the site, while the  $DE$  level is defined in ASCE 7 as a shaking having an intensity two-thirds that of  $MCE_R$  one. Finally, the  $SLE$  level corresponds to relatively frequent and

more moderate intensity earthquake shaking. Figure 5.2 shows relationships between performance levels, earthquake intensities, and Risk Category in ASCE 41.

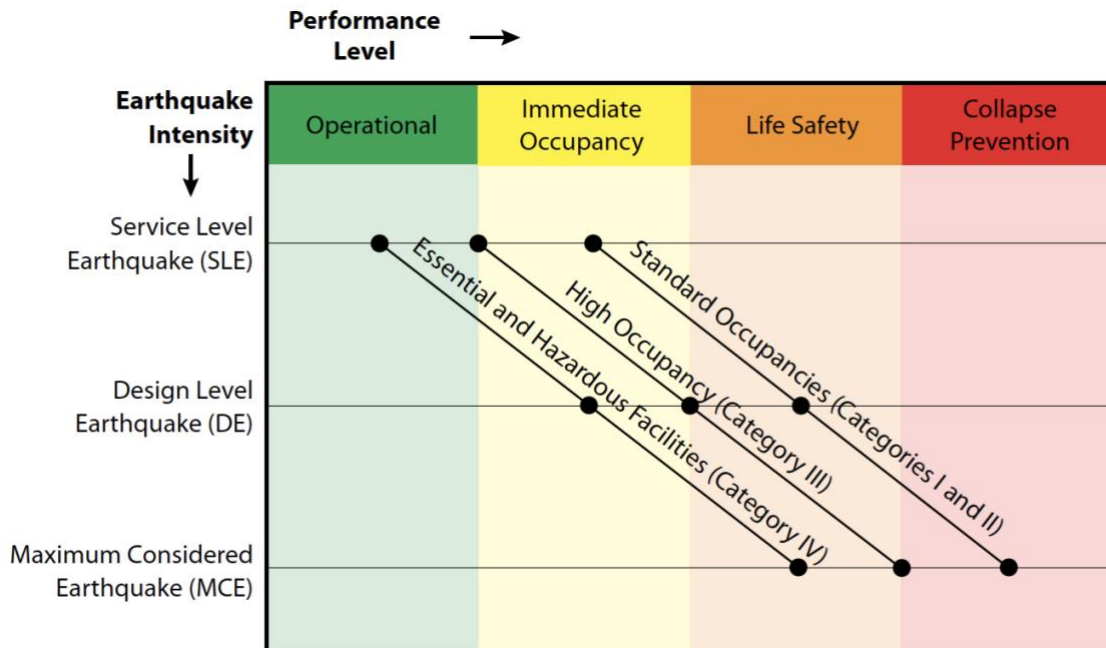
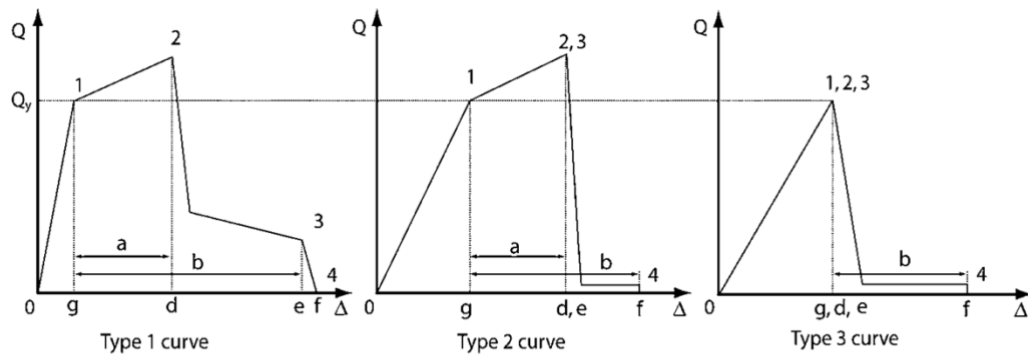


Figure 5.2 Performance Levels of Code-Based Buildings at Various Risk Category Levels as described in ASCE 41 (Golesorkhi et al., 2019)

### 5.3 Acceptance criteria in ASCE 41-13

This paragraph describes the acceptance criteria defined in ASCE 41-13, which has been taken as a reference for the analyses carried out in this thesis work in chapter 7. The acceptability of force and deformation actions shall be evaluated for each component of the structure in accordance with the requirements of ASCE 41-13. Before selecting component acceptance criteria, it is important to classify each component as primary or secondary and each action as deformation controlled (ductile) or force controlled (nonductile). Regarding the first classification, structural components that affect the lateral stiffness and distribution of seismic forces in a structure, giving a significant contribute to achieving the selected performance level shall be classified as primary, while structural components that are not required to resist seismic forces for the structure to achieve the selected performance level shall be classified as secondary. Regarding the second classification, all actions shall be classified as either deformation controlled or forced controlled using the component force versus deformation curves shown in Figure 5.3.



## Notes:

1. Only secondary component actions permitted between points 2 and 4;
2. The force, Q, after point 3 diminishes to approximately zero.

*Figure 5.3 Component Force vs Deformation Curves*

The type 1 curve depicted in Figure 5.3 is representative of ductile behavior where there is an elastic range, from point 0 to 1, and a plastic range, from point 1 to 3, followed by loss of seismic force resisting capacity at point 3 and loss of gravity load resisting capacity at point 4. The plastic range can have either a positive or negative post-elastic slope (points 1 to 2) and a strength-degraded region with nonnegligible residual strength to resist seismic forces and gravity loads (points 2 to 3). Primary component actions exhibiting this behavior shall be classified as deformation-controlled if the plastic range is such that  $d \geq 2g$ , otherwise, they shall be classified as force controlled. Secondary component actions exhibiting this behavior shall be classified as deformation controlled for any  $d/g$  ratio.

The type 2 curve depicted in Figure 5.3 is representative of ductile behavior where there is an elastic range, from point 0 to 1, and a plastic range, from point 1 to 3. The plastic range can have either a positive or negative post-elastic slope (points 1 to 3) followed by substantial loss of seismic force resisting capacity at point 3. Loss of gravity load resisting capacity takes place at the deformation associated with point 4. Primary component actions exhibiting this behavior shall be classified as deformation-controlled if the plastic range is such that  $e \geq 2g$ , otherwise, they shall be classified as force controlled.

The type 3 curve depicted in Figure 5.3 is representative of a brittle or nonductile behavior where there is an elastic range, from point 0 to 1, followed by loss of seismic force resisting capacity at point 3 and loss of gravity load resisting capacity at the

deformation associated with point 4. Primary component actions exhibiting this behavior shall be classified as force controlled. Secondary component actions exhibiting this behavior shall be classified as deformation controlled if  $f \geq 2g$ , otherwise, they shall be classified as force controlled.

Table 5.2 provides some examples of possible deformation and force-controlled actions in common framing systems.

*Table 5.2 Examples of Possible Deformation-Controlled and Force-Controlled Actions*

Component	Deformation-Controlled Action	Force-Controlled Action
<b>Moment frames</b>		
• Beams	Moment ( $M$ )	Shear ( $V$ )
• Columns	—	Axial load ( $P$ ), $V$
• Joints	—	$V^a$
Shear walls	$M$ , $V$	$P$
<b>Braced frames</b>		
• Braces	$P$	—
• Beams	—	$P$
• Columns	—	$P$
• Shear link	$V$	$P$ , $M$
Connections	$P$ , $V$ , $M^b$	$P$ , $V$ , $M$
Diaphragms	$M$ , $V^c$	$P$ , $V$ , $M$

<sup>a</sup>Shear may be a deformation-controlled action in steel moment frame construction.

<sup>b</sup>Axial, shear, and moment may be deformation-controlled actions for certain steel and wood connections.

<sup>c</sup>If the diaphragm carries lateral loads from vertical-force-resisting elements above the diaphragm level, then  $M$  and  $V$  shall be considered force-controlled actions.

Figure 5.4 shows the generalized force versus deformation curves used to specify element modelling and acceptance criteria for deformation-controlled actions. Linear response is depicted between point A and an effective yield point B. The slope from point B to point C is typically a small percentage, from 0% to 10%, of the elastic slope and is included to represent phenomena such as strain hardening. Point C ordinate represents the maximum strength of the element, while its abscissa value corresponds to the deformation at which significant strength degradation begins (line CD). Beyond point D, the element responds with substantially reduced strength to point E. For deformations greater than point E, the element seismic strength is essentially zero. The sharp transition as shown on idealized curves in Figure 5.4 between points C and D can result in computational difficulty and an inability to converge where it is used as

modelling input in nonlinear analysis. To avoid this computational instability, a small slope (e.g., 10 vertical to 1 horizontal) may be provided to the segment of these curves between points C and D.

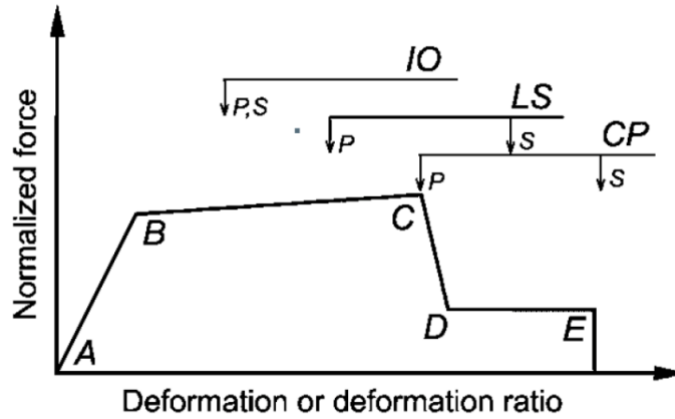


Figure 5.4 Acceptance Criteria for Force-Deformation Relationships

For some components, it is convenient to prescribe acceptance criteria in terms of deformation (e.g.,  $\theta$  or  $\Delta$ ), whereas for others it is more convenient to give criteria in terms of deformation ratios. Acceptance criteria for deformation or deformation ratio for primary components (P) and secondary components (S) corresponding to the target building performance levels of Collapse Prevention (CP), Life Safety (LS) and Immediate Occupancy (OC) as shown in Figure 5.4 are given in ASCE 41-13.

## 5.4 Site specific seismic hazard assessment

The seismic design of structures, especially in the PBSD approach, should always include proper evaluation of seismic hazards (Golesorkhi et al., 2019). PBSD guidelines recommend to establish appropriate site-specific ground motions, rather than using a prescriptive code spectrum, considering all the significant for the structure.

### 5.4.1 Site response spectra

The site response spectrum can be obtained in different ways, such as using probabilistic seismic hazard analysis (PSHA), deterministic seismic hazard analysis (DSHA) or ground response analysis (Golesorkhi et al., 2019). The obtained site

response spectrum is used as a target spectrum from ground motion scaling and matching.

In a PSHA, a level of ground shaking is defined as a probability of exceedance in a given period of time, that for standard occupancies structures corresponds to 50 years. The spectral values are developed for the same mean annual frequency of exceedance, which represents a uniform hazard, hence the term Uniform Hazard Spectrum (UHS). In a DSHA, it is considered the occurrence of an earthquake of a particular magnitude, typically a maximum earthquake on a particular fault and the closest distance to the fault. The main difference between PSHA and DSHA is that the second does not explicitly consider the probability (or frequency) of the occurrence of a particular earthquake.

Ground response analysis is a computational technique based on the theory of wave propagation through the soil. For this analysis, an idealized soil column is shaken by an earthquake time series at the base layer. The nonlinear soil behavior is typically modelled by an equivalent-linear approach or a full nonlinear approach, depending on the expected deformation level reached by the soil.

In the PBSD approach (TBI Guidelines, 2017), two levels of spectral values should be considered:

- $MCE_R$  is defined as a Risk-Targeted PSHA level of shaking having a 2 percent probability of exceedance in 50 years, that corresponds to a 2475-year return period).
- $SLE$  is defined as a PSHA level having a 50 percent probability of exceedance in 30 years, that corresponds to a 43-year return period.

The return period of these two levels of spectral values, if necessary, can be adjusted accordingly to the local building code requirements for the site building.

### 5.4.2 Time series record selection

Proper selection and development of a set of site-specific time series is a critically important step in the PBSD procedure. In this step, the aim is to select time series that have a similar magnitude, distance, fault mechanism and duration as that of the recommended target spectrum. The number of ground motion time series considered in the selection depends on the building code requirements. Each time series needs to

be developed in order to be spectrally compatible to the site-specific target spectrum. Traditionally, two different approaches can be used in developing site-specific time series:

- *spectral matching* approach;
- *spectral amplitude scaling* approach.

In the *spectral matching* approach, the shape of the response spectrum of the original time series is modified to match a target spectrum, as shown in Figure 5.5.

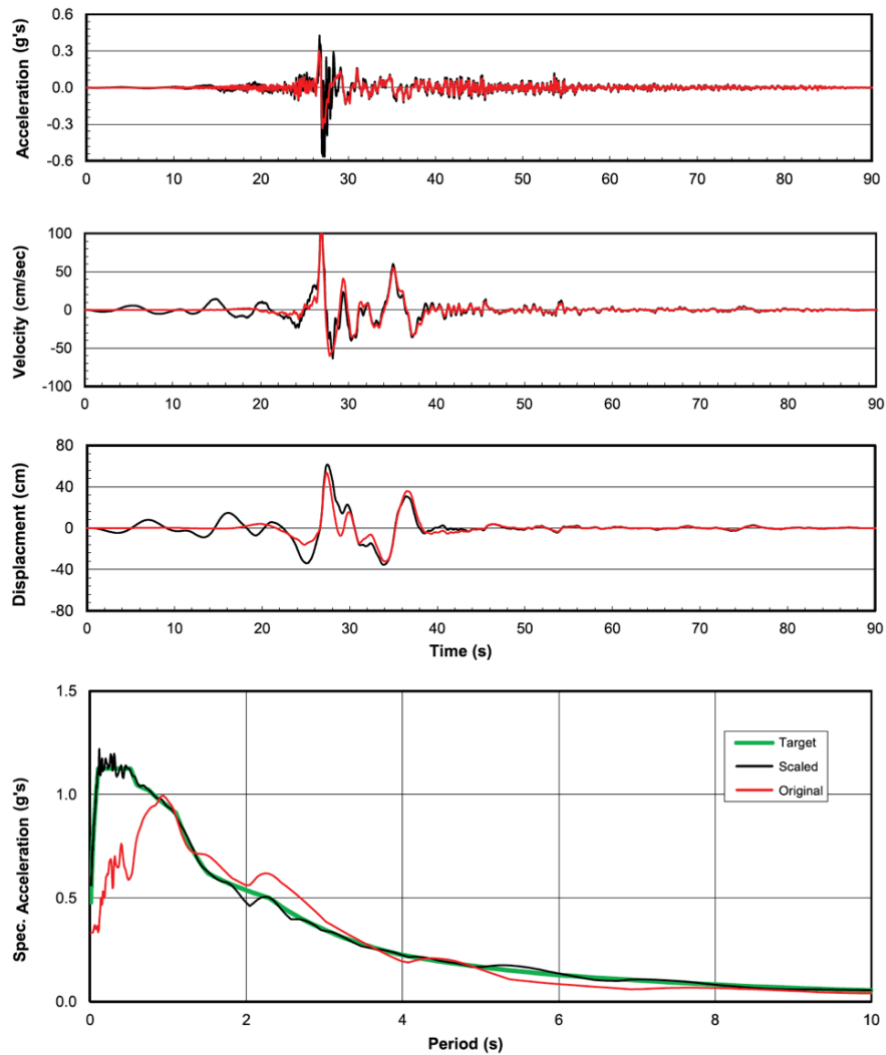


Figure 5.5 Spectrally matched time series (Golesorkhi et al., 2019)

Time or frequency domain matching can be used. In general, a time domain approach is preferred because it minimizes alteration and distortion to the original time series. However, both methods can change the frequency content and characteristics of the

original time series if spectral matching is not done properly. The main advantage of this approach is that the spectrum of the matched time series is consistent with the site-specific target spectrum.

In the *spectral amplitude scaling* approach, a single scalar value is used to modify the spectral values of the original time series. An example of spectrally scaled time series is shown in Figure 5.6.

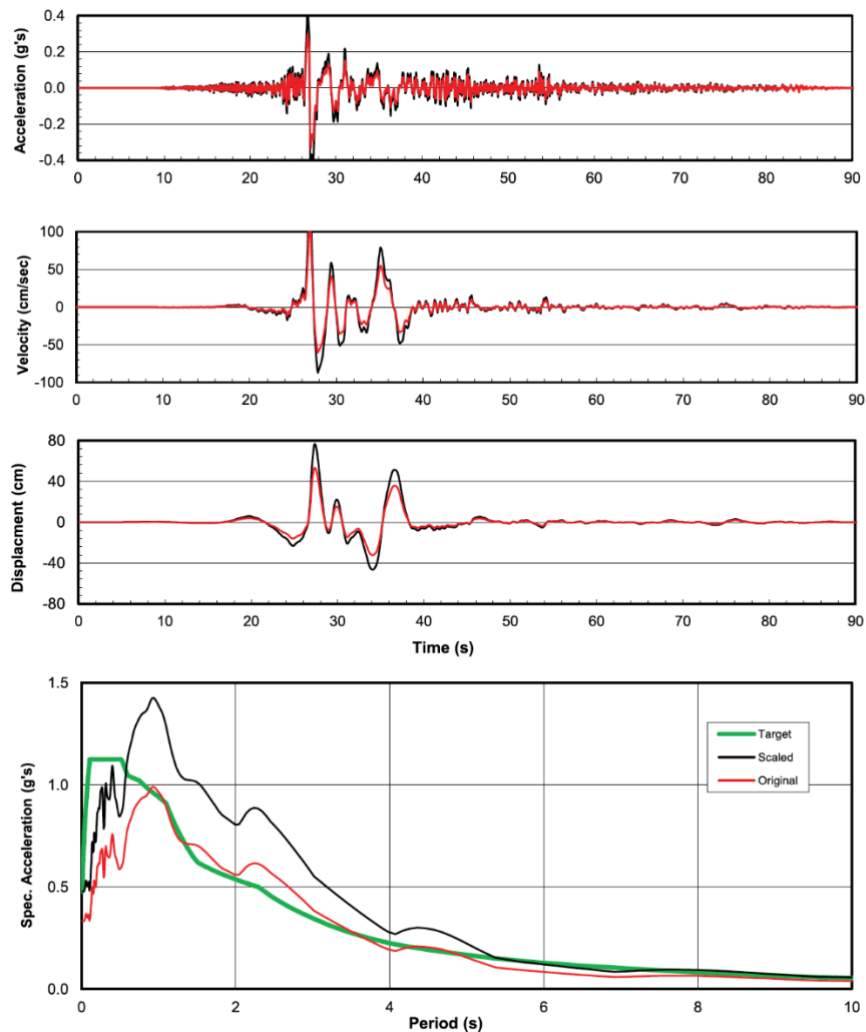


Figure 5.6 Spectrally scaled time series (Golesorkhi et al., 2019)

In this case, considering that the entire original spectrum is scaled by a single value, there could be very large discrepancies between the scaled spectrum and target one at any period. The advantage of this approach is that the characteristics of the time series in terms of shape, relative amplitude and frequency content of the signals, and



spectrum are not altered. However, the amplitude of time series changes accordingly to the scale factor used for the spectral amplitude scaling approach, as shown in Figure 5.6.

## 5.5 PBSD approach procedure

Performance based seismic design approach is typically a two-step process where the structure is first designed using linear analysis methods (e.g., Response Spectrum analysis) and then the design is verified using non-linear time history analyses (Golesorkhi et al., 2019). The design step, that consists in a complete proportioning of all members of the seismic force-resisting system, is typically carried out considering the service-level earthquake (*SLE*) with the aim to verify that the proposed structural system meets the minimum required strength and stiffness for earthquake resistance under *SLE* demands (e.g., Immediate Occupancy performance). It is important to consider that explicit verification of immediate occupancy level would require non-linear time history analyses, using appropriate ground motions. However, as traditionally done in code-based designs, *SLE* structural performance is generally verified using linear Response Spectrum analysis (*RSA*), considering that the structure should perform an essentially elastic response. The wind demand, if it is expected to affect the structural design, must be considered in this step. The intent of designing using *SLE* level demands is to inherently satisfy *DE* performance objectives by verifying the structural performance behavior under *SLE* and *MCE<sub>R</sub>* demands. However, if specific performance objectives are defined at *SLE*, *DE* and *MCE<sub>R</sub>*, verification at each level may be required. In this first step, if *SLE*-level demands are used, drift should not exceed a certain amount percent (e.g., 5 %, depending on the building code) of the story height. After the design of the seismic force-resisting system using linear analysis, it is necessary to conduct the verification of the structural performance under *DBE* and *MCE<sub>R</sub>* level shaking using non-linear time history analyses. The aim of this second step, that is always carried out by non-linear time history analyses, is to verify the structural design of the building, but it could be also necessary to make some design modifications in order to satisfy performance levels.

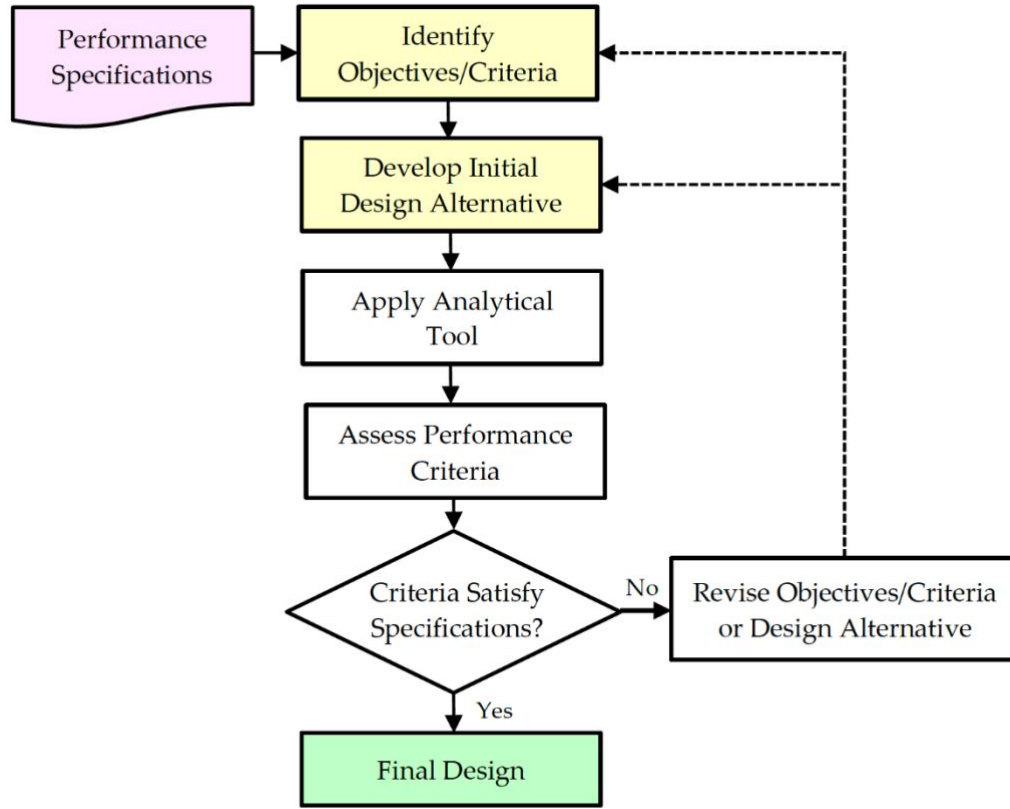


Figure 5.7 Typical flowchart of PBSD approach (Golesorkhi et al., 2019)

A small amount of equivalent viscous damping may be included in linear response spectrum analyses and in linear and nonlinear time history analyses to account for energy dissipation that is not otherwise represented by the analysis model. Unless evidence is provided to justify larger values, effective additional modal or viscous damping shall not exceed the fraction of critical damping given by the following equation:

$$\xi_{crit} = \frac{0.2}{\sqrt{H}} \leq 0.05 \quad (5.1)$$

where  $H$  is the height of the structures in meters. For  $MCE_R$  level, the viscous damping value, calculated with the eq. (5.1), in any case need not be taken less than 0.025 as shown in Figure 5.8.

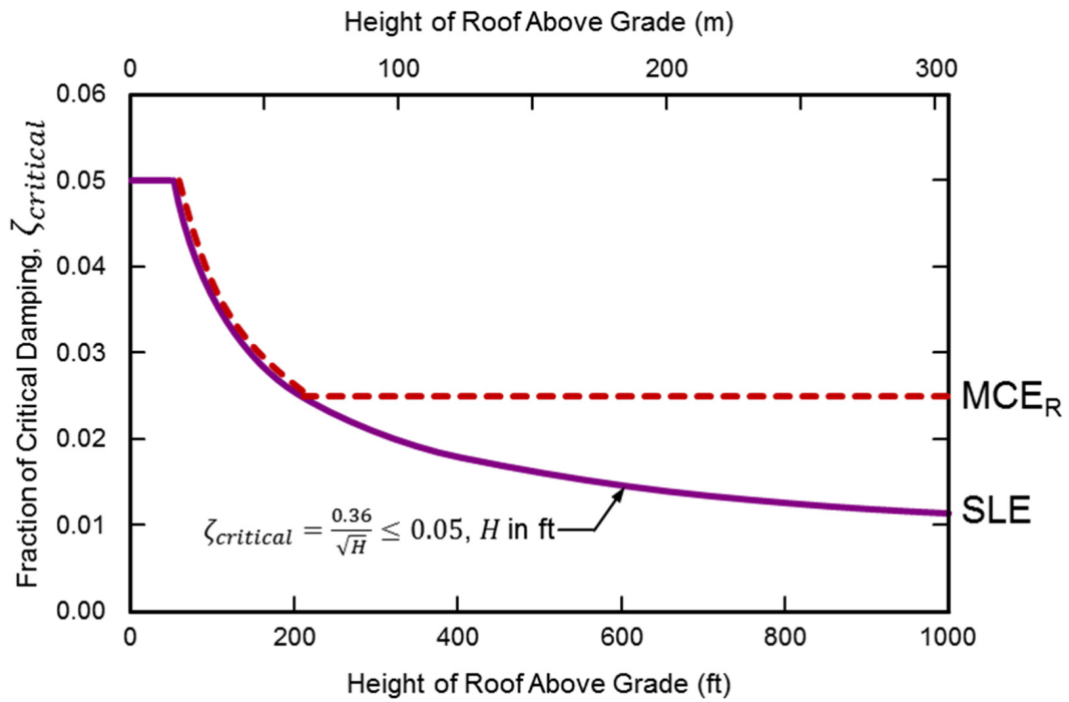


Figure 5.8 Equivalent viscous damping versus building height (TBI Guidelines, 2017)

Both in linear response spectrum analyses and in linear and nonlinear time history analyses, section properties need to be reduced to account for concrete cracking and damage to the components, through section property modifiers with reduced effective stiffness of the member. Property modifiers are based on experimental testing and their values are typically proposed by the building codes and guidelines. For example, accordingly to the “*TBI – Guidelines for Performance-Based Seismic Design of Tall Buildings*”, the reinforced concrete effective stiffness values can be estimated from Table 5.3.

Table 5.3 Reinforced concrete effective stiffness values

Component	Service-Level Linear Models			MCE <sub>R</sub> -Level Nonlinear Models		
	Axial	Flexural	Shear	Axial	Flexural	Shear
Structural walls <sup>1</sup> (in-plane)	$1.0E_cA_g$	$0.75E_cI_g$	$0.4E_cA_g$	$1.0E_cA_g$	$0.35E_cI_g$	$0.2E_cA_g$
Structural walls (out-of-plane)	--	$0.25E_cI_g$	--	--	$0.25E_cI_g$	--
Basement walls (in-plane)	$1.0E_cA_g$	$1.0E_cI_g$	$0.4E_cA_g$	$1.0E_cA_g$	$0.8E_cI_g$	$0.2E_cA_g$
Basement walls (out-of-plane)	--	$0.25E_cI_g$	--	--	$0.25E_cI_g$	--
Coupling beams with conventional or diagonal reinforcement	$1.0E_cA_g$	$0.07\left(\frac{\ell}{h}\right)E_cI_g$ $\leq 0.3E_cI_g$	$0.4E_cA_g$	$1.0E_cA_g$	$0.07\left(\frac{\ell}{h}\right)E_cI_g$ $\leq 0.3E_cI_g$	$0.4E_cA_g$
Composite steel / reinforced concrete coupling beams	$1.0(EA)_{trans}$	$0.07\left(\frac{\ell}{h}\right)(EI)_{trans}$	$1.0E_sA_{sw}$	$1.0(EA)_{trans}$	$0.07\left(\frac{\ell}{h}\right)(EI)_{trans}$	$1.0E_sA_{sw}$
Non-PT transfer diaphragms (in-plane only) <sup>3</sup>	$0.5E_cA_g$	$0.5E_cI_g$	$0.4E_cA_g$	$0.25E_cA_g$	$0.25E_cI_g$	$0.1E_cA_g$
PT transfer diaphragms (in-plane only) <sup>3</sup>	$0.8E_cA_g$	$0.8E_cI_g$	$0.4E_cA_g$	$0.5E_cA_g$	$0.5E_cI_g$	$0.2E_cA_g$
Beams	$1.0E_cA_g$	$0.5E_cI_g$	$0.4E_cA_g$	$1.0E_cA_g$	$0.3E_cI_g$	$0.4E_cA_g$
Columns	$1.0E_cA_g$	$0.7E_cI_g$	$0.4E_cA_g$	$1.0E_cA_g$	$0.7E_cI_g$	$0.4E_cA_g$
Mat (in-plane)	$0.8E_cA_g$	$0.8E_cI_g$	$0.8E_cA_g$	$0.5E_cA_g$	$0.5E_cI_g$	$0.5E_cA_g$
Mat <sup>4</sup> (out-of-plane)	--	$0.8E_cI_g$	--	--	$0.5E_cI_g$	--

<sup>1</sup>Values are relevant where walls are modeled as line elements. Where walls are modeled using fiber elements, the model should automatically account for cracking of concrete and the associated effects on member stiffness.

<sup>2</sup> $(EI)_{trans}$  is intended to represent the flexural rigidity of the cracked transformed section. It is acceptable to calculate the transformed section properties based on structural mechanics or to use  $(EI)_{trans} = E_cI_g/5 + E_sI_s$  per ACI 318.

<sup>3</sup>Specified stiffness values for diaphragms are intended to represent expected values. Alternative values may be suitable where bounding analyses are used to estimate bounds of force transfers at major transfer levels. For diaphragms that are not associated with major force transfers, common practice is to model the diaphragm as being rigid in its plane. Flexural rigidity of diaphragms out of plane is usually relatively low and is commonly ignored. The exception is where the diaphragm acts as a framing element to engage gravity columns as outrigger elements, in which case out-of-plane modeling may be required.

<sup>4</sup>Specified stiffness values for mat foundations pertain to the general condition of the mat. Where the walls or other vertical members impose sufficiently large forces, including local force reversals across stacked wall openings, the stiffness values may need to be reduced.

## 6 NONLINEAR MODELLING OF STRUCTURES

Over last few decades, the structural design against earthquakes has passed through a continuous process of evolution, starting from a simple mass-proportional lateral load applied to the structure and evolving into an explicit consideration of design earthquakes applied to a more detailed nonlinear finite-element model. Initially, for the structural design, the seismic load was idealized as a simple mass-proportional lateral static loading. Later, with the increasing applications of modal analysis and the formulation of the response spectrum analysis (RSA) procedure, the role of vibration modes and natural periods of the structure in understanding and controlling the seismic demand was recognized. With the advent of computer programs and dynamic analysis solvers and with the increasing availability of more ground motion records, the use of detailed dynamic analysis procedures based on the direct integration solution of the governing dynamic equations of motion was established. Nonlinear modelling and analysis of complex structures, such as high-rise reinforced concrete buildings, requires a detailed understanding of inelastic phenomena and also significant computational effort and the use of advanced structural analysis software. For these reasons, the obtained results can be significantly sensitive to nonlinear modelling assumptions and inelastic properties of components assigned to the elements. The advent of the “Performance-based Design” methodology increased the need of nonlinear modelling and analysis for structures, especially in the case of tall buildings, as discussed in the previous chapter.

The nonlinear model of a structure is capable to clearly identify the structural damage and performance in terms of deformation demand-capacity ratios, in addition the structural seismic response is more realistic and meaningful if compared to a linear elastic one. Nonlinear models can generally be classified based on the degree of idealization used in the model. A comparison of three idealized nonlinear model types for a reinforced concrete element is show in Figure 6.1 (Graham H. Powell, 2010).

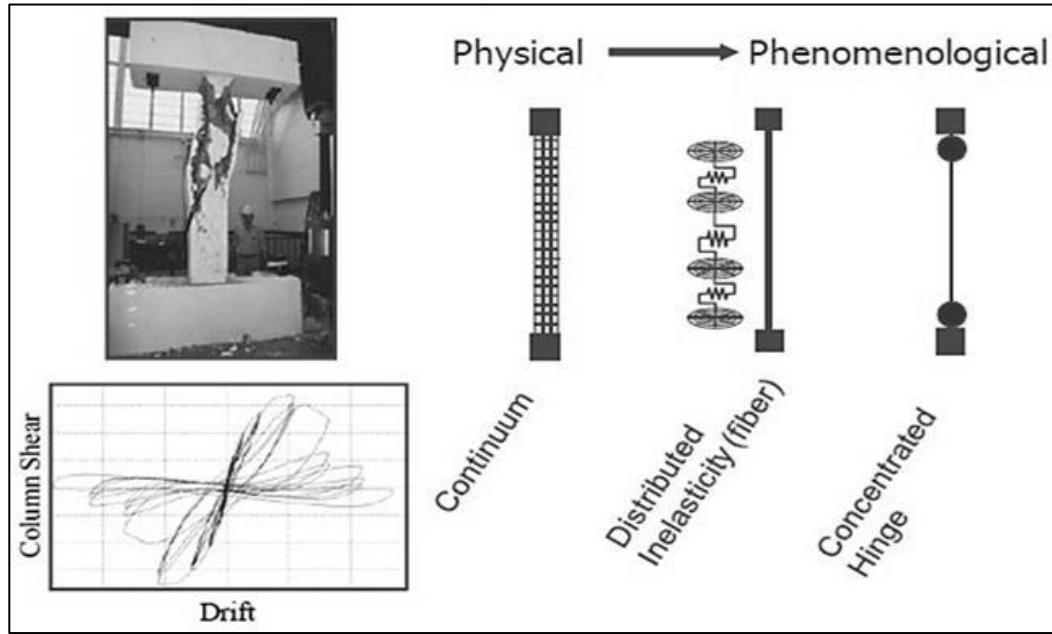


Figure 6.1 Comparison of nonlinear model types for reinforced concrete element

Continuum and distributed inelasticity models can capture in a more accurate way behaviors such as initiation of concrete cracking and steel yielding, but they can have some limits to capture strength degradation, reinforcing bar buckling, bond slip and shear failure. On the other way the concentrated hinge models can capture strength degradation effects, but in a more empirical manner, in contrast to fiber and continuum finite element models that are calibrated more at the material level, where the kinematics and equilibrium of the components are represented directly by the model formulation. Concentrated hinge models are also more consistent with common limit state checks related to stress resultants and concentrated deformations in current building codes. The current practice for nonlinear modelling is mostly based on the use of concentrated and fiber hinge models.

## 6.1 Fiber modelling approach

The fiber modelling approach (Graham H. Powell, 2010) is based on the division of the cross-section of a structural element into a number of uniaxial fibers arranged along the longitudinal axis of the element. A uniaxial stress-strain relationship (as shown in Figure 6.2) is assigned to each fiber of the section and it allows to consider various aspects of material nonlinearity. These fibers may either be used throughout the whole

length of the member or just for a fraction of it. In this second case, the model is assigned to the plastic zone of the member, where is expected the inelastic behavior of the structural element. For reinforced concrete elements, a fiber segment consists of several concrete and steel fibers with their respective stress-strain relationships.

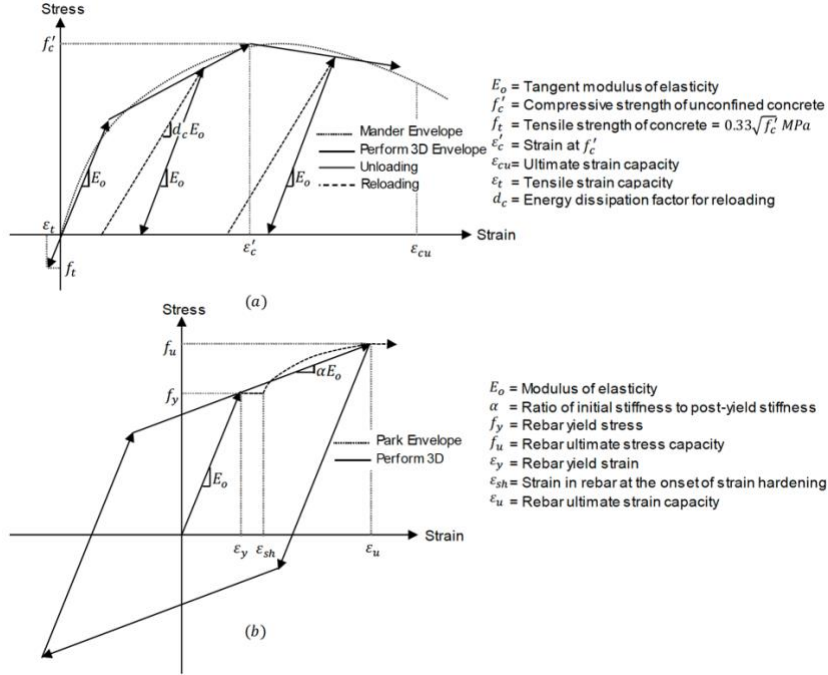


Figure 6.2 Stress-strain curve for concrete (a) and steel (b) for uniaxial fiber model

### 6.1.1 Fiber model for RC beams

Figure 6.3 shows the fiber model approach that can be used for a beam section. A common assumption for beams is that the inelastic behavior can be considered just for vertical bending, while for horizontal bending the behavior is elastic (Graham H. Powell, 2010). In order to model bending behavior in vertical direction, fibers are needed only through the depth of the beam, as shown in Figure 6.3. In this case, the cross section is discretized just in one direction to define the uniaxial concrete and steel fibers. For horizontal bending, the beam is characterized by an elastic bending stiffness defined through its  $EI$  value and the model assumes that there is no interaction between axial load and bending moment and also that there is no coupling between vertical and lateral bending. However, for vertical bending the  $EI$  stiffness is defined by the fiber model.

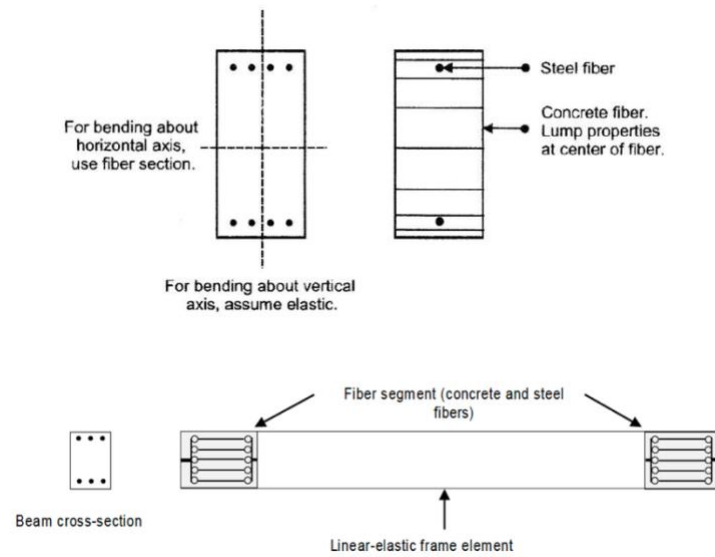


Figure 6.3 Fiber section of a reinforced concrete beam (Powell, 2010, Mazhar H. et al., 2021)

### 6.1.2 Fiber model for RC columns

Figure 6.4 shows the fiber model approach that can be used for a column section. In this case, it is necessary to consider the biaxial bending stress in the cross-section. Hence, fibers are needed in both cross-sectional directions, as illustrated in Figure 6.4.

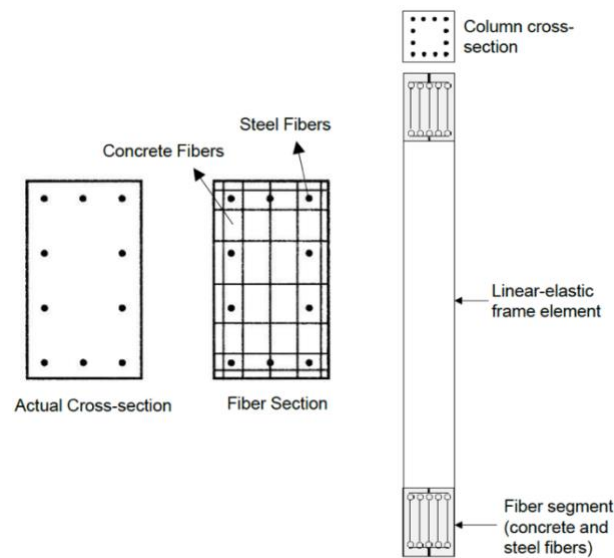


Figure 6.4 Fiber section of a reinforced concrete column ((Powell, 2010, Mazhar H. et al., 2021)



This type of model allows to consider the axial-flexural interaction in both cross-sectional axes. For both beams and columns, the behavior in torsion is usually assumed to be elastic and also uncoupled from the axial and bending behavior (Graham H. Powell, 2010).

### 6.1.3 Fiber model for walls

Shear wall section are characterized by bending in two directions, usually named in-plane and out-of-plane. However, in most cases it is reasonable to consider inelastic behavior only for in-plane bending and to assume an elastic behavior for out-of-plane bending. In this case, the fiber model can be similar to the beam one, as shown in Figure 6.5.

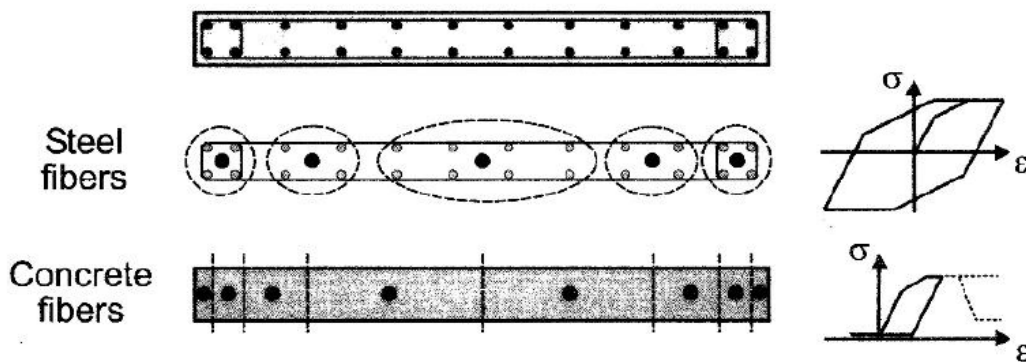


Figure 6.5 Fiber section for in-plane bending behavior of a reinforced concrete wall

### 6.1.4 Limitations of fiber models (Graham H. Powell, 2010)

Fiber models can capture the cracking of reinforced concrete cross sections in the elastic range, P-M-M strength interaction, both axial and bending deformations after yield. However, fiber models can not necessarily predict ductile limits and subsequent strength loss. The major limitations of these models are:

- The ductile limit for a reinforced concrete section may be reached when the concrete crushes and loses strength. In an actual cross-section, crushing starts at the extreme edge of the cross section and progresses continuously into the section. In a fiber model, crushing occurs fiber by fiber and progresses

---

discontinuously into the section according to the fibers yielding. If relatively few fibers are used to model a cross section, the fibers are very large, so crushing starts later in the model than in the actual section, and the crushed part of the cross-section changes in relatively large jumps. For this reason, as more fibers are used the model becomes more accurate, but the computational cost increases.

- The strength of concrete in compression, and also its ductility, depend on the amount of confinement. In a cross section, a part of the concrete is within the confinement and another one is unconfined. This aspect should be taken into account in the definition of the fiber model.
- In a fiber model, the stress-strain relationship for steel fibers can, in principle, account for buckling, but the buckling behavior is uncertain and difficult to model. The same is for bond slip, which is not considered in a basic fiber model and in most of cases the bond slip phenomenon is too complex to be included in a model of a complete structure.
- The strength of a RC element may be controlled by shear, or by P-M-V acting in combinations. However, the basic fiber model considers only P-M interaction because it is much more difficult to model P-M-V interaction.

In conclusion, fiber model can be useful, but is not a complete solution. A fiber model may not be accurate for large cyclic deformations, it does not account for bond slip or shear force effects, and it cannot predict the ductile limit and the amount of strength loss. Fiber models can certainly be better than model based on plasticity theory, but they still have major limitations.

### **6.1.5 Inelastic shear behavior in beams and columns**

In principle it is possible to consider inelastic shear behavior in beams and columns using P-M-V yield surfaces and plasticity theory (Graham H. Powell, 2010). However, in practice it is extremely difficult, especially for cyclic loading and for reinforced concrete. In any case, this is just a theoretical problem because as a general rule, the behavior of reinforced concrete in shear is brittle, with substantial degradation under cyclic deformations. For this reason, the aim is to design reinforced concrete beams

and columns to remain essentially elastic in shear, avoiding the P-M-V inelastic interaction.

## 6.2 Plastic hinge modelling approach

The plastic hinge modelling approach assumes that all inelastic deformation is concentrated in a certain point of the structural element, so the inelastic relationship is directly defined to the member cross-section. In the structural model, the definition of the plastic hinge location is based on the expected damage areas of the elements under the seismic loads. Figure 6.6 shows the plastic hinge model of a 2D reinforced concrete frame subjected to lateral earthquake loading. The yellow circles show the potential locations of inelastic action where the structural damage is expected, so in the model the concentrated plastic hinges are placed in that locations.

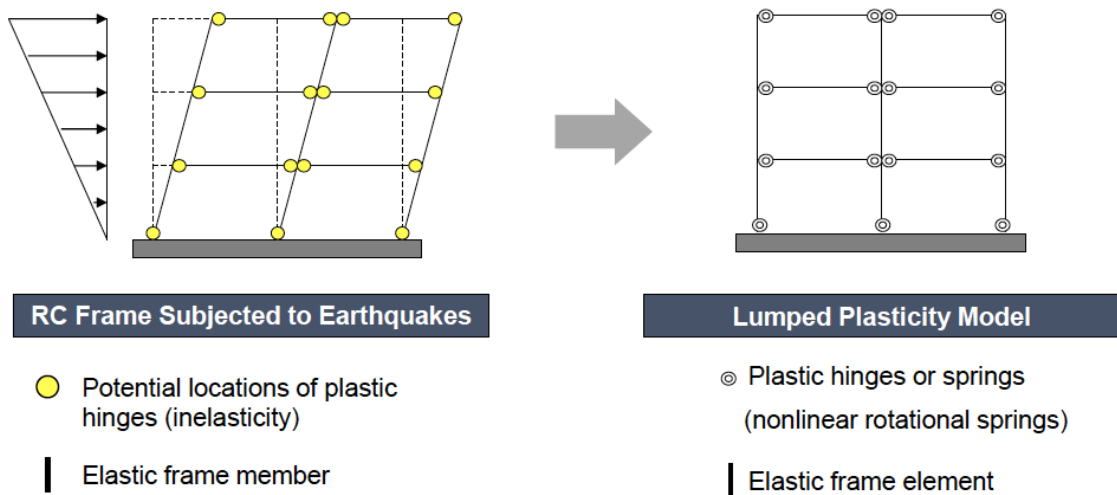


Figure 6.6 Plastic hinge model of a 2D frame subjected to lateral earthquake loading

Thus, in the lumped plasticity model the nonlinearity is assumed to be concentrated only at the plastic hinges, while the frame elements have an elastic behavior.

### 6.2.1 Plastic hinge model for RC beams

The inelastic behavior of beams can be modelled using moment-rotation plastic hinges, as shown in Figure 6.7 (Graham H. Powell, 2010). The reinforced concrete beams are modelled as elastic frame elements with plastic hinges at both ends, thus it

is assumed that all inelastic deformation is concentrated in zero-length plastic hinge, while the rest of the beam remains elastic. The plastic hinge is initially rigid and begins to rotate and participate in structural response at first yield. Therefore, plastic hinges are sometimes defined “rigid”. This means that the initial elastic flexural stiffness of the beam is used in the analysis until the reaching of the yielding point. However, after the yield, the flexural behavior is governed by the nonlinear moment-rotation relationship specified at the plastic hinge location.

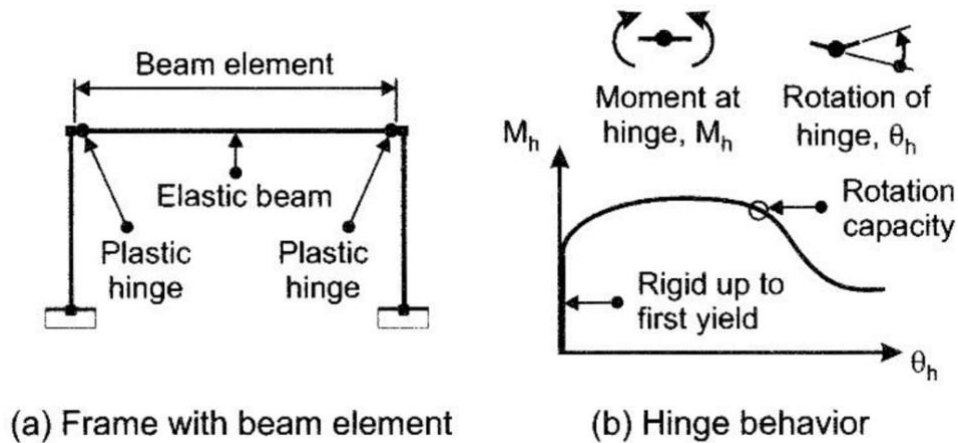


Figure 6.7 Plastic hinge modelling of beams (Powell, 2010)

The primary properties required to define a plastic hinge are its bending strength and the hinge rotation capacity, which is the rotation at the ductile limit. A way to obtain these properties, when the experimental results are not available, is to refer to specialized guidelines, such as ASCE 41, where the modelling parameters are prescribed.

### 6.2.2 Plastic hinge model for RC columns

The inelastic behavior of columns can be modelled using P-M-M plastic hinges. The reinforced concrete columns are modelled as elastic frame elements with plastic hinges to the base and to the end of the clear length of the member, so, as for the beams, it is assumed that all inelastic deformation is concentrated in zero-length plastic hinge, while the rest of the element remains elastic. The most important difference in this case is the interaction between the axial force and the bending moments acting in the

columns, which involves the use of interaction surfaces to define the yield and ultimate strength of the cross section of the element and in general complicates the plastic hinge modelling. For the three-dimensional case, the P-M-M interaction surface is represented by a 3D solid, as shown in Figure 6.8 (Graham H. Powell, 2010).

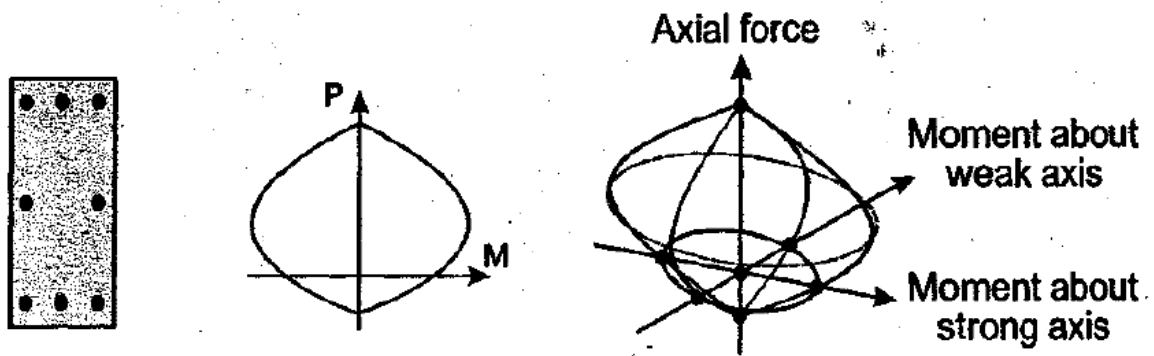


Figure 6.8 Yield surface for reinforced concrete columns (Powell, 2010)

The application of plasticity theory to P-M-M interaction involves many assumptions and approximations, especially in the case of reinforced concrete columns:

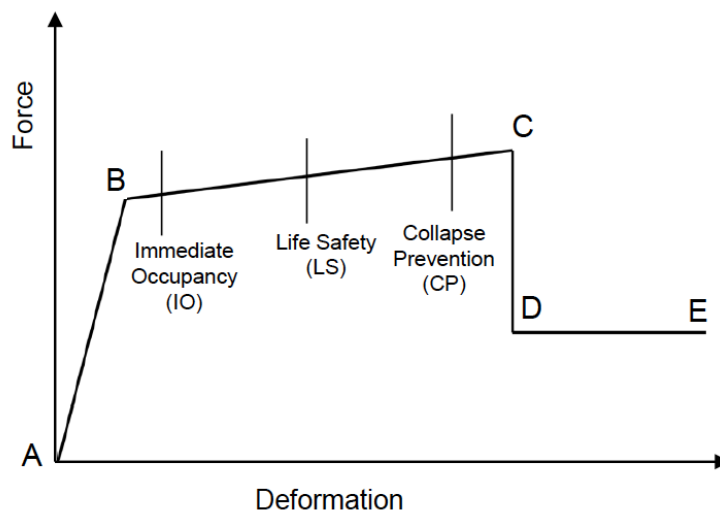
- Even in the elastic range, inside the yield interaction surface, the behavior of a real cross section is more complex than is assumed in plasticity theory, mainly because it is usual to assume constant values for the cross-section stiffness ( $EA$ ,  $EI$ ), even though these values change when the concrete cracks;
- Reinforced concrete is not a plastic material, in particular plasticity theory does not account correctly for the effects of cracking;
- Plasticity theory must usually assume that the yielding and ultimate interaction surfaces have the same shape, and also that the shape does not change as strain hardening occurs. There is also likely to be uncertainty about whether hardening follows the kinematic or isotropic assumption.
- It is difficult to model hysteresis loops accurately when there is interaction, especially when there is stiffness degradation, strength loss and progressive cyclic degradation in strength and ductility.

Despite these limitations for small amounts of hinging in concrete column the plasticity theory is still accurate enough for P-M-M strength interaction and for

inelastic bending. However, if there is substantial hinging, plasticity theory may be in error. In such cases it may be necessary to use a fiber hinge model, as described in the paragraph 6.1.2.

### 6.2.3 Moment-Rotation relationship in ASCE 41-13

Seismic Design Guidelines for Tall Buildings (PEER, 2017) discusses two levels of performance-based seismic assessment: Service level evaluation and Maximum Considered Earthquake (MCE) level evaluation, which generally involve comparisons of force and deformation demands imposed by the specified earthquake hazard to corresponding limit state capacities of the structural components and systems. For the performance-based seismic evaluation of components, several performance levels (Immediate Occupancy, Life Safety and Collapse Prevention) are defined and marked on the nonlinear force-deformation relationships assigned to plastic hinges, as shown in Figure 6.9.



*Figure 6.9 Force vs. Deformation curve for the plastic hinge definition – Acceptance Criteria Illustration*

In the **Immediate Occupancy (IO)** level only a small amount of inelastic behavior is allowed, so the elastic analysis should be sufficient. In the **Life Safety (LS)** level, a larger amount of inelastic behavior is allowed, so it is necessary to use an inelastic model of the structure, that should consider the yield and ultimate strengths of the

---

structural components. The hysteresis loops can be expected to be fairly simple at this level of deformation, with modest degradation in stiffness and strength. In the **Collapse Prevention (CP)** level, the allowed amount of inelastic behavior is even larger than the **LS** level, so in this case it is reasonable to expect more complex hysteresis loops with substantial degradation in stiffness and strength.

Generally, in the plastic hinges modelling, five points labelled A,B,C,D and E are used to define the force-deformation behavior of the plastic hinges, as illustrated in Figure 6.9:

- Point A is always the origin.
- Point B represents yielding. No deformation occurs in the hinge up to point B. The displacement at this point will be subtracted from the deformations at points C, D, E in order to consider only the plastic deformation exhibited by the hinge.
- Point C represents the ultimate capacity for pushover analysis.
- Point D represents a residual strength for pushover analysis.
- Point E represent total failure of the hinge.

Before reaching point B, all deformation is linear and occurs in the frame element and not in the hinge. Plastic deformation beyond point B occurs in the hinge in addition to the elastic deformation that occurs in the frame element. A way to obtain these properties, when the experimental results are not available, is to refer to specialized guidelines, such as ASCE 41, where the modelling parameters are prescribed.

ASCE 41 is a standard for seismic rehabilitation of existing buildings, but it may also be used in the design of new ones. Among many other things, ASCE 41 provides modelling guidelines for inelastic analysis and performance assessment of different structural components.

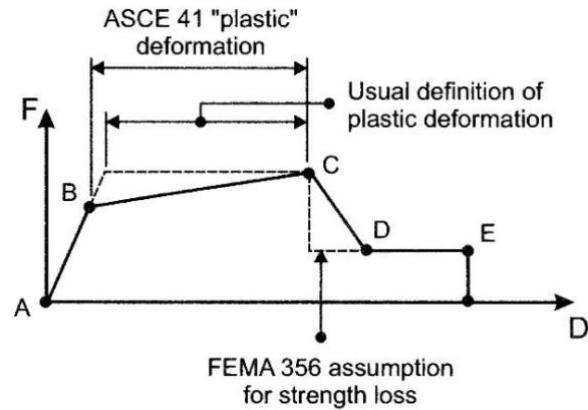


Figure 6.10 ASCE 41 force-deformation relationship

For the plastic hinge modelling, ASCE 41 recommends deformation capacities for a wide range of components, for the Immediate Occupancy (IO), Life Safety (LS) and Collapse Prevention (CP) performance levels. For example, the following tables, taken from the ASCE 41-13 guidelines, defines the modelling parameters and numerical acceptance criteria for reinforced concrete beams and columns.

Table 6.1 Modelling Parameters and Numerical Acceptance Criteria for  
Nonlinear Procedures – Reinforcement Concrete Beams (ASCE41-13)

Conditions			Modelling Parameters <sup>a</sup>			Acceptance Criteria <sup>a</sup>		
			Plastic Rotations Angle (radians)		Residual Strength Ratio	Plastic Rotations Angle (radians)		
			a	b		Performance Level		
					c	IO	LS	CP
Condition i. Beams controlled by flexure <sup>b</sup>								
$\rho - \rho'$	Transverse reinforcement <sup>c</sup>	$\frac{V}{b_w d \sqrt{f'_c}}$ <sup>d</sup>						
$\leq 0.0$	C	$\leq 3$ (0.25)	0.025	0.05	0.2	0.010	0.025	0.05
$\leq 0.0$	C	$\geq 6$ (0.5)	0.02	0.04	0.2	0.005	0.02	0.04
$\geq 0.5$	C	$\leq 3$ (0.25)	0.02	0.03	0.2	0.005	0.02	0.03
$\geq 0.5$	C	$\geq 6$ (0.5)	0.015	0.02	0.2	0.005	0.015	0.02
$\leq 0.0$	NC	$\leq 3$ (0.25)	0.02	0.03	0.2	0.005	0.02	0.03
$\leq 0.0$	NC	$\geq 6$ (0.5)	0.01	0.015	0.2	0.0015	0.01	0.015
$\geq 0.5$	NC	$\leq 3$ (0.25)	0.01	0.015	0.2	0.005	0.01	0.015
$\geq 0.5$	NC	$\geq 6$ (0.5)	0.005	0.01	0.2	0.0015	0.005	0.01
Condition ii. Beams controlled by shear <sup>b</sup>								
Stirrup spacing $\leq d/2$			0.0030	0.02	0.2	0.0015	0.01	0.02
Stirrup spacing $> d/2$			0.0030	0.01	0.2	0.0015	0.005	0.01
Condition iii. Beams controlled by inadequate development or splicing along the span <sup>b</sup>								
Stirrup spacing $\leq d/2$			0.0030	0.02	0.0	0.0015	0.01	0.02
Stirrup spacing $> d/2$			0.0030	0.01	0.0	0.0015	0.005	0.01
Condition iv. Beams controlled by inadequate embedment into beam-column joint <sup>b</sup>								
			0.015	0.03	0.2	0.01	0.02	0.03

NOTE:  $f'_c$  in lb/in.<sup>2</sup> (MPa) units.

<sup>a</sup>Values between those listed in the table should be determined by linear interpolation.

<sup>b</sup>Where more than one of conditions i, ii, iii, and iv occur for a given component, use the minimum appropriate numerical value from the table.

<sup>c</sup>"C" and "NC" are abbreviations for conforming and nonconforming transverse reinforcement, respectively. Transverse reinforcement is conforming if, within the flexural plastic hinge region, hoops are spaced at  $\leq d/3$ , and if, for components of moderate and high ductility demand, the strength provided by the hoops ( $V_h$ ) is at least 3/4 of the design shear. Otherwise, the transverse reinforcement is considered nonconforming.

<sup>d</sup> $V$  is the design shear force from NSP or NDP.



*Table 6.2 Modelling Parameters and Numerical Acceptance Criteria for  
Nonlinear Procedures – Reinforcement Concrete Columns (ASCE 41-13)*

Conditions			Modeling Parameters <sup>a</sup>			Acceptance Criteria <sup>a</sup>		
			Plastic Rotations Angle (radians)		Residual Strength Ratio	Plastic Rotations Angle (radians)		
			a	b		Performance Level		
					c	IO	LS	CP
Condition i. <sup>b</sup>								
$\frac{P}{A_g f'_c}$	$\rho = \frac{A_s}{b_w s}$							
$\leq 0.1$	$\geq 0.006$		0.035	0.060	0.2	0.005	0.045	0.060
$\geq 0.6$	$\geq 0.006$		0.010	0.010	0.0	0.003	0.009	0.010
$\leq 0.1$	$\leq 0.002$		0.027	0.034	0.2	0.005	0.027	0.034
$\geq 0.6$	$\leq 0.002$		0.005	0.005	0.0	0.002	0.004	0.005
Condition ii. <sup>b</sup>								
$\frac{P}{A_g f'_c}$	$\rho = \frac{A_s}{b_w s}$	$\frac{V}{b_w d \sqrt{f'_c}}$						
$\leq 0.1$	$\geq 0.006$	$\leq 3 (0.25)$	0.032	0.060	0.2	0.005	0.045	0.060
$\leq 0.1$	$\geq 0.006$	$\geq 6 (0.5)$	0.025	0.060	0.2	0.005	0.045	0.060
$\geq 0.6$	$\geq 0.006$	$\leq 3 (0.25)$	0.010	0.010	0.0	0.003	0.009	0.010
$\geq 0.6$	$\geq 0.006$	$\geq 6 (0.5)$	0.008	0.008	0.0	0.003	0.007	0.008
$\leq 0.1$	$\leq 0.0005$	$\leq 3 (0.25)$	0.012	0.012	0.2	0.005	0.010	0.012
$\leq 0.1$	$\leq 0.0005$	$\geq 6 (0.5)$	0.006	0.006	0.2	0.004	0.005	0.006
$\geq 0.6$	$\leq 0.0005$	$\leq 3 (0.25)$	0.004	0.004	0.0	0.002	0.003	0.004
$\geq 0.6$	$\leq 0.0005$	$\geq 6 (0.5)$	0.0	0.0	0.0	0.0	0.0	0.0
Condition iii. <sup>b</sup>								
$\frac{P}{A_g f'_c}$	$\rho = \frac{A_s}{b_w s}$							
$\leq 0.1$	$\geq 0.006$		0.0	0.060	0.0	0.0	0.045	0.060
$\geq 0.6$	$\geq 0.006$		0.0	0.008	0.0	0.0	0.007	0.008
$\leq 0.1$	$\leq 0.0005$		0.0	0.006	0.0	0.0	0.005	0.006
$\geq 0.6$	$\leq 0.0005$		0.0	0.0	0.0	0.0	0.0	0.0
Condition iv. Columns controlled by inadequate development or splicing along the clear height <sup>c</sup>								
$\frac{P}{A_g f'_c}$	$\rho = \frac{A_s}{b_w s}$							
$\leq 0.1$	$\geq 0.006$		0.0	0.060	0.4	0.0	0.045	0.060
$\geq 0.6$	$\geq 0.006$		0.0	0.008	0.4	0.0	0.007	0.008
$\leq 0.1$	$\leq 0.0005$		0.0	0.006	0.2	0.0	0.005	0.006
$\geq 0.6$	$\leq 0.0005$		0.0	0.0	0.0	0.0	0.0	0.0

NOTE:  $f'_c$  is in lb/in.<sup>2</sup> (MPa) units.

<sup>a</sup>Values between those listed in the table should be determined by linear interpolation.

<sup>b</sup>Refer to Section 10.4.2.2.2 for definition of conditions i, ii, and iii. Columns are considered to be controlled by inadequate development or splices where the calculated steel stress at the splice exceeds the steel stress specified by Eq. (10-2). Where more than one of conditions i, ii, iii, and iv occurs for a given component, use the minimum appropriate numerical value from the table.

<sup>c</sup>Where  $P > 0.7A_g f'_c$ , the plastic rotation angles should be taken as zero for all performance levels unless the column has transverse reinforcement consisting of hoops with 135-degree hooks spaced at  $\leq d/3$  and the strength provided by the hoops ( $V_h$ ) is at least 3/4 of the design shear. Axial load  $P$  should be based on the maximum expected axial loads caused by gravity and earthquake loads.

<sup>d</sup> $V$  is the design shear force from NSP or NDP.

### 6.3 Nonlinear time-history analysis

Time-history analysis is a step-by-step analysis of the dynamical response of a structure to a specified loading that may vary with time (CSi Reference Manual., 2017). The analysis may be linear or nonlinear. This paragraph describes the mainly concepts of the nonlinear time-history analysis, which is used for the case study described in the chapter 7 of this thesis. The dynamic equilibrium equations to be solved are given by:

---


$$\mathbf{K} \mathbf{u}(t) + \mathbf{C} \dot{\mathbf{u}}(t) + \mathbf{M} \ddot{\mathbf{u}}(t) = \mathbf{r}(t) \quad (6.1)$$

where  $\mathbf{K}$  is the stiffness matrix,  $\mathbf{C}$  is the damping matrix and  $\mathbf{M}$  is the mass matrix;  $\mathbf{u}$ ,  $\dot{\mathbf{u}}$ ,  $\ddot{\mathbf{u}}$  are the displacements, velocities and accelerations of the structure, while  $\mathbf{r}$  is the vector of the applied loads on the structure. If the load consists in ground acceleration, as in this case, then the results in terms of displacements, velocities and accelerations are relative to the ground. The load  $\mathbf{r}(t)$  applied in a time-history case can be written as a finite sum of spatial load vectors  $\mathbf{p}_i$  multiplied by time functions  $f_i(t)$  as shown in the following expression:

$$\mathbf{r}(t) = \sum_i f_i(t) \mathbf{p}_i \quad (6.2)$$

In the case of a nonlinear analysis, the stiffness, damping and load may all depend upon the displacements, velocities and time. For this reason, nonlinear analysis requires an iterative solution to the equations of motion.

### 6.3.1 Proportional damping

In direct-integration time history analysis, the damping in the structure is modelled using a full damping matrix, as described in the eq. (6.1). In this case the damping matrix could be calculated, following the *Rayleigh damping method* (Figure 6.11), as a linear combination of the stiffness matrix  $\mathbf{K}$ , scaled by a coefficient  $c_K$ , and the mass matrix  $\mathbf{M}$ , scaled by a second coefficient  $c_M$ , as shown in the following expression:

$$\mathbf{C} = c_M \cdot \mathbf{M} + c_K \cdot \mathbf{K} \quad (6.3)$$

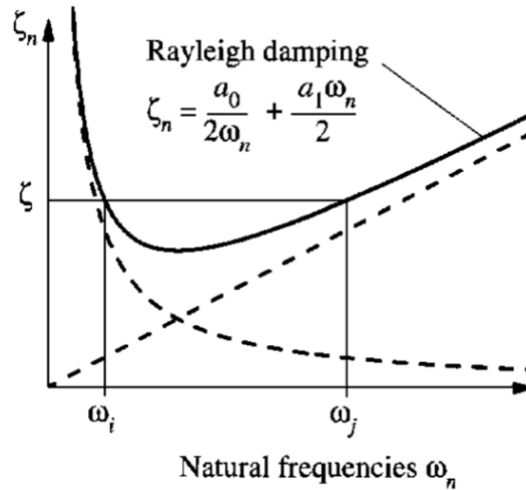


Figure 6.11 Rayleigh damping

The two coefficients  $c_M$  and  $c_K$  can be computed by setting a same modal damping ratio (i.e.,  $\xi_i = 5\%$ ) at two different natural periods (or frequencies) of the structure, that usually correspond to the first modal period and the period required to achieve 90% mass participation in all the directions.

### 6.3.2 Time integration parameters

Direct-integration time-history analysis results are extremely sensitive to time-step size, so it is important to run direct-integration analyses with decreasing time-step sizes until the step size is small enough that the results are no longer affected by it.

A variety of common methods are available for performing direct-integration time-history analysis, but is commonly recommended to use the “Hilber-Hughes-Taylor alpha” (HHT) method. This method uses a single parameter called alpha that may take values between 0 and  $-1/3$ . For  $\alpha = 0$ , the method is equivalent to the Newmark one with  $\gamma = 0.5$  and  $\beta = 0.25$ , which is the same as the average acceleration method, which is also called the trapezoidal rule.

#### 6.3.2.1 Newmark method

In 1959, N. M. Newmark developed a family of time stepping methods based on the following equations (Anil K. Chopra, 1995):

$$\dot{u}_{i+1} = \dot{u}_i + [(1 - \gamma) \Delta t] \ddot{u}_i + (\gamma \Delta t) \ddot{u}_{i+1} \quad (6.4)$$

$$u_{i+1} = u_i + (\Delta t) \dot{u}_i + [(0.5 - \beta) (\Delta t)^2] \ddot{u}_i + [\beta (\Delta t)^2] \ddot{u}_{i+1} \quad (6.5)$$

The parameters  $\beta$  and  $\gamma$  define the variation of acceleration over a time step and determine the stability and accuracy characteristics of the method. Typical selection for  $\gamma$  is  $1/2$  and  $1/6 \leq \beta \leq 1/4$  is satisfactory from all points of view, including that of accuracy. These two equations, combined with the equilibrium equation at the end of the time step, provide the basis for computing  $u_{i+1}$ ,  $\dot{u}_{i+1}$ , and  $\ddot{u}_{i+1}$  at time  $i+1$  from the known  $u_i$ ,  $\dot{u}_i$  and  $\ddot{u}_i$  at time  $i$ . Iteration is required to implement these computations because the unknown  $\ddot{u}_{i+1}$  appears in the right sign of the equations (6.4) and (6.5). However, for linear systems it is possible to modify Newmark's original formulation to obtain solution of the equations (6.4) and (6.5) without iteration. One of the most well-known cases of Newmark's method is the average acceleration one, that is obtained assuming  $\gamma = 1/2$  and  $\beta = 1/4$ . The basic equations of this particular method are shown in Figure 6.12.

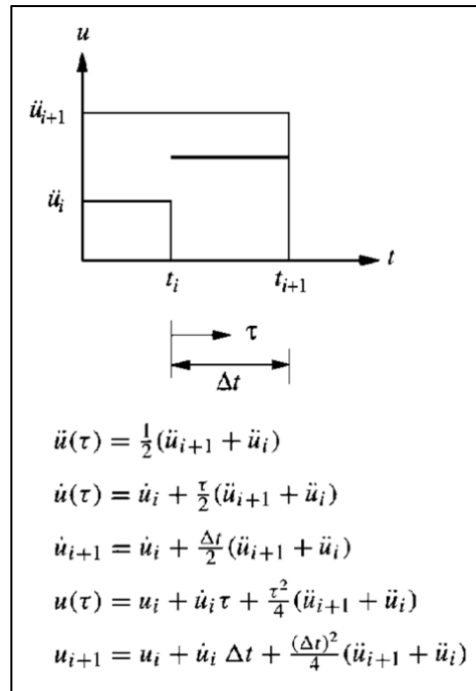


Figure 6.12 Average acceleration method - Newmark's method equations

### 6.3.3 Geometric nonlinearity

Nonlinear time history analysis of the structure should be carried out considering not only the material nonlinearity, as discussed in the previous paragraphs, but also the geometric nonlinearity. Generally, it is possible to choose between two types of geometric nonlinearity: P- $\Delta$  and large displacements. In the P- $\Delta$  analysis, the equilibrium equations take into partial account the deformed configuration of the structure and the solutions may require a moderate amount of iteration. In the large displacements analysis, all equilibrium equations are written in the deformed configuration of the structure and this may require a large amount of iteration, usually using Newton-Raphson method. In most cases the P- $\Delta$  option is sufficient to adequately consider the geometric nonlinearity of the structure, especially in the case of RC frames and when material nonlinearity dominates (Fenwick R.C. et al., 1992).

#### 6.3.3.1 P- $\Delta$ effect

The basic concepts behind the P- $\Delta$  effect are illustrated in the following example (Figure 6.13), where is considered a cantilever beam subjected to an axial load  $P$  and a transverse load  $F$ .

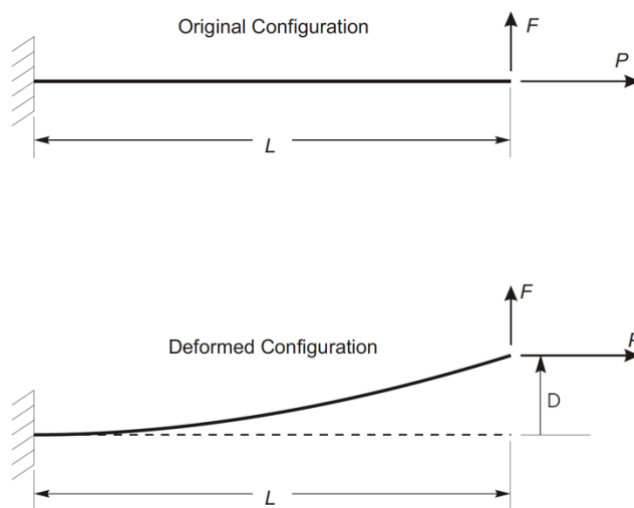
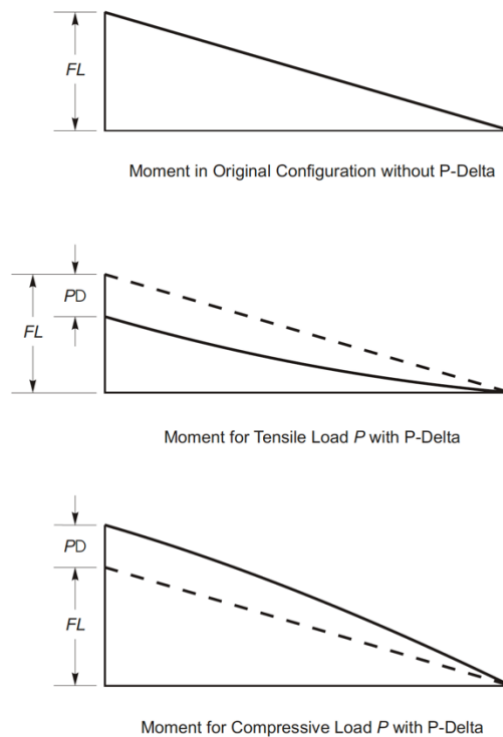


Figure 6.13 Static scheme of the cantilever beam (CSi Reference Manual., 2017)

If equilibrium is examined in the original configuration, considering the undeformed geometry of the beam, the moment at the base is equal to  $M=FL$  and decreases linearly to zero at the loaded end. If, instead, equilibrium is considered in the deformed configuration, there is an additional moment caused by the axial force  $P$  acting on the transverse tip displacement  $\Delta$ . In this second case, the moment at the base is  $M=FL \pm P\Delta$ , where the sign is positive for compressive axial load  $P$  and is negative for tensile axial load  $P$ . The moment diagrams for all the cases described are shown in Figure 6.14.



*Figure 6.14 Moment diagrams for cantilever beam with and without P- $\Delta$  effect  
(CSi Reference Manual., 2017)*

It is important to highlight that only the transverse deflection is considered in the deformed configuration. Any change in moment due to a change in length of the member is neglected in the traditional P- $\Delta$  approach. If the beam is in tension, the moment at the base and throughout the member is reduced, if compared to the one in the original configuration without P- $\Delta$  effect, thus the member is effectively stiffer against the transverse load  $F$ . Conversely, if the beam is in compression, the moment

throughout the member is increased, so the member is more flexible against the transverse load  $F$ .

Similarly, some others basic mechanics related to  $P$ - $\Delta$  actions are illustrated in Figure 6.15 for a single degree of freedom structure that consists of a mass,  $m$ , with weight force,  $P$ , supported by a rigid column with a flexural spring at its base (Fenwick R.C. et al., 1992). A dashpot is attached to the mass to include viscous damping. The stiffness related to the lateral displacement of the mass, due to a horizontal force,  $V$ , is  $K_0$  if  $P$ - $\Delta$  actions are neglected.

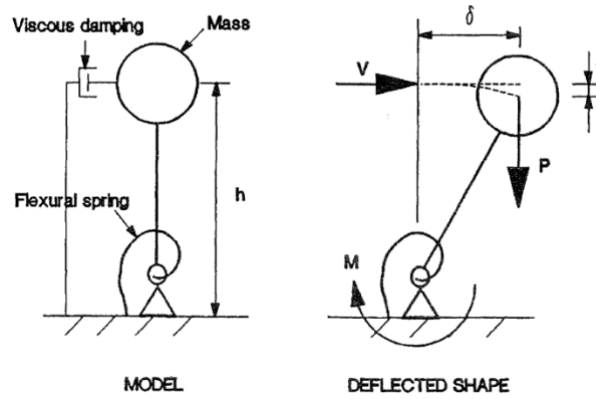


Figure 6.15 Single degree of freedom model (Fenwick R.C. et al., 1992)

With this model the bending moment,  $M$ , acting on the flexural spring is equal to:

$$M = Vh + P\delta \quad (6.6)$$

A measure that is commonly used to assess the sensitivity of structures to  $P$ - $\Delta$  effects is the stability coefficient  $\theta$ , which is a numerical value defined as the ratio of  $P$ - $\Delta$  induced bending moment at some critical section to the corresponding value induced by the lateral load. The coefficient is obtained assuming that the structure is linearly elastic and for a single degree of freedom its value is given by the following equation:

$$\theta = \frac{P\delta}{Vh} \quad (6.7)$$

The influence of P-Δ actions on a single degree of freedom structure with a bilinear hysteretic response is illustrated in Figure 6.16 for the case of monotonically increasing displacement.

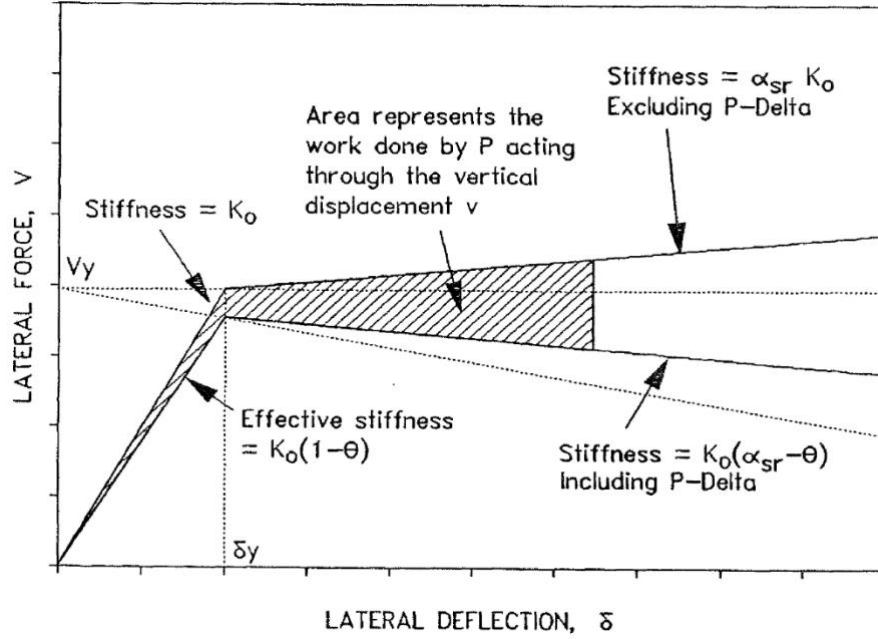


Figure 6.16 P-Δ effects in a structure subjected to monotonically increasing lateral displacement (Fenwick R.C. et al., 1992)

If the P-Δ actions are excluded, a lateral force  $V_y$  is sustained at yield and the subsequent strain hardening stiffness is equal to  $\alpha_{sr} K_0$ . With the P-Δ actions included, the effective lateral stiffness is reduced to  $K_0(1-\theta)$  in elastic range and to  $K_0(\alpha_{sr} - \theta)$  for deflections in the post elastic range. The area between the lateral force versus displacement traces with and without P- Δ actions included represents the work done by the weight force acting through the vertical displacement of the mass.

A consequence of the reduction in stiffness that occurs when P-Δ actions are considered in an analysis is that the period of vibrations increases from  $T$  to  $T'$  (Fenwick R.C. et al., 1992).

$$T' = \frac{T}{\sqrt{1-\theta}} \quad (6.8)$$



---

For  $\theta$  values between 0 e 0.2, the increase in period of vibration is not generally significant in design terms, while for values between 0.2 e 0.3, where 0.3 is considered as the maximum allowable value for structures, is necessary to consider the P- $\Delta$  effects. However, the reduction in stiffness of a structure in the elastic and inelastic range due to the inclusion of P- $\Delta$  effects means that in general there is a tendency for the displacement to increase.

## **7 CASE STUDY: BAIA PROJECT**

This chapter describes the main results obtained for the case study considered in this thesis, which concerns a new building located in the city of Acapulco (Mexico) and whose design is developed in collaboration with another engineering company. The aim of the study is twofold: firstly, it is intended to highlight the benefits associated with the application of the Shear Link Bozzo devices to the structure and the advantages of using the Performance Based Seismic Design Approach instead prescriptive building codes. Therefore, as a first step, the design of the entire structure is carried out proposing the addition of SLB devices. On the other hand, as a second step, a simulated design of the initial bare frame structure, hence without SLB devices, is carried out with the aim of comparing the pros and cons of the two proposed solutions. The analyses are carried out using the software ETABS.

### **7.1 Description of the building**

The case study concerns a new reinforced concrete structure located in the city of Acapulco (Mexico). Baia is a 25-story residential building (see Figure 7.1) with a total height of approximately 86 meters, 79.1 meters of which are above ground. The plan of the building (see Figure 7.2) is, to a good approximation, rectangular in shape and with a total area 312 square meters for story 1 and 453 square meters for others.

The cross-sections of beams and columns and the mechanical properties of the materials, which have been previously defined by the other engineering company, are shown in Table 7.1.

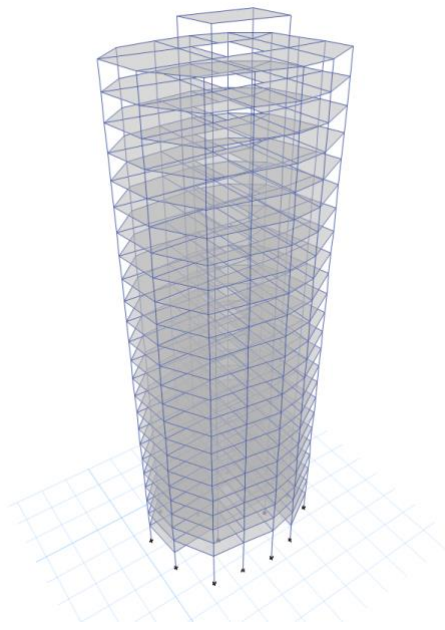


Figure 7.1 Bare frame 3D model

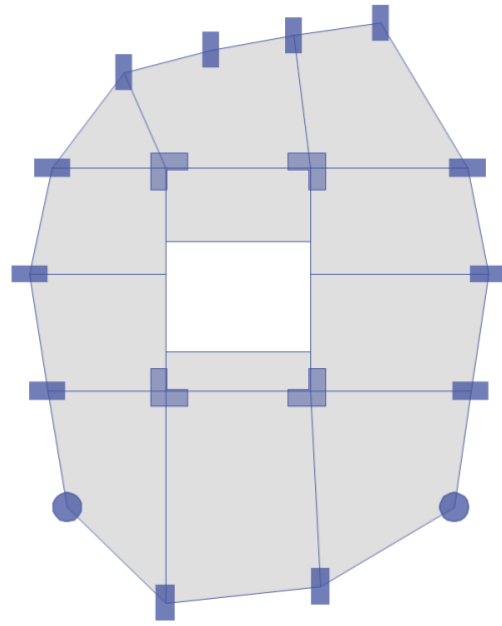


Figure 7.2 Plan of the building

Table 7.1 Geometric and mechanical properties of RC sections for Baia Project

Rect. Section [-]	b [cm]	h [cm]	A <sub>c</sub> [cm <sup>2</sup> ]	Concrete [-]	f <sub>ck</sub> [MPa]
TR 50X110	50	110	5500	C45	45
TR 55X70	55	70	3850	C45	45
TR 40X100	40	100	4000	C45	45
COL 70X125	70	125	8750	C55	55
COL 70X150	70	150	10500	C55	55
COL 80X175	80	175	14000	C55	55
COL 90X100	90	100	9000	C55	55
COL 90X125	90	125	11250	C55	55
COL 90X150	90	150	13500	C55	55
COL 90X175	90	175	15750	C55	55
L-shape Section [-]	b [cm]	B [cm]	A <sub>c</sub> [cm <sup>2</sup> ]	Concrete [-]	f <sub>ck</sub> [MPa]
COL L 70X150	70	150	16100	C45	45
COL L 70X180	70	180	20300	C55	55
COL L 80X180	80	180	22400	C55	55
Circular Section [-]	D [cm]		A <sub>c</sub> [cm <sup>2</sup> ]	Concrete [-]	f <sub>ck</sub> [MPa]
COL 100	100		7854	C45	45
COL 120	120		11310	C55	55
COL 140	140		15394	C55	55

---

The first objective is to optimize the design of the structure through the addition of SLB devices, which are connected to the structure with decoupled concrete walls. As will be shown in the next paragraphs, the use of dissipators increases the stiffness of the structure, reducing the interstory drift at both Service Level Earthquake (SLE) and Maximum Considered Earthquake (MCE) and providing an additional source of dissipation, which leads to a reduction of structural damage in the other structural elements (e.g., beams and columns) and non-structural components.

## 7.2 Reference code

The following reference codes are considered for this case study:

- TBI – Guidelines for Performance Based Seismic Design of Tall Buildings, 2017 – Guidelines developed by the Pacific Earthquake Engineering Research Center (PEER), used to verify the structure through static and dynamic earthquake analyses, to define the site spectra for the MCE level and the selection of ground motions used in the nonlinear time history analyses, to define the effective stiffness of reinforce concrete elements;
- MOC-CFE (2015) – Mexican building code for the design and verification of the structure for seismic loads, used to define the DE and SLE levels site spectra;
- ASCE 41-13 – Reference code used for the modelling parameters and numerical acceptance criteria of reinforcement concrete elements (e.g., beams and columns)
- ACI 318-19 – Building code used for the structural design and check of reinforcement concrete elements.

### 7.2.1 Code requirements

For the Service Level Earthquake (SLE), according to the *PBSD* approach, it is possible to verify the structure with a linear response spectrum analysis, or with linear or nonlinear time history analyses. For global acceptance criteria, according to the

MOC-CFE requirements, the calculated story drift shall not exceed  $0.4\%^1$  of story height in any story. Regarding the component acceptance criteria, if the structure is analyzed with response spectrum or linear response history analysis, calculated demand-to-capacity ratios shall not exceed 1.5 for deformation-controlled actions and 1.0 for force-controlled actions. In case the structure is analyzed with nonlinear time history analysis, calculated deformations in structural elements (e.g., beams, columns) and in the dissipators should not exceed the Immediate Occupancy (IO) level. The fulfilment of these requirements ensures that for the SLE evaluation the structure does not exhibit significant damages to both structural and non-structural elements, thus containing eventual repair costs.

Maximum Considered Earthquake (MCE) evaluation is conducted by means of nonlinear time history analyses according to the requirements of MOC-CFE code and TBI-Guidelines. For the global acceptance evaluation unacceptable response to ground motion consists of any of the following:

- Analytical solution fails to converge;
- Demands on deformation-controlled elements exceed the valid range of modelling;
- Demands on critical or ordinary force-controlled elements exceed the element capacity;
- Deformation demands on elements not explicitly modelled exceed the deformation limits at which the members are no longer able to carry their gravity loads;
- Peak transient story drift ratio in any story exceeds 0.045;
- Residual story drift ratio in any story exceeds 0.015.

For Risk Category II buildings, to which the structure under study belongs, it is permitted to have one unacceptable response. For global acceptance criteria evaluation, in each story, the mean of the values of the peak transient story drift ratios from the seismic signals set should not exceed 0.03, in accordance to both MOC-CFE and TBI-Guidelines. In addition, for the TBI-Guidelines, in each story, the mean of the absolute values of residual drift ratios shall not exceed 0.01. This value is intended

---

<sup>1</sup> The limit value imposed by the MOC-CFE is lower than the one proposed by the TBI-Guidelines (2017) equal to 0.5%

to protect against excessive post-earthquakes, in order to provide enhanced performance for tall buildings.

For the component acceptance criteria evaluation, when the structure is verified with nonlinear time history analyses, calculated deformations in structural elements (e.g., beams, columns) and in the dissipators should not exceed the Collapse Prevention (CP) level.

### 7.3 Load combinations

For the structural design of the building, the following load combinations have been considered:

- $1.4 G_1 + 1.4 G_2$
- $1.2 G_1 + 1.2 G_2 + 1.6 L$
- $1.2 G_1 + 1.2 G_2 + L + W$
- $G_1 + G_2 + 0.5 L \pm E_x \pm 0.3 E_y$
- $G_1 + G_2 + 0.5 L \pm 0.3 E_x \pm E_y$
- $G_1 + G_2 + 0.5 L + TH$

where  $G_1$  and  $G_2$  represent the permanent structural loads and the permanent non-structural loads, respectively;  $L$  indicates the live load,  $W$  the wind load,  $E$  represents the equivalent static seismic load (Response seismic analysis, *RSA*),  $TH$  corresponds to the time history considered in the case of linear or nonlinear time history analysis. The first three load combinations are related to the ultimate limit state assessments of the structure, while the other ones are related to the seismic evaluation of the building at Service Level Earthquake and Maximum Considered Earthquake.

#### 7.3.1 Gravity loads

The permanent structural loads  $G_1$  have been computed automatically by ETABS, while the values considered for the permanent non-structural loads  $G_2$  and live loads  $L$  are  $200 \text{ kgf/m}^2$  and  $190 \text{ kgf/m}^2$ , respectively. The wind load has been computed from the previous engineering company.

---

### 7.3.2 Seismic loads

The seismic design of structures, as explained in the chapter 5 of this thesis, should always include proper evaluation of seismic hazards. PBSD guidelines recommend to establish appropriate site-specific ground motions, rather than using a prescriptive code spectrum, considering all the significant earthquake intensities for the structure. For this case study, the analyses are carried out using site spectra obtained from appropriate ground response analysis. It is important to highlight, as described in section 5.4.1, that in the PBSD approach at least two levels of spectral values should be considered:

- $MCE_R$  is defined as a Risk-Targeted PSHA level of shaking having a 2 percent probability of exceedance in 50 years, that corresponds to a 2475-year return period).
- $SLE$  is defined as a PSHA level having a 50 percent probability of exceedance in 30 years, that corresponds to a 43-year return period.

The procedure for the evaluation of these spectra is explained in the section 7.3.2.1.

#### 7.3.2.1 Site response spectra

This section presents the procedure to calculate response spectra for the building site, which is located in Playa Diamante, Acapulco, Mexico and that is shown in Figure 7.3.

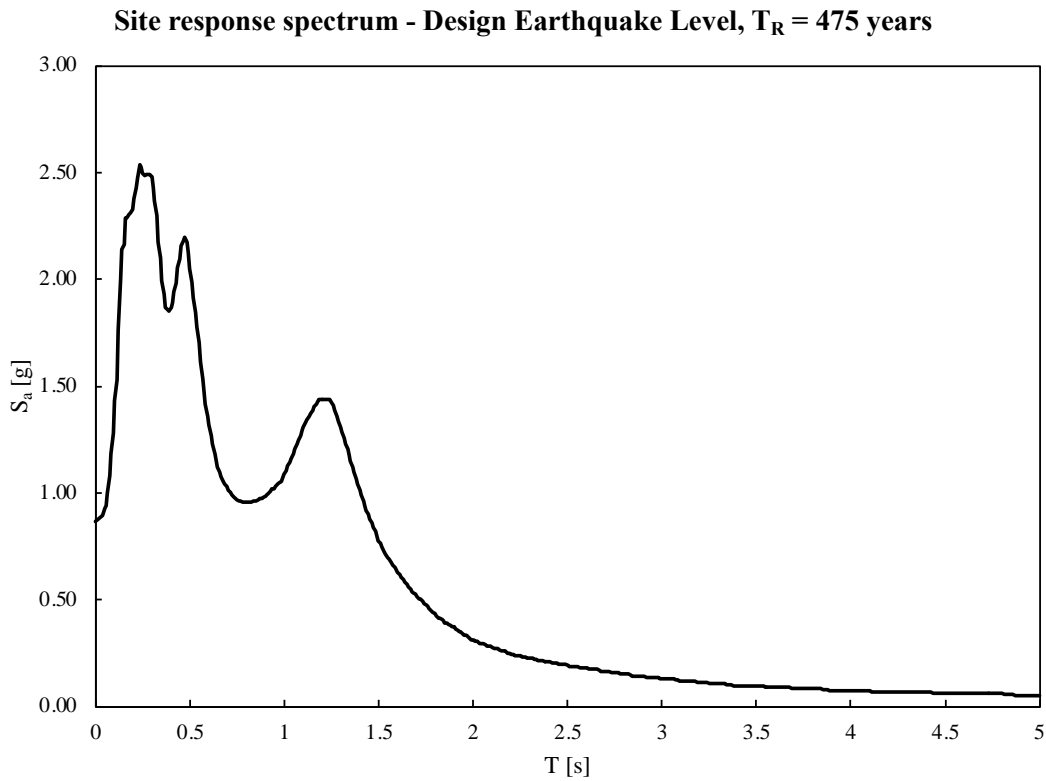


*Figure 7.3 Location of the study site in relation to the seismic regionalization of Mexico (MOC-CFE, 2015)*

In accordance with the seismic regionalization proposed by the “Manual de Obras Civiles de la Comisión Federal de Electricidad”, 2015 (MOC-CFE, 2015), the site under investigation is located in zone D as shown in Figure 7.3.

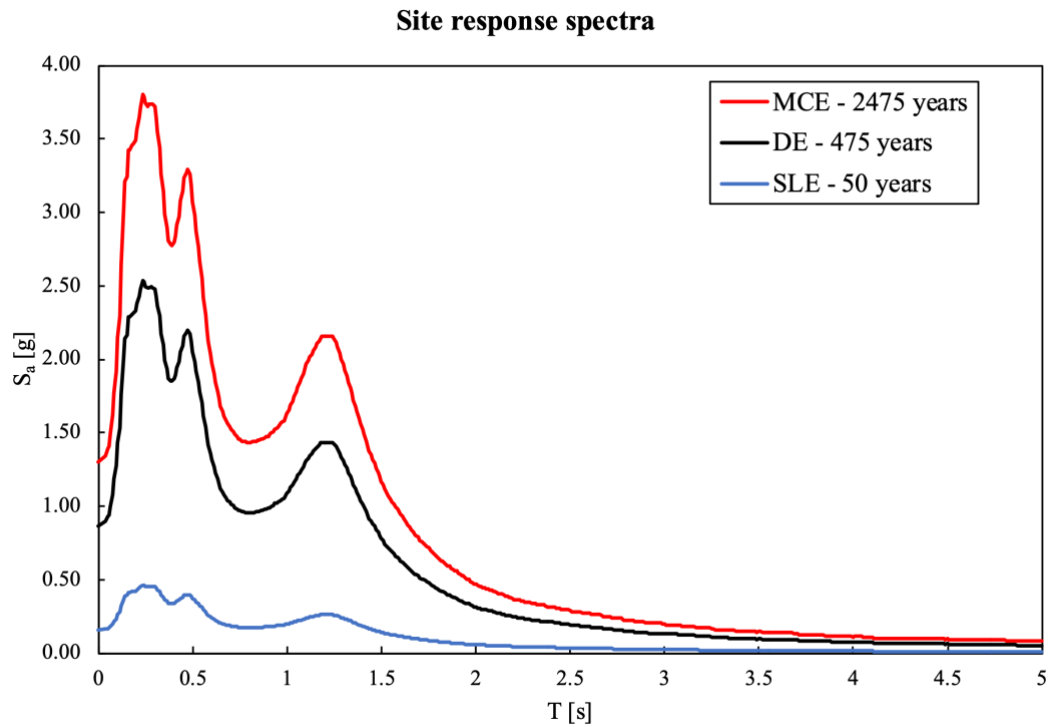
The free-field acceleration site response spectrum, that is shown in Figure 7.4, is obtained from the corresponding bedrock site response spectrum by taking the geotechnical site effects into account.





*Figure 7.4 Site response spectrum - Design Earthquake Level*

The spectrum shown in Figure 7.4 corresponds to the Design Earthquake (DE) level, thus for a return period of 475 years. The Maximum Considered Earthquake (MCE) site spectrum is obtained by multiplying the ordinates of the DE spectrum by a factor of 1.5, in accordance with the guidelines for Performance-Based Seismic Design of Tall Buildings, while the Service Level Earthquake (SLE) spectrum is obtained by dividing the ordinates of the DE spectrum by a reduction factor  $F_{ser}$  (MOC-CFE, 2015). For residential buildings that belong to group B, as the one considered in this case study, the value of the reduction factor  $F_{ser}$  is equal to 5.5 in accordance to MOC-CFE, 2015. Figure 7.5 shows the three site spectra obtained from the analysis described above.



*Figure 7.5 MCE, DBE and SLE site response spectra*

The obtained site response spectra are used, as explained in the following paragraphs, for the verification of the structure for the MCE and SLE performance levels.

The initial DE site spectrum is also adjusted to obtain an elastic design spectrum, which will be used for the design of the steel reinforcement of the bare frame structure, in accordance with the MOC-CFE building code. The elastic design spectrum for the Design Earthquake level is shown in Figure 7.6 and is characterized by:

- a first linear segment starting from the peak ground acceleration (PGA),  $a_0$ , to the maximum spectral acceleration,  $c$ ;
- a second segment, the plateau, defined by the range of periods between  $T_a$  and  $T_b$ , characterized by a constant spectral acceleration value equal to  $c$ ;
- a third exponential trait defined by the parameter  $p$ .

The mathematical expressions that describe the elastic design spectrum for the DE level are shown below:

$$S_a = a_0 + (c - a_0) \cdot \frac{T}{T_a} \quad 0 \leq T < T_a \quad (7.1)$$

---


$$S_a = c \quad T_a \leq T < T_b$$

$$S_a = p \cdot c \cdot \left(\frac{T_b}{T}\right)^2 \quad T \geq T_b$$

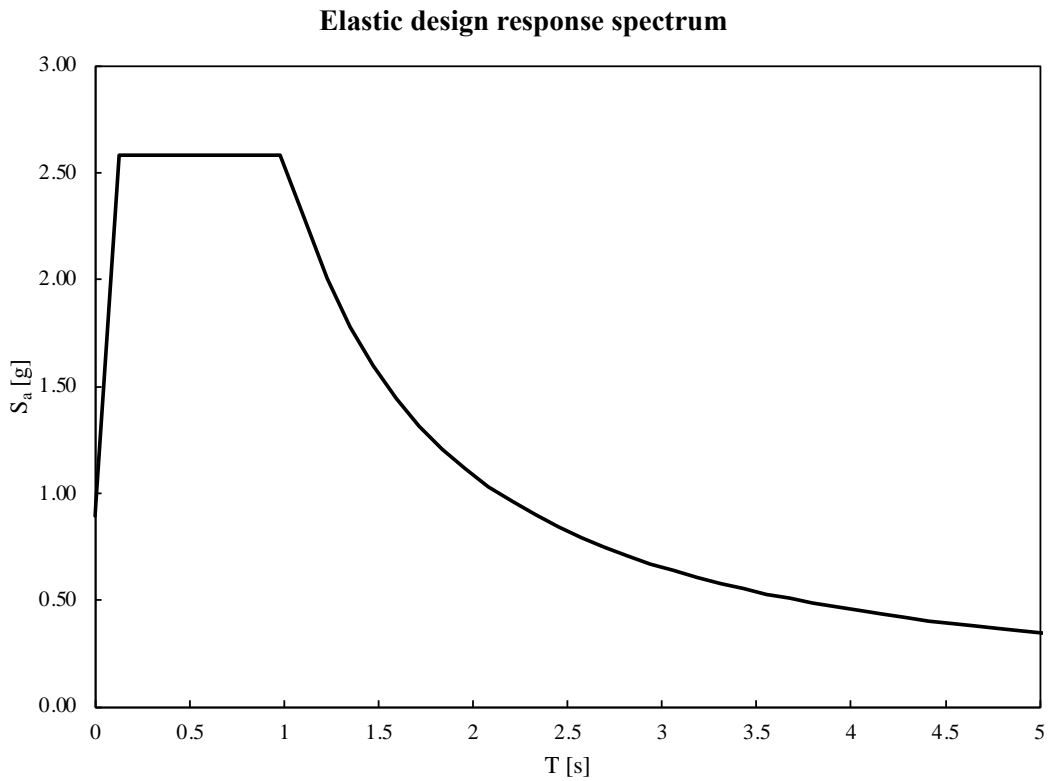
where  $T$  is the period of a single degree of freedom system,  $S_a$  is the acceleration spectral value and  $p$  is a coefficient that is calculated using the following expression:

$$p = k + (1 - k) \cdot \left(\frac{T_b}{T}\right)^2 \quad (7.2)$$

The seismic parameters values used in the equations (7.1) e (7.2) for the calculation of the design elastic spectrum are given in the Table 7.2.

*Table 7.2 Seismic parameters values for the elastic design response spectrum*

<b>Seismic parameters values - Elastic design response spectrum</b>					
<b><math>T_R</math></b>	<b><math>a_0</math></b>	<b><math>c</math></b>	<b><math>T_a</math></b>	<b><math>T_b</math></b>	<b><math>k</math></b>
<b>[years]</b>	<b>[g]</b>	<b>[g]</b>	<b>[s]</b>	<b>[s]</b>	<b>[-]</b>
475	0.895	2.58	0.10	1.00	1.5

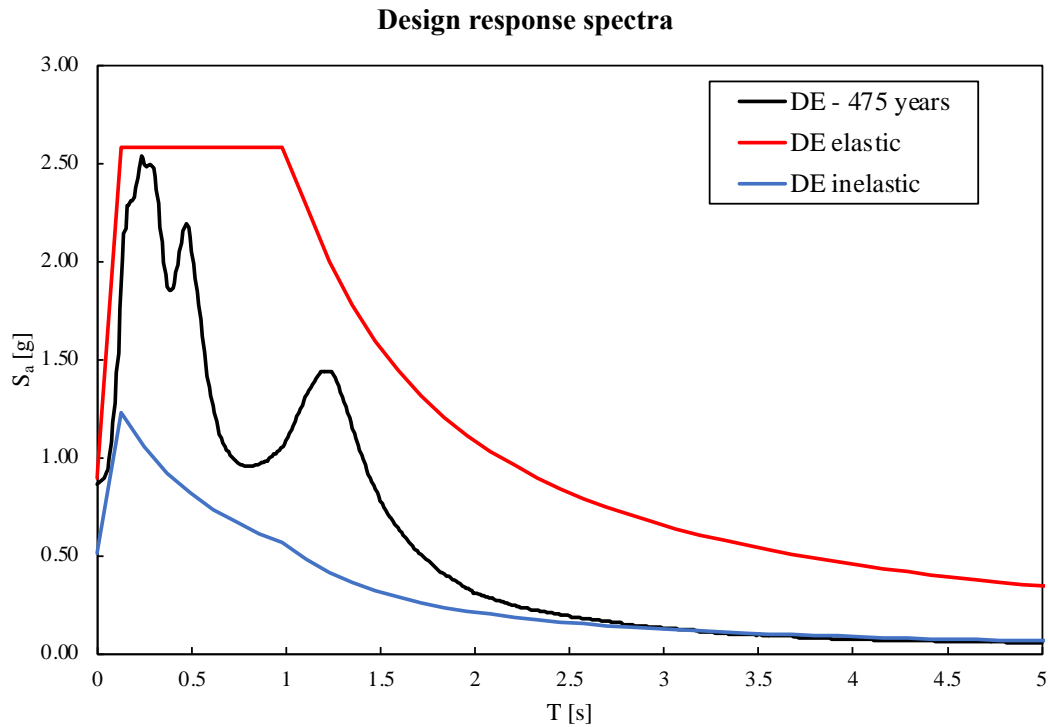


*Figure 7.6 Elastic design response spectrum*

The inelastic design spectrum is obtained dividing the ordinates of the elastic design response spectrum by an overstrength factor equal to 1.75 (MOC-CFE, 2015) and by a factor  $Q'$  calculated in accordance to the following expressions:

$$\begin{aligned}
 Q' &= 1 + \frac{(Q - 1)T}{\sqrt{k} \cdot T_b} & T \leq T_b \\
 Q' &= 1 + \frac{(Q - 1)\sqrt{p}}{\sqrt{k}} & T > T_b
 \end{aligned} \tag{7.3}$$

where  $Q$  is the behavior factor of the structure for seismic loads, that for a reinforced concrete structure in low ductility class is equal to 3 (MOC-CFE, 2015). The inelastic design spectrum given in Figure 7.7, that is obtained from the corresponding DE spectrum for a return period of 475 years, will be used for the reinforcement design of the bare frame structure, as explained in paragraph 7.5.4.



*Figure 7.7 Design Response Spectra*

### 7.3.2.2 Time Series record selection

As described in chapter 5, in the PBSD approach the proper selection and development of a set of site-specific time series is a very important step. MOC-CFE (2015) requires a minimum number of four accelerograms to verify the structure with linear or nonlinear time history analyses. In that case, accordingly to the code, it is necessary to consider the maximum values of the results to the evaluation of global and local acceptance criteria. However, if is used a minimum number of seven accelerograms, as for this case study, it is possible to evaluate global and local acceptance criteria using the mean values of the results obtained from the analyses.

The first five seismic signals showed below are taken from an accelerometer station located in Acapulco and which is approximately 3 kilometers from the building site, while the last two signals are selected considering significant magnitude and distance pairs for the study site.

Each time series is matched in order to be spectrally compatible to a site-specific target spectrum. The procedure is performed by means of the spectral matching approach in the frequency domain using ETABS. Following figures show the time series of the

seven seismic signals spectrally matched to the MCE site spectrum. For each seismic signal there are two time series, one for each horizontal direction.

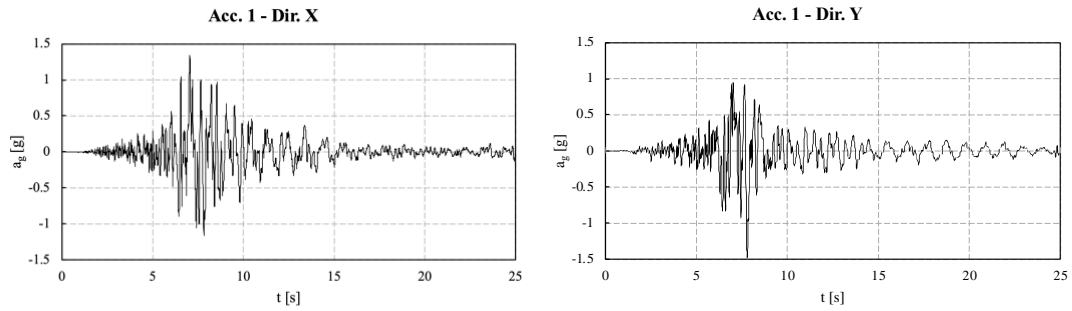


Figure 7.8 MCE matched seismic signal 1

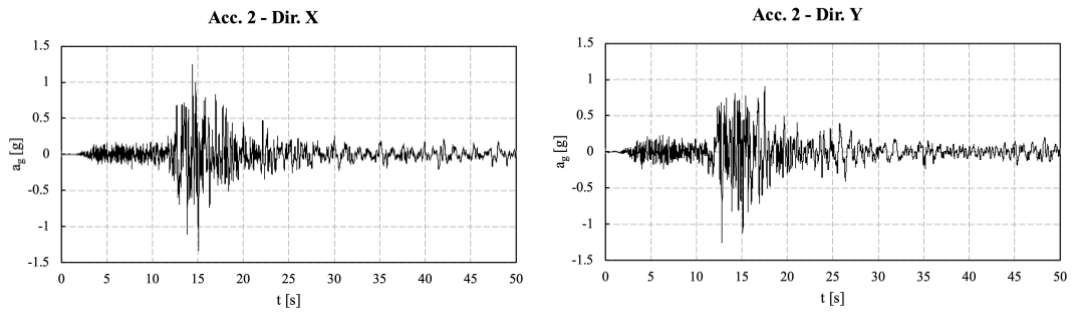


Figure 7.9 MCE matched seismic signal 2

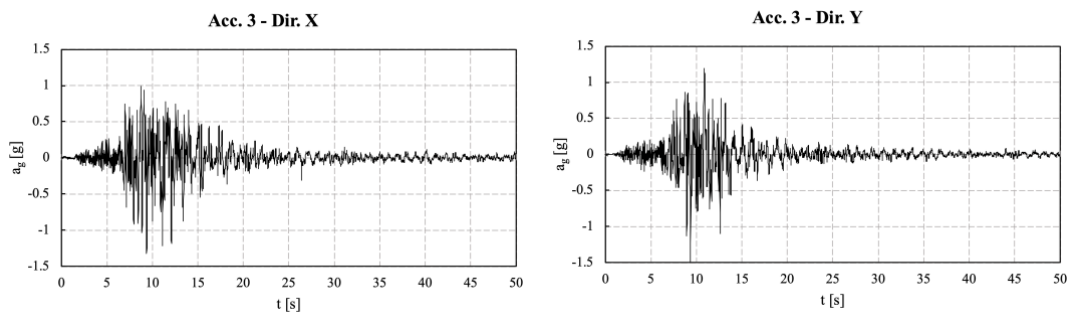


Figure 7.10 MCE matched seismic signal 3

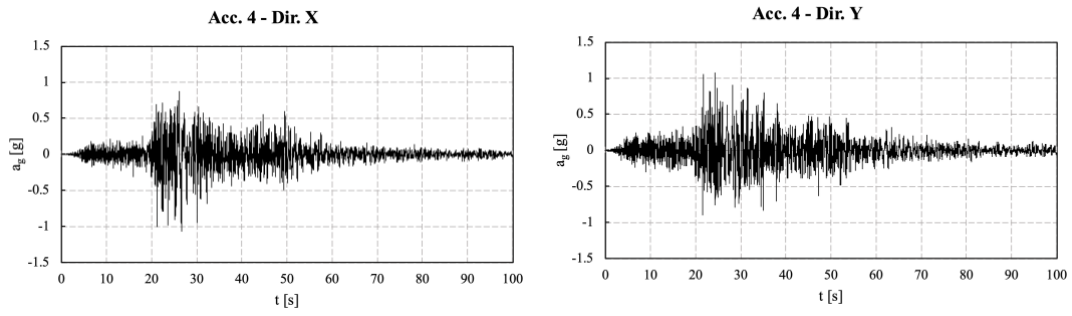


Figure 7.11 MCE matched seismic signal 4

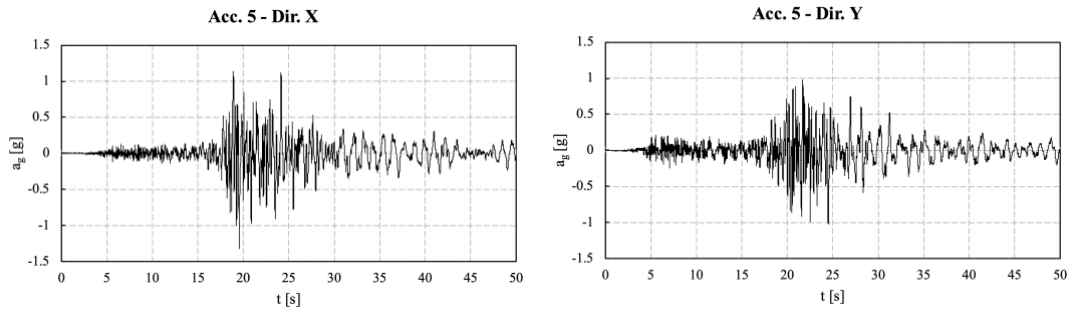


Figure 7.12 MCE matched seismic signal 5

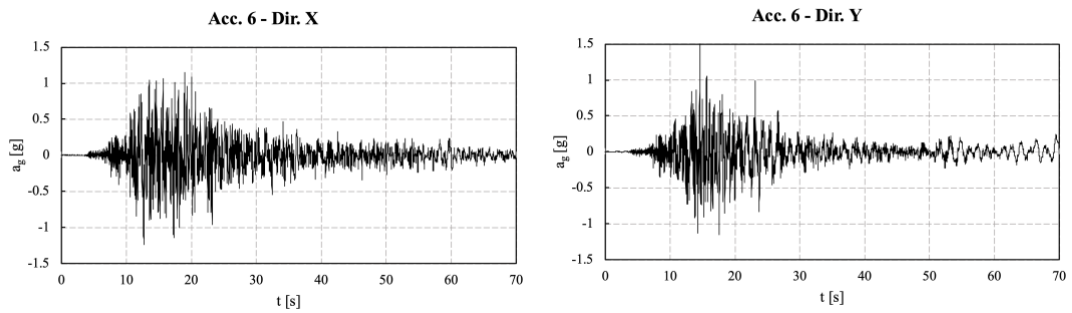


Figure 7.13 MCE matched seismic signal 6

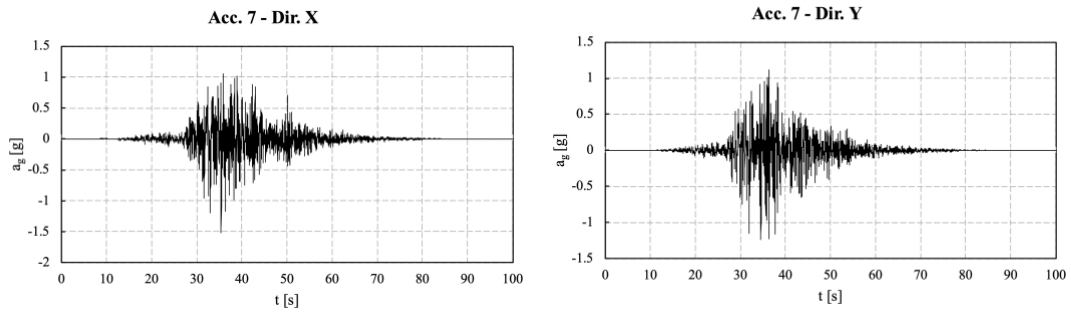


Figure 7.14 MCE matched seismic signal 7

Figure 7.15 shows the acceleration response spectra of matched seismic signals (in grey) and their mean spectrum (in green) versus the target MCE site spectrum (in black).

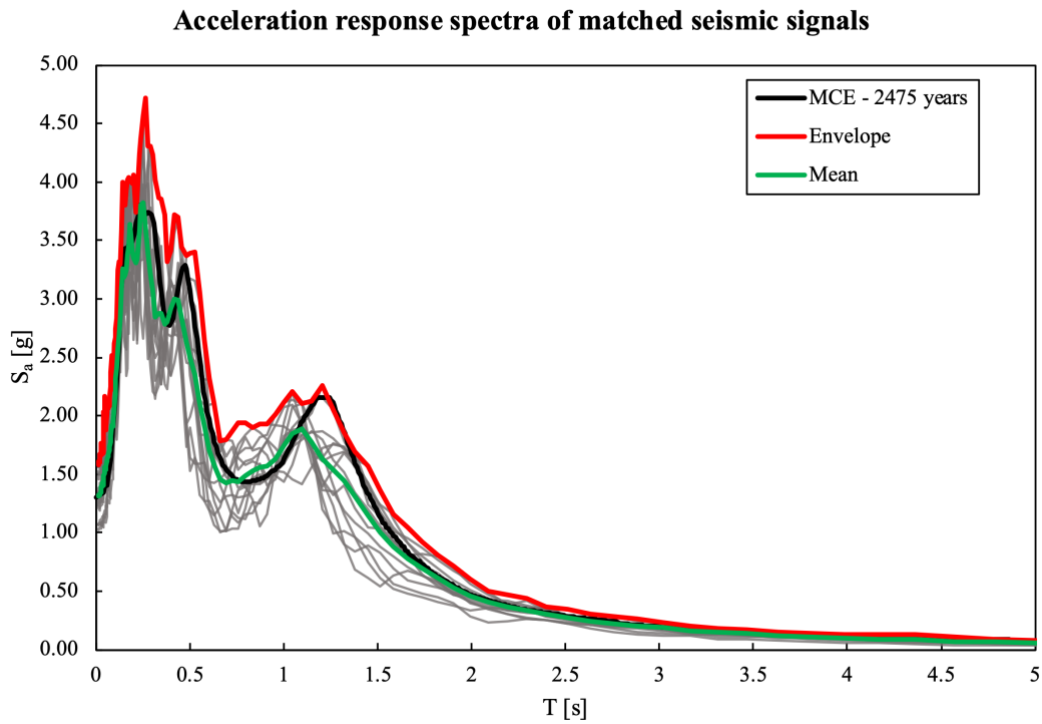


Figure 7.15 Acceleration response spectra of matched seismic signals

## 7.4 Modelling assumptions for the analyses

This section describes the modelling assumptions made for the analyses of the bare frame structure and the structure equipped with SLB devices. PBSD approach, as described in chapter 5, suggests to reduce the section properties to account for concrete



cracking and damage to structural elements through property modifiers, which values, accordingly to “*TBI – Guidelines for Performance-Based Seismic Design of Tall Buildings*”, are shown in Table 7.3.

Table 7.3 Reinforced concrete effective stiffness values

Component	Service-Level Linear Models			MCE <sub>R</sub> -Level Nonlinear Models		
	Axial	Flexural	Shear	Axial	Flexural	Shear
Structural walls <sup>1</sup> (in-plane)	$1.0E_cA_g$	$0.75E_cI_g$	$0.4E_cA_g$	$1.0E_cA_g$	$0.35E_cI_g$	$0.2E_cA_g$
Structural walls (out-of-plane)	--	$0.25E_cI_g$	--	--	$0.25E_cI_g$	--
Basement walls (in-plane)	$1.0E_cA_g$	$1.0E_cI_g$	$0.4E_cA_g$	$1.0E_cA_g$	$0.8E_cI_g$	$0.2E_cA_g$
Basement walls (out-of-plane)	--	$0.25E_cI_g$	--	--	$0.25E_cI_g$	--
Coupling beams with conventional or diagonal reinforcement	$1.0E_cA_g$	$0.07\left(\frac{\ell}{h}\right)E_cI_g$ $\leq 0.3E_cI_g$	$0.4E_cA_g$	$1.0E_cA_g$	$0.07\left(\frac{\ell}{h}\right)E_cI_g$ $\leq 0.3E_cI_g$	$0.4E_cA_g$
Composite steel / reinforced concrete coupling beams	$1.0(EA)_{trans}$	$0.07\left(\frac{\ell}{h}\right)(EI)_{trans}$	$1.0E_sA_{sw}$	$1.0(EA)_{trans}$	$0.07\left(\frac{\ell}{h}\right)(EI)_{trans}$	$1.0E_sA_{sw}$
Non-PT transfer diaphragms (in-plane only) <sup>3</sup>	$0.5E_cA_g$	$0.5E_cI_g$	$0.4E_cA_g$	$0.25E_cA_g$	$0.25E_cI_g$	$0.1E_cA_g$
PT transfer diaphragms (in-plane only) <sup>3</sup>	$0.8E_cA_g$	$0.8E_cI_g$	$0.4E_cA_g$	$0.5E_cA_g$	$0.5E_cI_g$	$0.2E_cA_g$
Beams	$1.0E_cA_g$	$0.5E_cI_g$	$0.4E_cA_g$	$1.0E_cA_g$	$0.3E_cI_g$	$0.4E_cA_g$
Columns	$1.0E_cA_g$	$0.7E_cI_g$	$0.4E_cA_g$	$1.0E_cA_g$	$0.7E_cI_g$	$0.4E_cA_g$
Mat (in-plane)	$0.8E_cA_g$	$0.8E_cI_g$	$0.8E_cA_g$	$0.5E_cA_g$	$0.5E_cI_g$	$0.5E_cA_g$
Mat <sup>4</sup> (out-of-plane)	--	$0.8E_cI_g$	--	--	$0.5E_cI_g$	--

<sup>1</sup>Values are relevant where walls are modeled as line elements. Where walls are modeled using fiber elements, the model should automatically account for cracking of concrete and the associated effects on member stiffness.

<sup>2</sup> $(EI)_{trans}$  is intended to represent the flexural rigidity of the cracked transformed section. It is acceptable to calculate the transformed section properties based on structural mechanics or to use  $(EI)_{trans} = E_cI_g/5 + E_sI_s$  per ACI 318.

<sup>3</sup>Specified stiffness values for diaphragms are intended to represent expected values. Alternative values may be suitable where bounding analyses are used to estimate bounds of force transfers at major transfer levels. For diaphragms that are not associated with major force transfers, common practice is to model the diaphragm as being rigid in its plane. Flexural rigidity of diaphragms out of plane is usually relatively low and is commonly ignored. The exception is where the diaphragm acts as a framing element to engage gravity columns as outrigger elements, in which case out-of-plane modeling may be required.

<sup>4</sup>Specified stiffness values for mat foundations pertain to the general condition of the mat. Where the walls or other vertical members impose sufficiently large forces, including local force reversals across stacked wall openings, the stiffness values may need to be reduced.

It is important to take into account that the RC effective stiffness values depend on earthquake intensity. This means that two different structural models need to be

realized for each structure, one for Service Level Earthquake (SLE) analyses and one for Maximum Considered Earthquake (MCE) analyses. The SLE effective stiffness values are also considered for the reinforcement steel design, accordingly to MOC-CFE building code.

A further fundamental aspect for MCE analyses is the nonlinear modelling of the structures. Chapter 6 describes the main theoretical elements of nonlinear modelling, so this section only defines the modelling assumptions made for the case study. Concentrated plastic hinge model has been assumed for rectangular and circular cross-section RC elements following ASCE 41-13 recommendations. Fiber hinge model has been taken for L shape cross-section columns, discretizing the section into a number of uniaxial fibers arranged along the longitudinal axis of the element and assigning a uniaxial stress-strain relationship to each of them. In this case, the acceptance criteria (IO, LS, CP) are specified directly on the material stress-strain relationship.

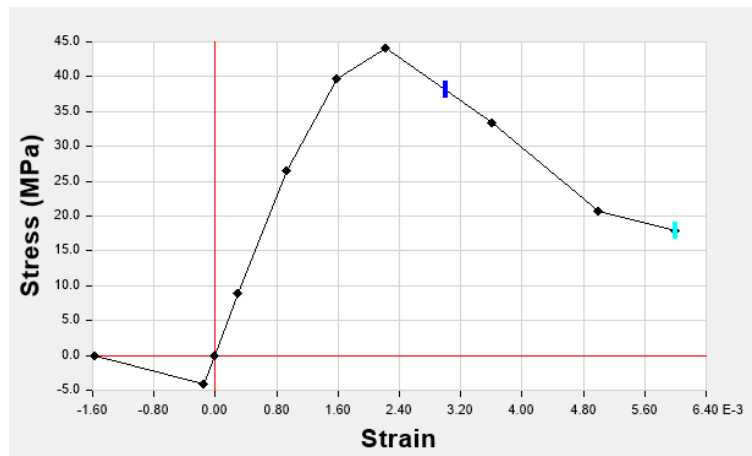


Figure 7.16 Concrete C45 - Material stress-strain relationship

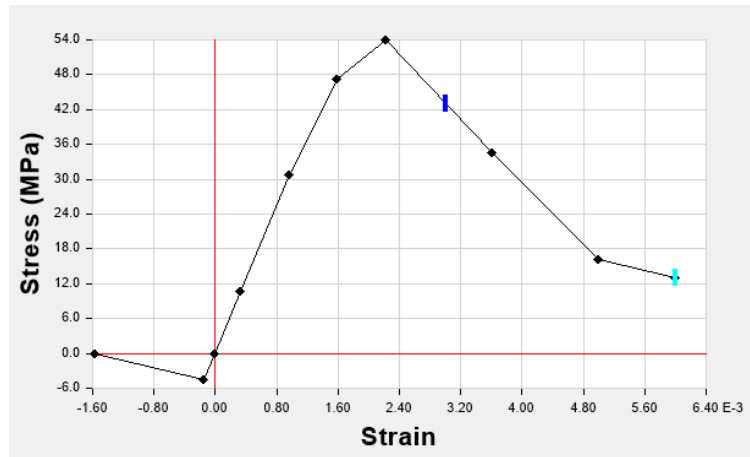


Figure 7.17 Concrete C55 - Material stress-strain relationship

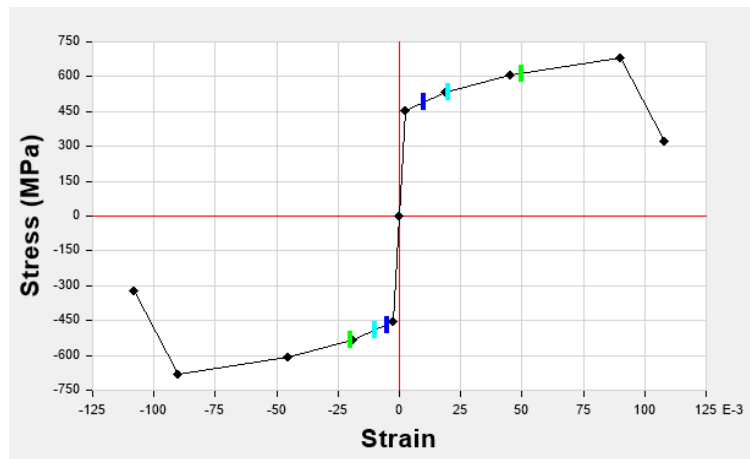


Figure 7.18 Steel A615Gr60 - Material stress-strain relationship

P- $\Delta$  effects have been considered in all the static and dynamic analyses carried out for the case study. The “Hilber-Hughes-Taylor alpha” method, introduced in section 6.3.2, has been used for performing direct-integration time-history analyses using  $\alpha = 0$  (see section 6.3.2), while the damping matrix has been calculated following the *Rayleigh damping method* (see section 6.3.1).

## 7.5 Bare frame structure design

### 7.5.1 Modal analysis

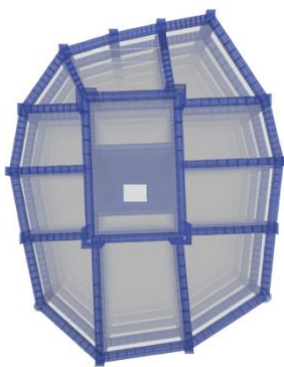
The first step is to perform a modal analysis with the aim to study the dynamic behavior of the bare frame structure. Table 7.4 shows periods and modal mass participating

mass ratios ( $m_x$ ,  $m_y$ ,  $r_z$ ) of the first three natural modes of vibration of the structure. The results are obtained considering the effective stiffness values of the Service Level Earthquake (see Table 7.3).

*Table 7.4 Modal analysis results for Bare frame structure*

Mode	Period	Participating Mass Ratio ( $m_x$ , $m_y$ , $r_z$ )			Sum Participating Mass Ratio ( $m_x$ , $m_y$ , $r_z$ )		
		[-]	[-]	[-]	[-]	[-]	[-]
1	3.32	34.07%	28.08%	14.66%	34.07%	28.08%	14.66%
2	3.23	28.44%	45.77%	1.36%	62.51%	73.85%	16.02%
3	2.51	12.87%	2.21%	61.88%	75.38%	76.06%	77.90%
9	0.46	1.11%	0.13%	2.76%	90.92%	90.91%	91.65%

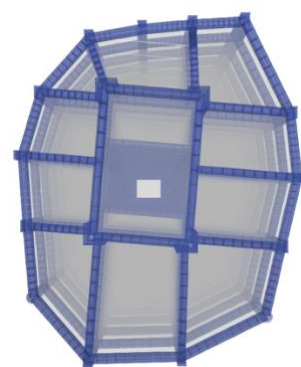
Results given in Table 7.4 shows that the first and second mode are essentially translational, while the third one is torsional. This ensures that the building is torsionally rigid, thus avoiding excessive stresses due to the torsion of the structure.



*Figure 7.19 1<sup>st</sup> mode*



*Figure 7.20 2<sup>nd</sup> mode*



*Figure 7.21 3<sup>rd</sup> mode*

The fundamental period is 3.32 seconds, a value that is acceptable for a 25-story reinforced concrete building, while 90% of the participating mass ratio is achieved in all directions considering the first 9 natural modes of vibrations of the structure.

### 7.5.2 Service Level Earthquake evaluation

The next step consists to verify the structure to the Service Level Earthquake according to MOC-CFE requirements. The interstory-drift results, given in Figure 7.22, are obtained with a response spectrum analysis using the SLE site spectrum introduced in Figure 7.5 and considering the load combinations defined in section 7.3.

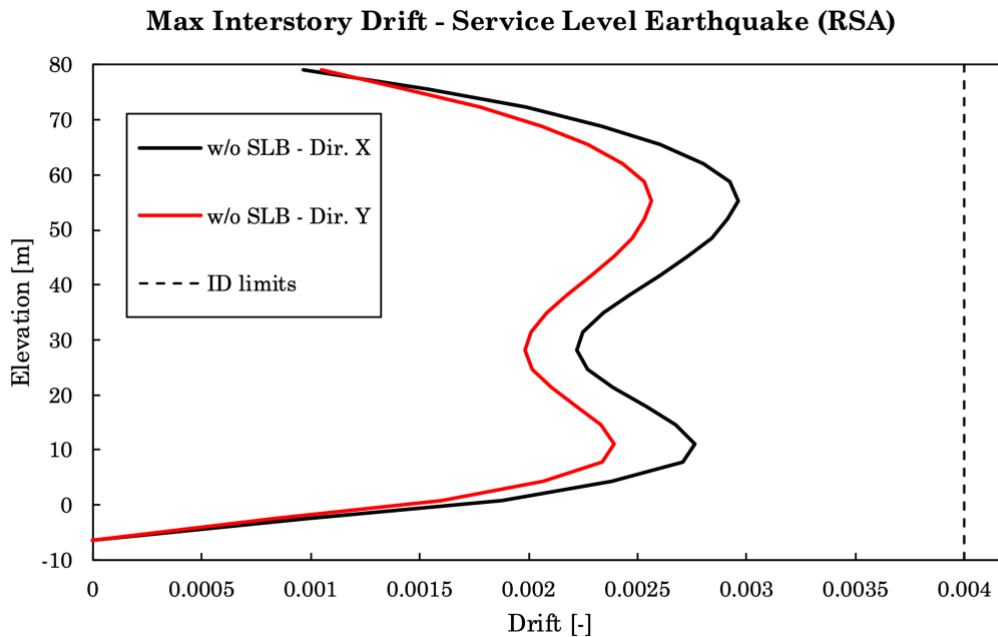
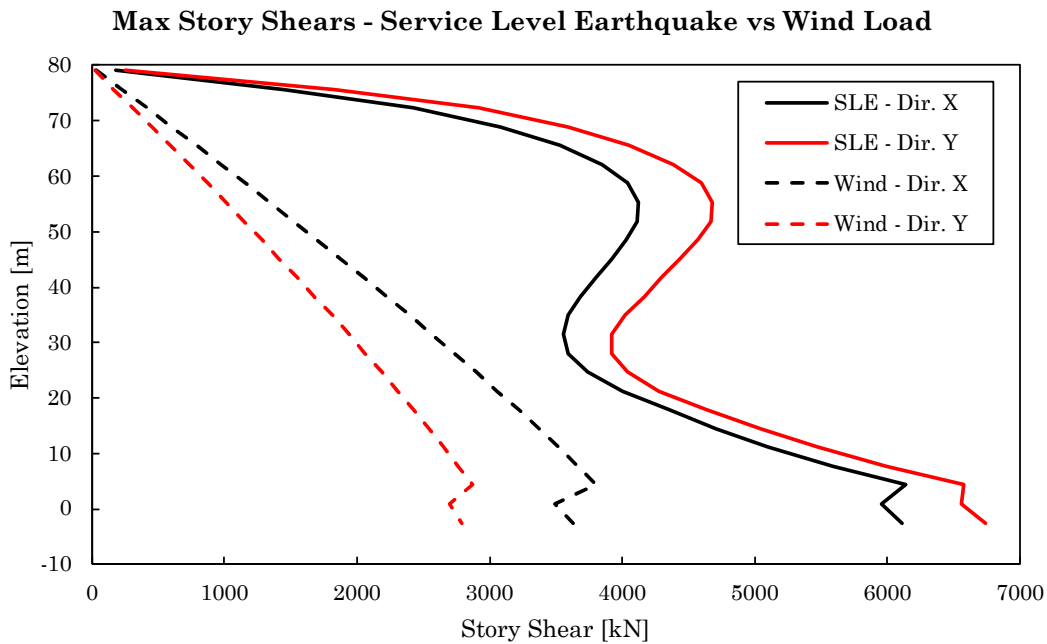


Figure 7.22 Max Interstory Drift at Service Level Earthquake (RSA)

### 7.5.3 Considerations of wind demand

Generally, for the structural design of high-rise buildings the wind load demand can be even more significant than the seismic demand at Service Level Earthquake (SLE): Thus, the wind demand, if is expected to affect the structural design, must be considered in the first step of the assessment of the structure, as explained in the *TBI – Guidelines for Performance Based Seismic Design of Tall Buildings, 2017* and in *Performance-Based Seismic Design for Tall Buildings* (Golesorkhi et al., 2019).

Figure 7.23 shows the story shears comparison between the seismic load combination at SLE and wind demand, the latter is given in section 7.3.



*Figure 7.23 Max Story Shears - Service Level Earthquake vs Wind Load*

The story shears values of wind load combination are lower than the ones obtained from the seismic load combination at Service Level Earthquake. In conclusion, the wind demand does not affect the evaluation of the structure in terms of interstory drift-results. However, the wind demand has been considered in the design of the structural elements of the two structures with and without SLB devices.

### 7.5.4 Reinforcement design

This paragraph describes the reinforcement design of structural elements (beams and columns), that has been carried out after the verification of the structure at Service Level Earthquake. The steel reinforcement has been calculated with a traditional capacity design approach, following the ACI 318-19 prescriptions, considering the maximum stresses in structural elements due to gravity loads and seismic loads combinations. The seismic loads effects on the structure have been computed with a *Response Spectrum analysis* (RSA) using the inelastic design spectrum introduced in Figure 7.7.

The beam reinforcement design is conducted subdividing the structural element into three parts, as shown in Figure 7.24: two end sections where is expected the formation

of plastic hinges, and one mid-section where the stresses due to gravity and seismic loads are generally lower and therefore less steel is required.

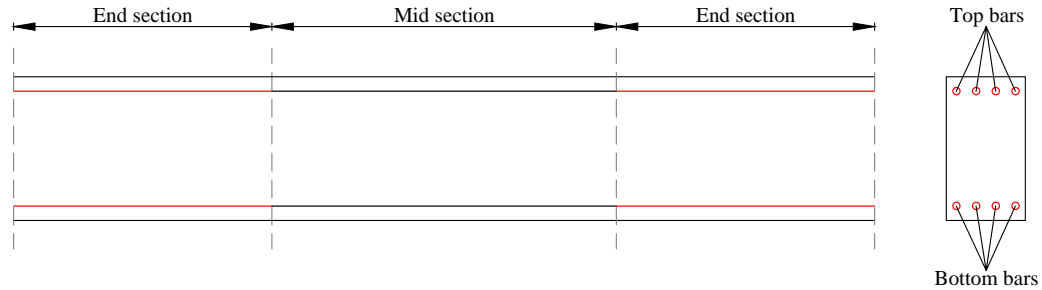


Figure 7.24 Subdivision of the beam for the reinforcement design

Table 7.5 contains the amount of steel reinforcement for beam sections obtained by the design procedure. The coefficients  $\rho_{s,bot}$  and  $\rho_{s,top}$  represent the bottom and top geometric percentage of reinforcement, defined as:

$$\rho_{s,bot} = \frac{A_{s,bot}}{A_c} \quad \rho_{s,top} = \frac{A_{s,top}}{A_c} \quad (7.4)$$

where  $A_c$  is the concrete area of the section.

Table 7.5 Reinforcement design for Bare frame structure - Beam sections

End section														Mid section				
Section	$A_c$	$\Phi$	Num. of bars	$A_{s,bot}$	$A_{s,top}$	$\rho_{s,bot}$	$\rho_{s,top}$	$\Phi$	Num. of bars	$A_{s,bot}$	$A_{s,top}$	$\rho_{s,bot}$	$\rho_{s,top}$					
[-]	[cm <sup>2</sup> ]	[mm]	[-]	[cm <sup>2</sup> ]	[cm <sup>2</sup> ]	[-]	[-]	[mm]	[-]	[cm <sup>2</sup> ]	[cm <sup>2</sup> ]	[-]	[-]					
TR 50X110 0.5%	5500	25.4	6	30.40	30.40	0.55%	0.55%	25.4	6	30.40	30.40	0.55%	0.55%					
TR 50X110 1%	5500	25.4	11	55.74	55.74	1.01%	1.01%	25.4	6	30.40	30.40	0.55%	0.55%					
TR 50X110 1.5%	5500	32.3	11	90.13	90.13	1.64%	1.64%	25.4	6	30.40	30.40	0.55%	0.55%					
TR 50X110 2%	5500	32.3	14	114.72	114.72	2.09%	2.09%	25.4	6	30.40	30.40	0.55%	0.55%					
TR 50X110 2.5%	5500	32.3	18	147.49	147.49	2.68%	2.68%	25.4	6	30.40	30.40	0.55%	0.55%					
TR 55X70 0.5%	3850	25.4	4	20.27	20.27	0.53%	0.53%	25.4	4	20.27	20.27	0.53%	0.53%					
TR 55X70 1%	3850	25.4	8	40.54	40.54	1.05%	1.05%	25.4	4	20.27	20.27	0.53%	0.53%					
TR 55X70 1.5%	3850	25.4	12	60.80	60.80	1.58%	1.58%	25.4	4	20.27	20.27	0.53%	0.53%					
TR 55X70 2%	3850	32.3	10	81.94	81.94	2.13%	2.13%	25.4	4	20.27	20.27	0.53%	0.53%					
TR 55X70 2.5%	3850	32.3	12	98.33	98.33	2.55%	2.55%	25.4	4	20.27	20.27	0.53%	0.53%					
TR 40X100 0.5%	4000	25.4	4	20.27	20.27	0.51%	0.51%	25.4	4	20.27	20.27	0.51%	0.51%					
TR 40X100 1%	4000	25.4	8	40.54	40.54	1.01%	1.01%	25.4	4	20.27	20.27	0.51%	0.51%					
TR 40X100 1.5%	4000	25.4	12	60.80	60.80	1.52%	1.52%	25.4	4	20.27	20.27	0.51%	0.51%					
TR 40X100 2%	4000	32.3	10	81.94	81.94	2.05%	2.05%	25.4	4	20.27	20.27	0.51%	0.51%					
TR 40X100 2.5%	4000	32.3	12	98.33	98.33	2.46%	2.46%	25.4	4	20.27	20.27	0.51%	0.51%					

Table 7.6 contains the amount of steel reinforcement for beam sections obtained by the design procedure. The coefficient  $\rho_s$  represents the total geometric percentage of reinforcement, defined as:

$$\rho_s = \frac{A_s}{A_c} \quad (7.5)$$

Table 7.6 Reinforcement design for Bare frame structure - Column sections

Section [-]	A <sub>c</sub> [cm <sup>2</sup> ]	Φ [mm]	Num. of bars [-]	A <sub>s,tot</sub> [cm <sup>2</sup> ]	ρ <sub>s</sub> [-]
COL 70X125	8750	25.4	48	243.22	2.78%
COL 70X150	10500	32.3	48	393.31	3.75%
COL 80X175	14000	32.3	76	622.74	4.45%
COL 90X100	9000	25.4	36	182.41	2.03%
COL 90X125	11250	32.3	36	294.98	2.62%
COL 90X150	13500	32.3	44	360.54	2.67%
COL 90X175	15750	32.3	76	622.74	3.95%
COL 100	7854	25.4	30	152.01	1.94%
COL 120	11310	25.4	30	152.01	1.34%
COL 140	15394	32.3	60	491.64	3.19%
COL L 70X150	16100	25.4	55	278.69	1.73%
COL L 70X180	20300	32.3	67	549.00	2.70%
COL L 80X180	22400	32.3	83	680.10	3.04%

### 7.5.5 MCE analyses results

This paragraph shows the results obtained with nonlinear time history analyses at MCE level after the reinforcement design of structural elements. In this case, the damping matrix has been calculated following the *Rayleigh damping method*, as described in paragraph 6.3.1, as a linear combination of the stiffness matrix  $\mathbf{K}$ , scaled by a coefficient  $c_K$ , and the mass matrix  $\mathbf{M}$ , scaled by a second coefficient  $c_M$  (see eq. (6.3)). The two coefficients  $c_M$  and  $c_K$  of eq. (6.3) have been computed setting a same modal damping ratio ( $\xi_i = 5\%$ ) at two different natural periods of the structure, that correspond to the first modal period and the period required to achieve 90% mass participation in all the directions. It is important to highlight that the MCE structural model is characterized by specific effective stiffness values, that are different from the ones used in the SLE model. Therefore, the coefficients  $c_M$  and  $c_K$  need to be calibrated according to the modal analysis results of MCE structural model.



Modal Load Case

Viscous Proportional Damping

☐ Direct Specification
 ☒ Specify Damping by Period
 ☐ Specify Damping by Frequency

☐ Specify as Period Ratio,  $T/T_{mode}$ , for This Mode

	Period	Frequency	Damping
First	4.127 sec	cyc/sec	0.05
Second	0.554 sec	cyc/sec	0.05

Recalculate Coefficients

Additional Modal Damping

☐ Include Additional Modal Damping

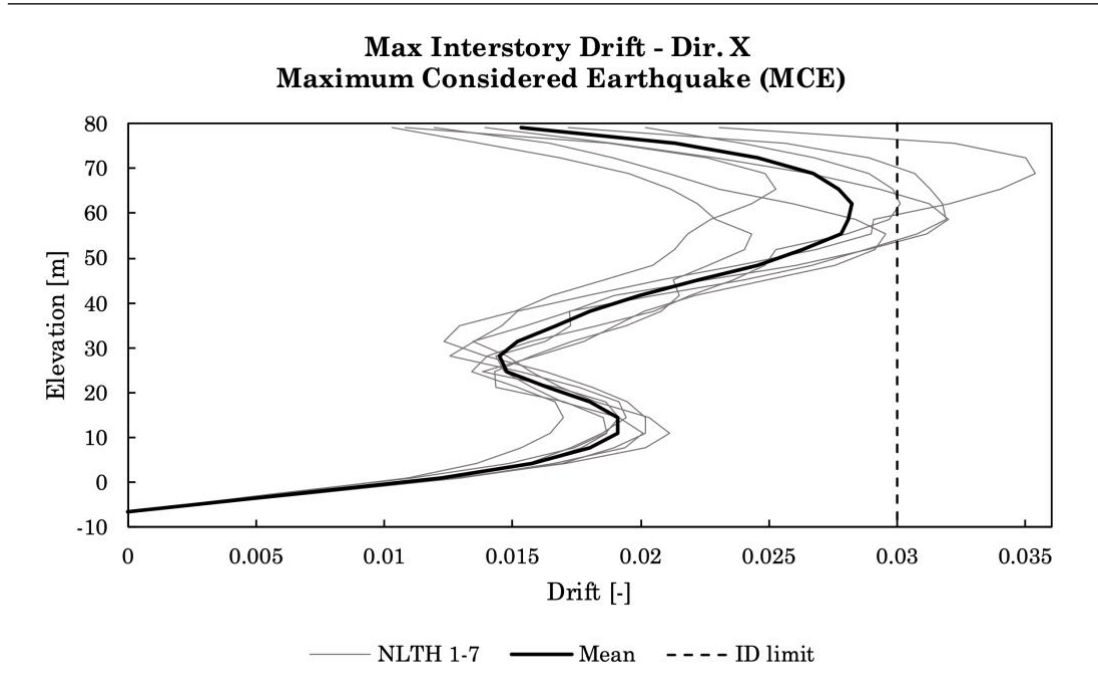
☐ Maximum Considered Modal Frequency

Modify/Show Modal Damping Parameters...

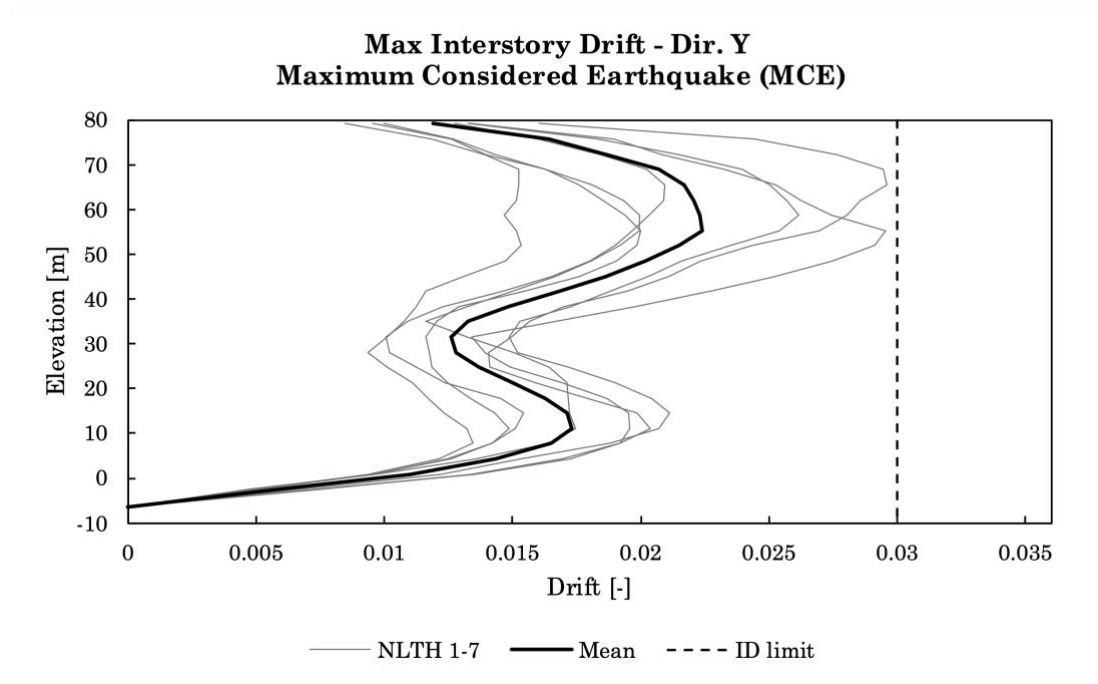
OK Cancel

Figure 7.25 Damping coefficients for Nonlinear time history analysis - ETABS

A set of 7 seismic signals has been used for performing the nonlinear time history analyses, thus, as described in section 7.3.2.2, the mean values of results has been considered to evaluate global and local acceptance criteria. Figure 7.26 and Figure 7.27 shows the max interstory drift results at MCE level.



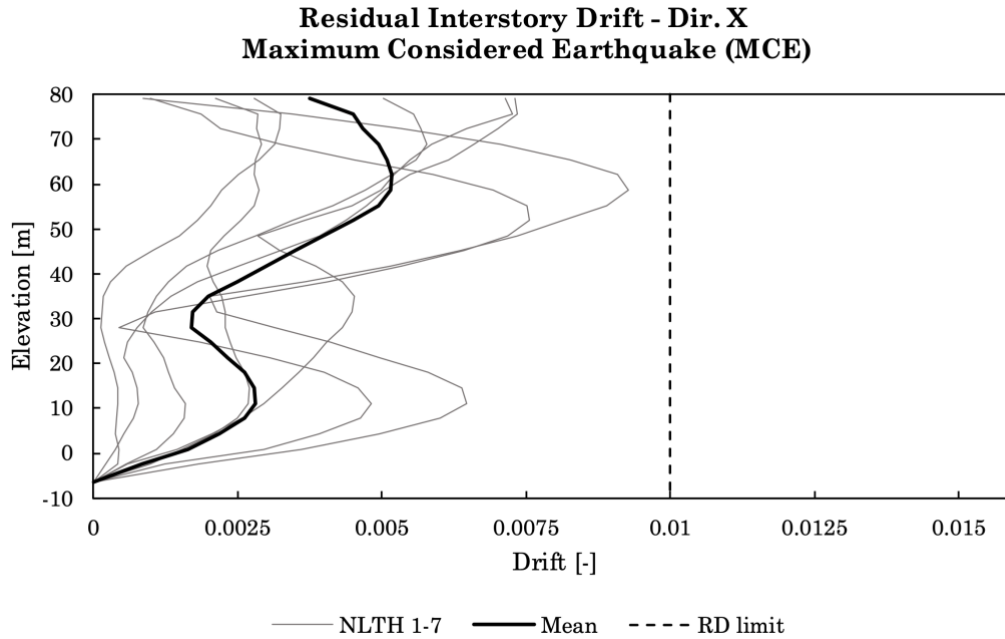
*Figure 7.26 Max interstory Drift at MCE level - Dir. X*



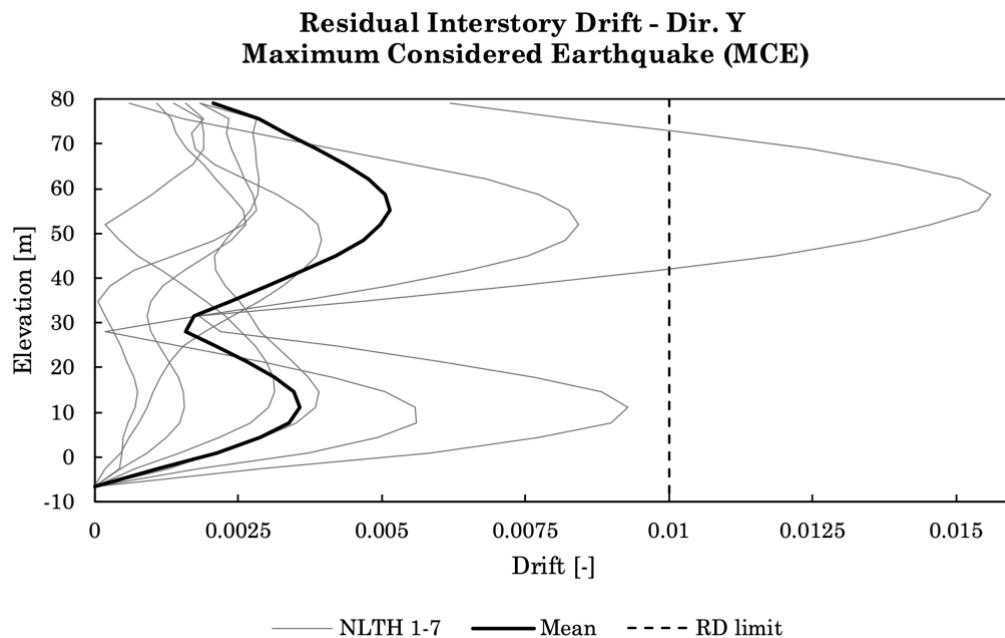
*Figure 7.27 Max Interstory Drift at MCE level - Dir. Y*

The maximum interstory drift is lower than limit in both directions, so the MOC-CFE requirements are satisfied. The mean values of residual interstory drift ratio obtained from the analyses, according to the TBI-Guideline (see section 7.2.1), shall not exceed

0.01 for protecting the building against excessive post-earthquakes. Figure 7.28 and Figure 7.29 show the residual interstory drift results at MCE level.



*Figure 7.28 Residual Interstory Drift at MCE level - Dir. X*



*Figure 7.29 Residual Interstory Drift at MCE level - Dir. Y*

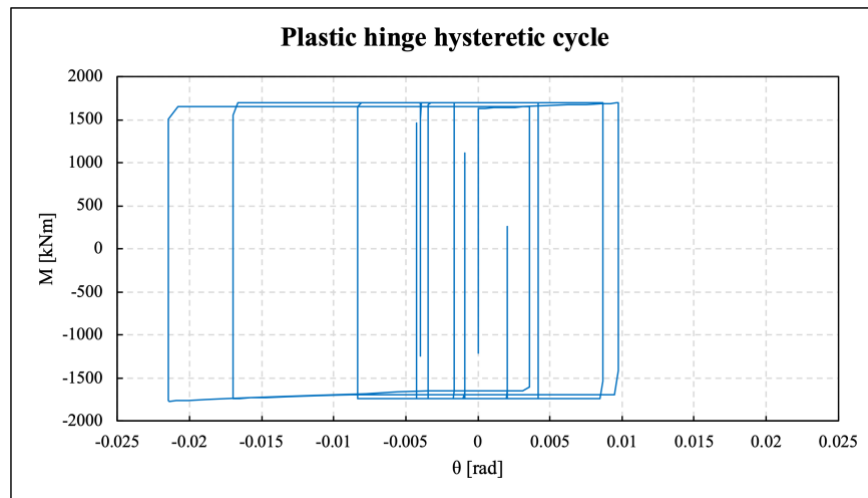
The residual interstory drift ratios are lower than limit in both directions, so the TBI-Guidelines requirements are satisfied. In conclusion, the results of nonlinear time history analyses at MCE level meet the global acceptance criteria.

Lastly, it is necessary to verify that the structure meets the local acceptance criteria. Therefore, plastic rotations in structural elements (beams and columns need to be lower than Collapse Prevention (CP) value. Numerical acceptance criteria for beams and columns, as described in section 7.2, are taken from ASCE 41-13.

Table 7.7 shows the maximum and mean demand on capacity ratios for CP of each structural element. The maximum D/C ratio is calculated on the results of the single nonlinear time history analysis, while the mean D/C ratio is calculated on the results of the entire set of accelerograms.

*Table 7.7 Mean and Maximum D/C ratios for Collapse Prevention (CP) - Bare structure*

Element	Mean D/C for CP	Max D/C for CP
[-]	[-]	[-]
Beam	0.714	0.999
Column	0.238	0.450



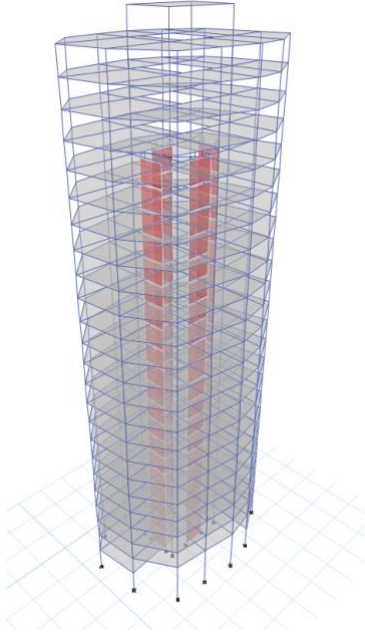
*Figure 7.30 Example of the plastic hinge hysteretic cycle of a beam*

## 7.6 Structure with SLB design

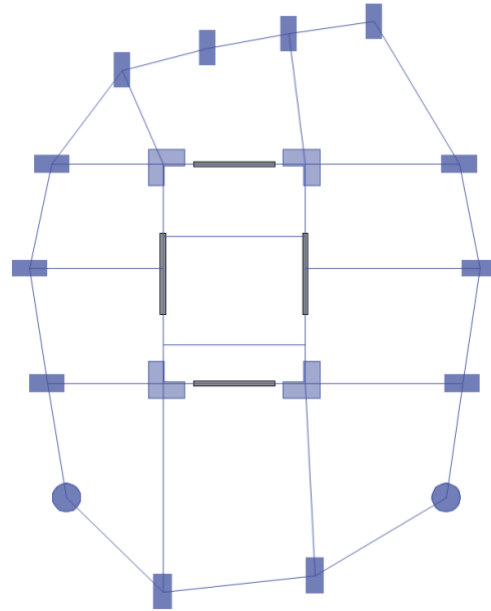
### 7.6.1 SLB design

The employment of 4<sup>th</sup> generation SLB devices has been proposed for the project of Baia, using decoupled concrete walls as support for the devices. The plan layout of

SLB devices and the concrete wall geometry, shown in Figure 7.32, have been defined taking into account the limitations imposed by the architectural design.

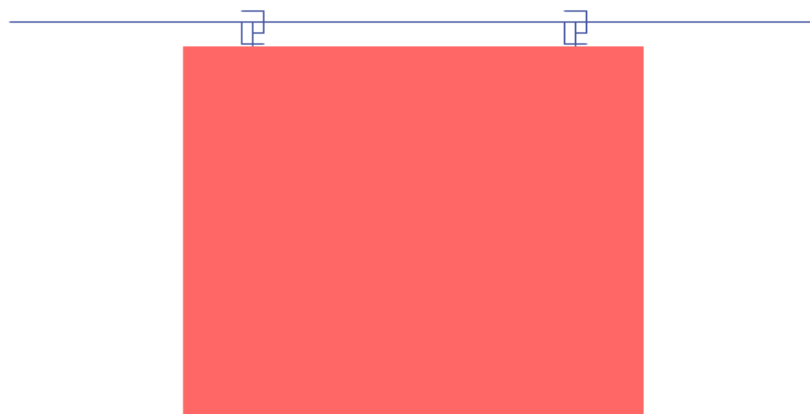


*Figure 7.31 Structure with SLB 3D model*



*Figure 7.32 Plan of the building*

The proposed SLB solution consists of four concrete walls per level, as shown in Figure 7.31, placed from story 1 to story 20. Each wall is equipped with 2 SLB devices and is characterized by a 4 meters length and 25 centimeters thickness.



*Figure 7.33 Decoupled wall FEM model - ETABS*

The shear capacity of a structural concrete wall according to the ACI code can be calculated with the following expression (units in MPa):

$$V_d = 0.75 \cdot 0.83 \cdot \sqrt{f_{ck}} \cdot L \cdot t \quad (7.6)$$

where:

- $f_{ck}$  is the compressive strength of the concrete;
- $L$  is the length of the wall;
- $t$  is the thickness of the wall.

Table 7.8 summarizes the geometrical and mechanical properties of the decoupled concrete walls considered for this case study.

*Table 7.8 Geometric and mechanical properties of decoupled concrete walls*

<b>Concrete</b>	<b><math>f_{ck}</math></b>	<b>L</b>	<b>t</b>	<b><math>V_d</math></b>
<b>[-]</b>	<b>[MPa]</b>	<b>[m]</b>	<b>[cm]</b>	<b>[kN]</b>
C45	45	4.00	25	4176

The selection procedure of SLB devices has been performed using the direct iteration method described in section 4.3.1, resulting in an initial set of devices. Then, the optimal solution has been achieved reducing the size of dissipators with a series of nonlinear time history analyses considering only the nonlinear behavior of dissipators.

*Table 7.9 Design Table for 4<sup>th</sup> generation of Shear Link Bozzo devices*

Device	K <sub>1</sub> (KN/cm)	K <sub>2</sub> (KN/cm)	D <sub>y</sub> (mm)	F <sub>y</sub> (KN)	F <sub>max</sub> (KN)
SLB4_10_5	2026.65	21.62	0.749	151.79	250.00
SLB4_10_6	2163.53	22.90	0.742	160.54	265.78
SLB4_15_5	2472.60	24.85	0.720	177.92	293.72
SLB4_15_6	2761.73	26.96	0.706	195.09	320.62
SLB4_15_7	3021.88	28.76	0.697	210.76	345.09
SLB4_20_6	3361.00	33.09	0.687	230.93	381.61
SLB4_20_7	3700.15	35.28	0.673	248.98	410.70
SLB4_25_6	4260.80	42.53	0.654	278.74	468.96
SLB4_25_7	4767.68	46.51	0.638	304.31	512.31
SLB4_25_8	5238.65	50.43	0.626	327.73	552.76
SLB4_30_7	5785.96	57.25	0.619	358.28	611.14
SLB4_30_8	6419.52	62.36	0.608	390.28	665.17
SLB4_30_9	6994.22	66.79	0.601	420.37	716.61
SLB4_30_10	7535.22	70.90	0.596	449.29	764.52
SLB4_40_7	7797.49	78.07	0.596	464.68	807.56
SLB4_40_8	8718.88	86.41	0.588	512.48	890.20
SLB4_40_9	9580.18	93.66	0.582	557.71	966.06
SLB4_40_10	10439.63	101.20	0.576	601.31	1043.20
SLB4_40_11	11253.53	109.93	0.571	643.06	1117.73
SLB4_40_12	12033.64	115.64	0.570	685.73	1191.30
SLB4_50_9	12289.99	120.57	0.578	709.95	1236.23
SLB4_50_10	13421.60	130.96	0.572	768.20	1340.09
SLB4_50_11	14537.41	141.39	0.569	827.48	1443.52
SLB4_50_12	15599.37	150.54	0.567	884.08	1540.02
SLB4_60_5	8891.13	91.74	0.598	531.45	932.94
SLB4_60_6	10457.28	106.25	0.586	613.19	1078.09
SLB4_60_11	17684.45	174.36	0.562	993.08	1746.50
SLB4_60_12	19029.62	185.88	0.560	1065.32	1868.98
SLB4_65_11	19829.08	194.60	0.562	1113.76	1957.04
SLB4_65_12	21326.70	209.74	0.560	1194.73	2103.54
SLB4_65_13	22872.65	223.05	0.558	1276.57	2245.62
SLB4_65_14	24379.36	235.06	0.556	1356.52	2382.04
SLB4_65_15	25869.86	249.17	0.554	1433.77	2519.93
SLB4_65_16	27331.55	261.77	0.553	1511.96	2654.85
SLB4_65_18	30180.37	286.67	0.554	1671.12	2912.47
SLB4_65_20	32951.18	306.56	0.553	1822.60	3157.88

For each decoupled concrete wall, according to its the shear capacity shown in Table 7.8, is it possible to install up to two SLB4\_65\_11 (see Table 7.9). However, the

optimal design solution consists in the use of two SLB4\_40\_10 for each decoupled wall, for a total of 160 devices.

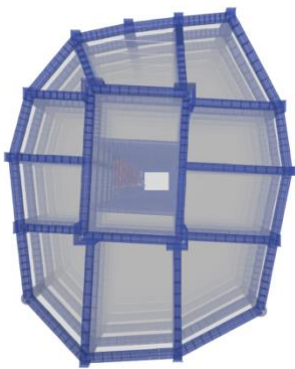
### 7.6.2 Modal analysis

The first step, as previously done for the bare frame structure, is to perform a modal analysis with the aim to study the dynamic behavior of the structure. Table 7.10 shows periods and modal mass participating mass ratios ( $m_x$ ,  $m_y$ ,  $r_z$ ) of the first three natural modes of vibration of the structure. The results are obtained considering the effective stiffness values of the Service Level Earthquake (see Table 7.3).

*Table 7.10 Modal analysis results for SLB structure*

Mode	Period	Participating Mass Ratio ( $m_x$ , $m_y$ , $r_z$ )			Sum Participating Mass Ratio ( $m_x$ , $m_y$ , $r_z$ )		
		[-]	[-]	[-]	[-]	[-]	[-]
1	2.49	47.03%	3.84%	23.09%	47.03%	3.84%	23.09%
2	2.25	9.59%	61.99%	2.50%	56.62%	65.83%	25.59%
3	2.01	14.33%	8.47%	52.38%	70.95%	74.30%	77.97%
9	0.37	2.94%	0.07%	1.69%	90.85%	91.23%	92.12%

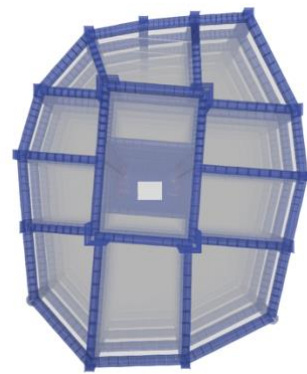
The use of SLB devices leads to a stiffer structure, as demonstrated by the period reduction of the first three natural periods of the building. Results given in Table 7.10 shows that the first and second mode are essentially translational, while the third one is torsional.



*Figure 7.34 1<sup>st</sup> mode*



*Figure 7.35 2<sup>nd</sup> mode*



*Figure 7.36 3<sup>rd</sup> mode*



The fundamental period of the structure with SLB is 2.49 seconds, while 90% of the participating mass ratio is achieved in all directions considering the first 9 natural modes of vibration of the structure.

### 7.6.3 Service Level Earthquake evaluation

The next step consists of verifying the structure to the Service Level Earthquake according to MOC-CFE requirements. The interstory-drift results, given in Figure 7.37, are obtained with a response spectrum analysis using the SLE site spectrum introduced in Figure 7.5 and considering the load combinations defined in section 7.3.

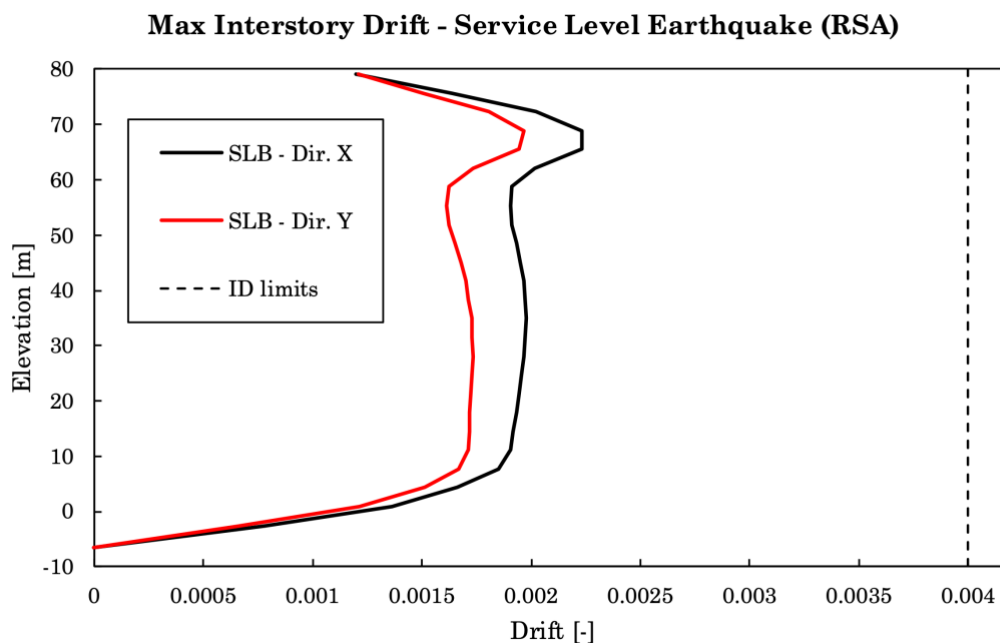


Figure 7.37 Max Interstory Drift at Service Level Earthquake (RSA)

### 7.6.4 Reinforcement design

This paragraph describes the reinforcement design of structural elements (beams, columns and decoupled walls), that has been carried out after the verification of the structure at Service Level Earthquake. In this case, the steel reinforcement design has been performed with the PBSB approach, rather than using the amount of reinforcement obtained from a RSA with the inelastic design spectrum. The reinforcement is initially designed considering the maximum stresses in structural

elements due to gravity loads and SLE seismic loads combinations (see section 7.3) and taking into account the minimum reinforcement required for RC beams and columns according to ACI 318-19. The initial design under SLE seismic loads ensures that structural elements meet the local acceptance criteria for Service Level Earthquake, i.e., plastic rotation is less than immediate occupancy. The structure is then verified with nonlinear time history analyses at Maximum Considered Earthquake level and for those structural elements that do not satisfy the local acceptance criteria (e.g., plastic rotation greater than collapse prevention) the amount of steel reinforcement has been increased. The variation of steel reinforcement requires to perform again the nonlinear time history analyses at MCE level, so the design methodology is iterative. The procedure is repeated until the code requirements regarding global and local acceptance criteria are met.

Table 7.11 contains the amount of steel reinforcement for beam sections obtained by the iterative design procedure. The coefficients  $\rho_{s,bot}$  and  $\rho_{s,top}$  represent the bottom and top geometric percentage of reinforcement, defined as:

$$\rho_{s,bot} = \frac{A_{s,bot}}{A_c} \quad \rho_{s,top} = \frac{A_{s,top}}{A_c} \quad (7.7)$$

where  $A_c$  is the concrete area of the section.

*Table 7.11 Reinforcement design for structure with SLB - Beam sections*

Section	$A_c$	$\Phi$	Num. of bars	$A_{s,bot}$	$A_{s,top}$	$\rho_{s,bot}$	$\rho_{s,top}$
[-]	[cm <sup>2</sup> ]	[mm]	[-]	[cm <sup>2</sup> ]	[cm <sup>2</sup> ]	[-]	[-]
TR 50X110	5500	25.4	6	30.40	30.40	0.55%	0.55%
TR 55X70	3850	25.4	4	20.27	20.27	0.53%	0.53%
TR 40X100	4000	25.4	4	20.27	20.27	0.51%	0.51%

In this case, the steel reinforcement obtained from the design is constant for the entire length of the beams, thus there is no difference between end and mid part of the structural elements as done for the design Bare frame structure (see section 7.5.4). Furthermore, the geometric percentage of reinforcement is very close to the one obtained by the initially design for gravity loads and SLE seismic loads combinations.

Table 7.12 contains the amount of steel reinforcement for column sections obtained by the iterative design procedure. The coefficient  $\rho_s$  represents the total geometric percentage of reinforcement, defined as:

$$\rho_s = \frac{A_s}{A_c} \quad (7.8)$$

Table 7.12 Reinforcement design for structure with SLB - Column sections

Section	$A_c$	$\Phi$	Num. of bars	$A_{s,tot}$	$\rho_s$
[-]	[cm <sup>2</sup> ]	[mm]	[-]	[cm <sup>2</sup> ]	[-]
COL 70X125	8750	25.4	20	101.34	1.16%
COL 70X150	10500	25.4	24	121.61	1.16%
COL 80X175	14000	32.3	28	229.43	1.64%
COL 90X100	9000	25.4	20	101.34	1.13%
COL 90X125	11250	25.4	24	121.61	1.08%
COL 90X150	13500	32.3	20	163.88	1.21%
COL 90X175	15750	32.3	36	294.98	1.87%
COL 100	7854	25.4	16	81.07	1.03%
COL 120	11310	25.4	24	121.61	1.08%
COL 140	15394	32.3	24	196.66	1.28%
COL L 70X150	16100	25.4	39	197.62	1.23%
COL L 70X180	20300	32.3	51	417.89	2.06%
COL L 80X180	22400	32.3	67	549.00	2.45%

### 7.6.5 MCE analyses results

This paragraph shows the results obtained with nonlinear time history analyses at MCE level after the reinforcement design of structural elements. In this case, the damping matrix has been calculated following the *Rayleigh damping method*, as described in paragraph 6.3.1, as a linear combination of the stiffness matrix  $\mathbf{K}$ , scaled by a coefficient  $c_K$ , and the mass matrix  $\mathbf{M}$ , scaled by a second coefficient  $c_M$  (see eq. (6.3)). The two coefficients  $c_M$  and  $c_K$  of eq. (6.3) have been computed setting a same modal damping ratio ( $\xi_i = 5\%$ ) at two different natural periods of the structure, that correspond to the first modal period and the period required to achieve 90% mass participation in all the directions. It is important to highlight, as done for bare frame structure, that the MCE structural model is characterized by specific effective stiffness values, that are different from the ones used in the SLE model. Therefore, the

coefficients  $c_M$  and  $c_K$  need to be calibrated according to the modal analysis results of MCE structural model.

Modal Load Case

Viscous Proportional Damping

☐ Direct Specification
 ☒ Specify Damping by Period
 ☐ Specify Damping by Frequency

☐ Specify as Period Ratio, T/T\_mode, for This Mode

	Period	Frequency	Damping
First	2.917 sec	cyc/sec	0.05
Second	0.429 sec	cyc/sec	0.05

Additional Modal Damping

☐ Include Additional Modal Damping

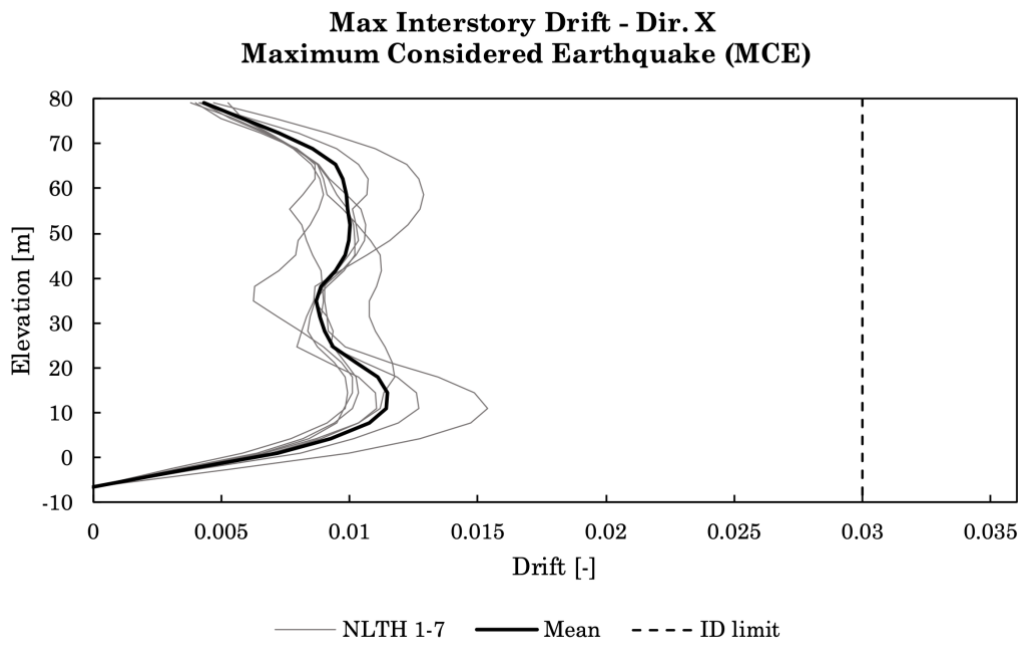
☐ Maximum Considered Modal Frequency

Modify/Show Modal Damping Parameters...

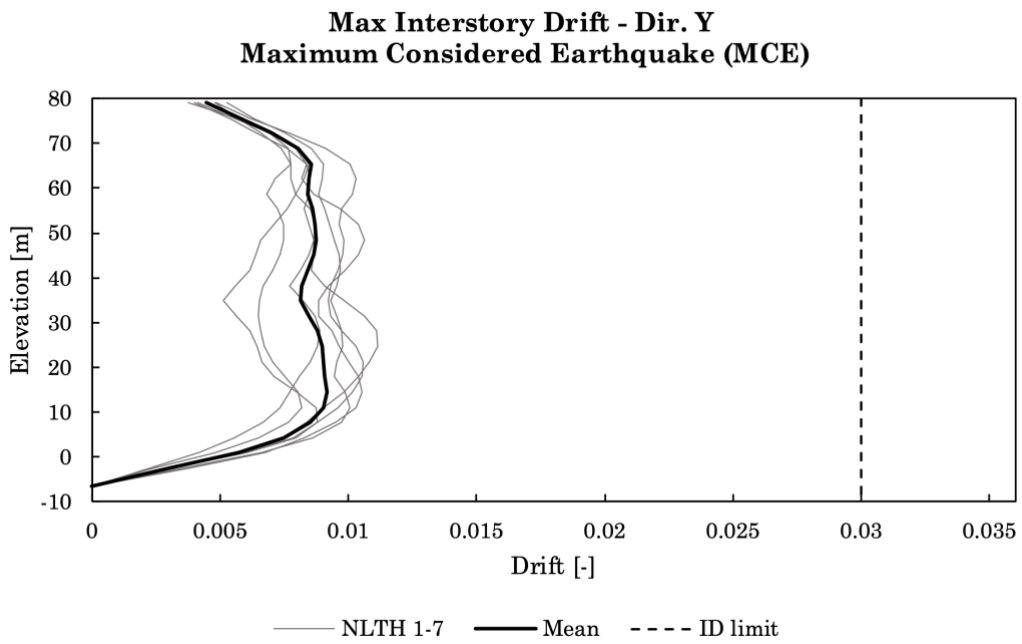
OK Cancel

Figure 7.38 Damping coefficients for Nonlinear time history analysis - ETABS

A set of 7 seismic signals has been used for performing the nonlinear time history analyses, thus, as described in section 7.3.2.2, the mean values of results has been considered to evaluate global and local acceptance criteria. Figure 7.39 and Figure 7.40 show the maximum interstory drift results at MCE level.



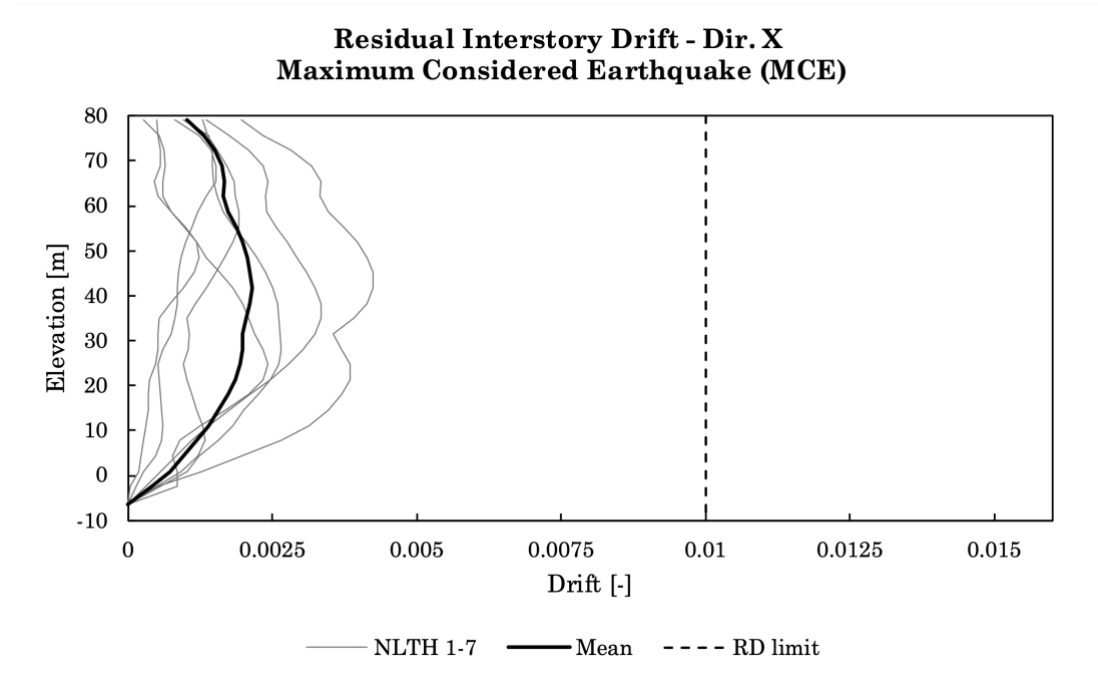
*Figure 7.39 Max interstory Drift at MCE level - Dir. X*



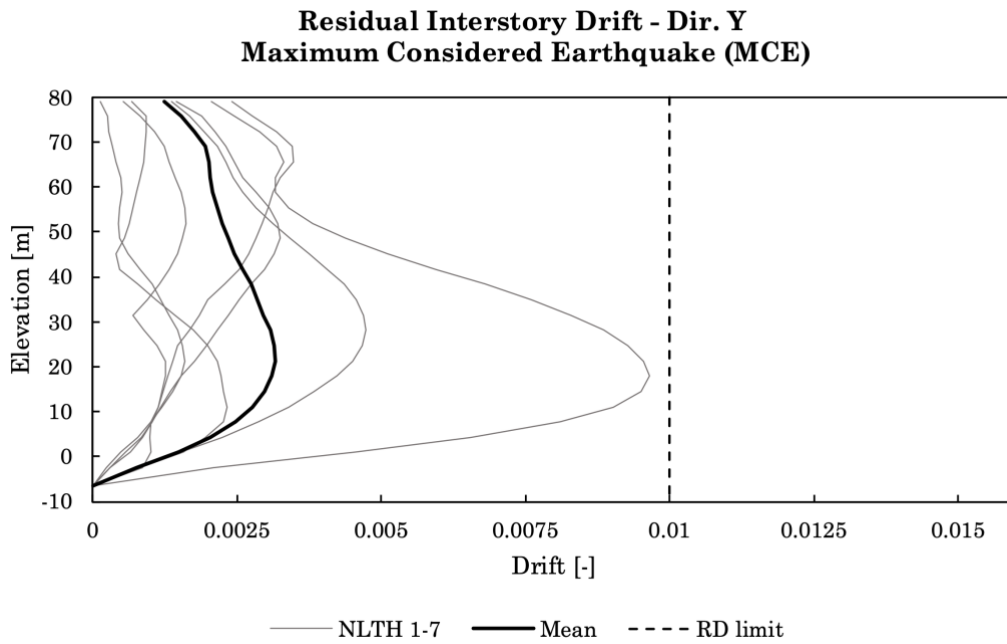
*Figure 7.40 Max Interstory Drift at MCE level - Dir. Y*

The maximum interstory drift is lower than limit in both directions, so the MOC-CFE requirements are satisfied.

The mean values of residual interstory drift ratio obtained from the analyses, according to the TBI-Guideline (see section 7.2.1), shall not exceed 0.01 for protecting the building against excessive post-earthquakes. Figure 7.39 and Figure 7.40 show the residual interstory drift results at MCE level.



*Figure 7.41 Residual Interstory Drift at MCE level - Dir. X*



*Figure 7.42 Residual Interstory Drift at MCE level - Dir. Y*

The residual interstory drift ratios are lower than limit in both directions, so the TBI-Guidelines requirements are satisfied. In conclusion, the results of nonlinear time history analyses at MCE level meet the global acceptance criteria.

Lastly, it is necessary to verify that the structure meets the local acceptance criteria. Therefore, plastic rotations in structural elements (beams and columns) and horizontal displacements in SLB devices need to be lower than Collapse Prevention (CP) value. Numerical acceptance criteria for beams and columns, as described in section 7.2, are taken from ASCE 41-13, while the maximum horizontal displacement for SLB devices is 60 mm<sup>2</sup>.

Table 7.13 shows the maximum and mean demand on capacity ratios for CP of each structural element. The maximum D/C ratio is calculated on the results of the single nonlinear time history analysis, while the mean D/C ratio is calculated on the results of the entire set of accelerograms.

---

<sup>2</sup>Maximum displacement is calibrated on the basis of the latest experimental tests conducted on 4<sup>th</sup> generation of SLB device

Table 7.13 Mean and Maximum D/C ratios for Collapse Prevention (CP) - Structure with SLB

Element	Mean D/C for CP	Max D/C for CP
[-]	[-]	[-]
Beam	0.386	0.664
Column	0.132	0.269
SLB device	0.626	0.877

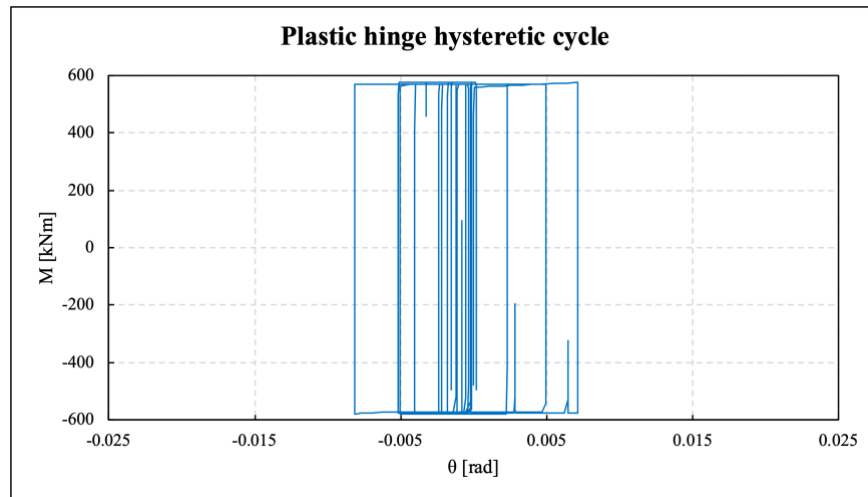


Figure 7.43 Example of plastic hinge hysteretic cycle

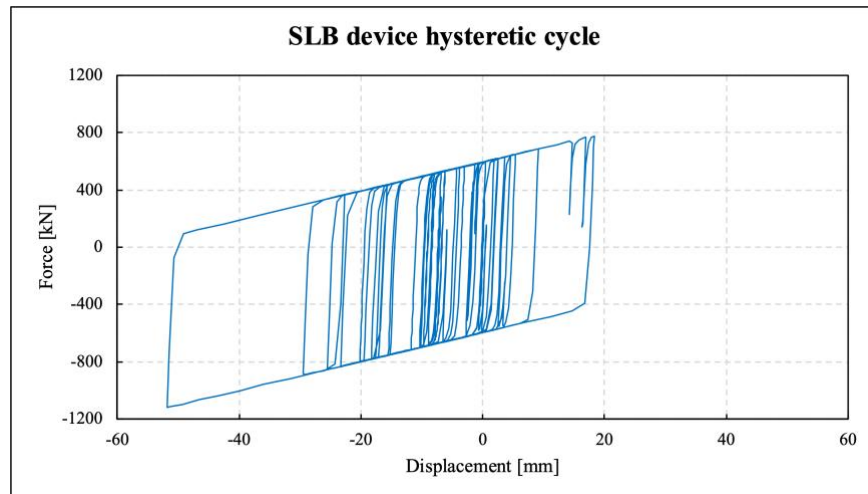


Figure 7.44 Example of SLB device hysteretic cycle



## 7.7 Comparison of Bare frame structure and Structure with SLB

This section presents a comparison between the two structures, with the aim to highlight pros and cons of the two proposed solutions. In particular, the comparison is conducted considering both the structural behavior and the economic costs of the structures, showing the benefits provided by the SLB devices.

### 7.7.1 Structural behavior comparison

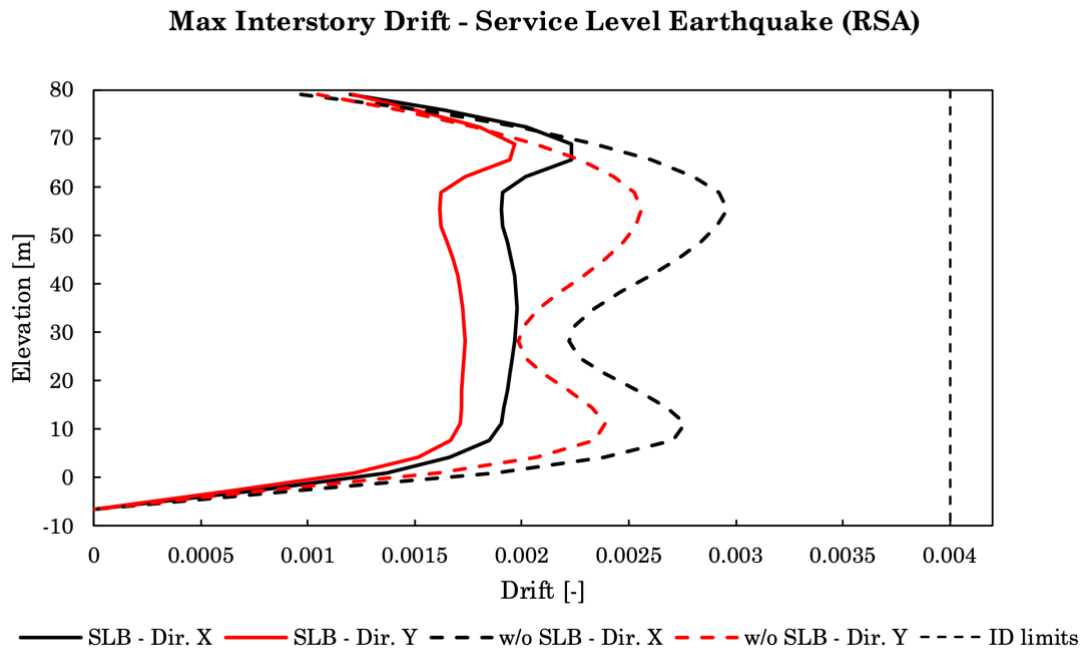
Firstly, in Table 7.14 are shown the modal analysis results of the two structures obtained by the Service Level Earthquake models.

*Table 7.14 Modal analysis results comparison*

Mode	Period	Period	Period	Participating Mass Ratio ( $m_x, m_y, r_z$ )			Participating Mass Ratio ( $m_x, m_y, r_z$ )		
	w/o SLB	with SLB	reduction	Structure w/o SLB			Structure with SLB		
[-]	[s]	[s]	[-]	[-]	[-]	[-]	[-]	[-]	[-]
1	3.32	2.49	25.0%	34.07%	28.08%	14.66%	47.03%	3.84%	23.09%
2	3.23	2.25	30.4%	28.44%	45.77%	1.36%	9.59%	61.99%	2.50%
3	2.51	2.01	20.0%	12.87%	2.21%	61.88%	14.33%	8.47%	52.38%

The use of SLB devices implies a significant stiffening of the structure, as described in the previous sections and confirmed by the period reduction of the first three vibration modes. In addition, it is important to remark that, although the SLB system (device and decoupled concrete wall) has been placed in the central frames of the structure, so very close to the stiffness center of gravity, the first two modal shapes are still translational as noted in section 7.6.2. This aspect is very important since, as described in the previous paragraphs, a torsional fundamental mode of vibration could lead to major stresses due to torsion of the building under seismic loads.

Figure 7.45 and Table 7.15 show the interstory drift results at Service Level Earthquake for the two structures.



*Figure 7.45 Max Interstory Drift - Service Level Earthquake (RSA)*

The use of SLB devices involves a significant reduction of the interstory drift ratios, which is calculated for each story with the following expression:

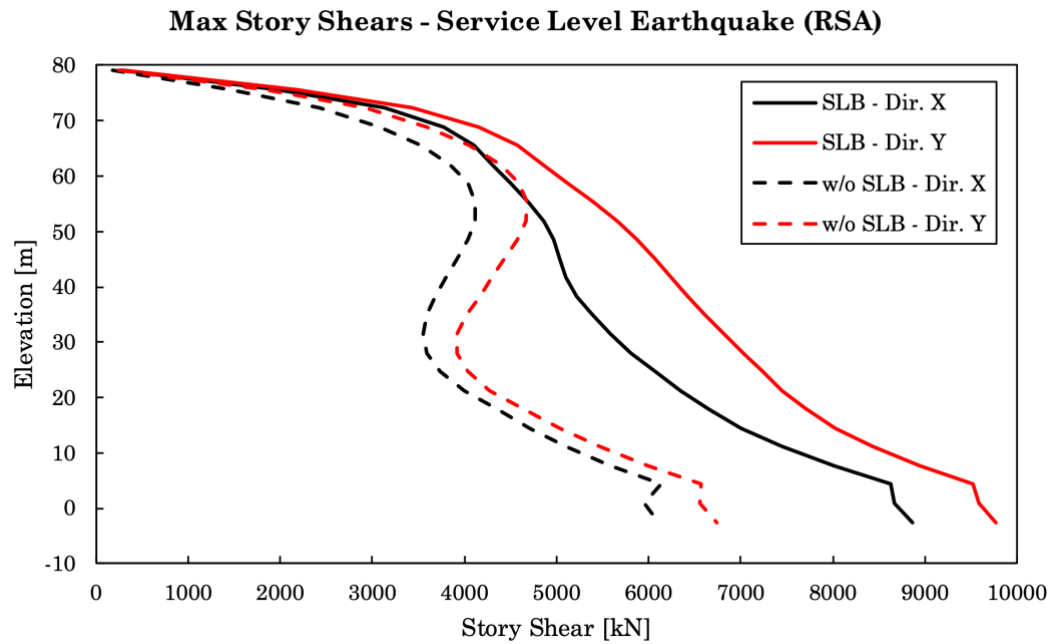
$$ID_{red} = \frac{ID_{w/o\ SLB} - ID_{with\ SLB}}{ID_{w/o\ SLB}} \quad (7.9)$$

The reduction of the interstory drift, calculated with the eq. (7.9), is given in Table 7.15.

Table 7.15 SLE Interstory Drift comparison

Story	Elevation	Interstory drift w/o SLB		Interstory drift with SLB		Interstory drift reduction	
		Dir. X	Dir. Y	Dir. X	Dir. Y	Dir. X	Dir. Y
[-]	[m]	[-]	[-]	[-]	[-]	[-]	[-]
Story25	79.1	0.000967	0.001046	0.001196	0.001209	-23.7%	-15.6%
Story24	75.7	0.001536	0.001431	0.001638	0.001505	-6.6%	-5.2%
Story23	72.3	0.001988	0.00178	0.002021	0.001804	-1.7%	-1.3%
Story22	68.9	0.002339	0.00206	0.00223	0.001966	4.7%	4.6%
Story21	65.5	0.002602	0.002271	0.002229	0.001945	14.3%	14.4%
Story20	62.1	0.0028	0.002429	0.002015	0.001734	28.0%	28.6%
Story19	58.7	0.002922	0.002528	0.001912	0.001622	34.6%	35.8%
Story18	55.3	0.002959	0.002561	0.001906	0.001614	35.6%	37.0%
Story17	51.9	0.00291	0.002529	0.001909	0.001624	34.4%	35.8%
Story16	48.5	0.002838	0.002474	0.001931	0.001652	32.0%	33.2%
Story15	45.1	0.002731	0.00239	0.00195	0.001679	28.6%	29.7%
Story14	41.7	0.002601	0.002289	0.001964	0.001701	24.5%	25.7%
Story13	38.3	0.002462	0.002179	0.001971	0.001714	19.9%	21.3%
Story12	34.9	0.00234	0.002081	0.001975	0.001726	15.6%	17.1%
Story11	31.5	0.002251	0.002009	0.001974	0.001731	12.3%	13.8%
Story10	28.1	0.002222	0.001984	0.001967	0.001732	11.5%	12.7%
Story9	24.7	0.00227	0.002017	0.001956	0.001728	13.8%	14.3%
Story8	21.3	0.002387	0.002104	0.001944	0.001723	18.6%	18.1%
Story7	17.9	0.002541	0.002223	0.001933	0.00172	23.9%	22.6%
Story6	14.5	0.002675	0.002329	0.001916	0.001715	28.4%	26.4%
Story5	11.1	0.002761	0.00239	0.001904	0.00171	31.0%	28.5%
Story4	7.7	0.002705	0.002338	0.001849	0.001669	31.6%	28.6%
Story3	4.3	0.002382	0.002066	0.001662	0.001514	30.2%	26.7%
Story2	0.9	0.001876	0.001602	0.001366	0.001217	27.2%	24.0%
Story1	-2.5	0.000985	0.000827	0.000782	0.000665	20.6%	19.6%
Base	-6.5	0	0	0	0		

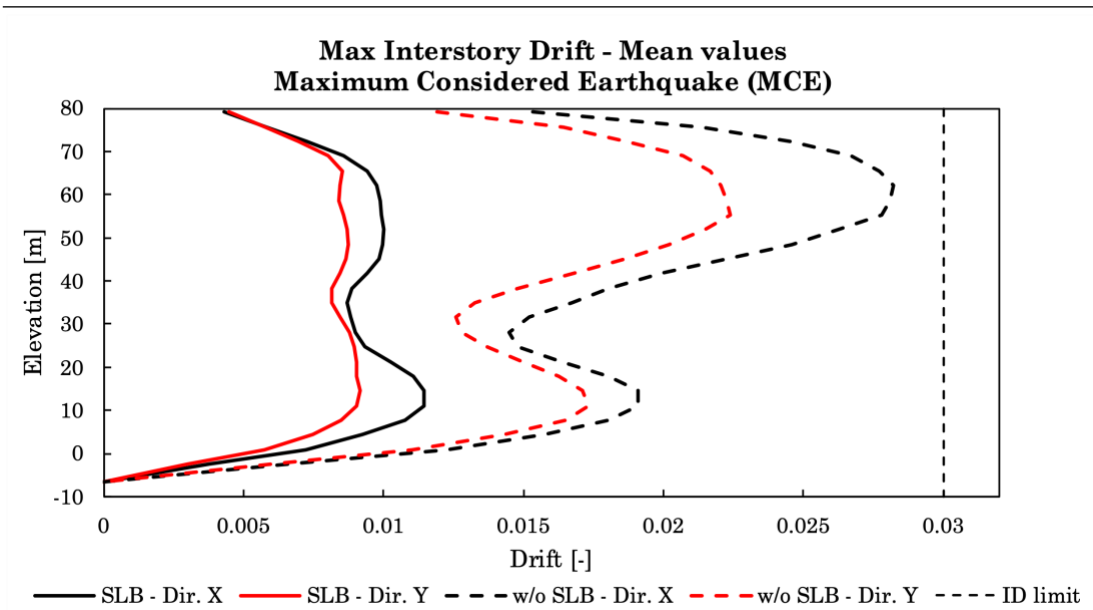
The interstory drift reduction is more significant from story 1 to 20, where the devices are placed, with values between a minimum of 11.5 % and a maximum of 37.0 %. For the upper stories, on the other hand, the reduction is less significant, with even an increase in the interstory drift for the last 3 stories (story 23, 24, 25). This aspect can be justified considering that the translational stiffness of the structure for stories 21 to 25 is practically the same for the two structures, while the story shear is greater for the structure with SLB, as showed in Figure 7.46, that is more rigid. Consequently, a greater value of the interstory drift can be expected for these levels.



*Figure 7.46 Max Story Shears at SLE - Structure with and w/o SLB*

In conclusion, the structure equipped with SLB shows lower values of interstory drift at SLE, that means less damage to both structural elements and non-structural components and, in general terms, lower repair costs in case of a seismic event.

Figure 7.47 and Table 7.16 show the mean values of interstory drift ratio obtained by the nonlinear time history analyses at the MCE level.



*Figure 7.47 Max Interstory Drift - Mean values for MCE level*

*Table 7.16 Max Interstory Drift - Mean values for Maximum Considered Earthquake (MCE)*

Story	Elevation [m]	Interstory drift w/o SLB		Interstory drift with SLB		Interstory drift reduction	
		Mean ID - Dir. X	Mean ID - Dir. Y	Mean ID - Dir. X	Mean ID - Dir. Y	Dir. X	Dir. Y
Story25	79.1	0.0153	0.0119	0.0043	0.0045	71.82%	62.47%
Story24	75.7	0.0214	0.0164	0.0058	0.0058	72.82%	64.87%
Story23	72.3	0.0245	0.0187	0.0073	0.0070	70.46%	62.61%
Story22	68.9	0.0267	0.0207	0.0086	0.0080	67.96%	61.15%
Story21	65.5	0.0277	0.0217	0.0094	0.0085	65.97%	60.58%
Story20	62.1	0.0282	0.0221	0.0097	0.0084	65.47%	61.71%
Story19	58.7	0.0281	0.0223	0.0099	0.0084	64.83%	62.25%
Story18	55.3	0.0278	0.0224	0.0099	0.0086	64.33%	61.64%
Story17	51.9	0.0263	0.0215	0.0100	0.0087	61.87%	59.43%
Story16	48.5	0.0246	0.0202	0.0100	0.0087	59.43%	56.64%
Story15	45.1	0.0223	0.0186	0.0098	0.0087	55.88%	53.52%
Story14	41.7	0.0199	0.0168	0.0094	0.0084	52.69%	49.89%
Story13	38.3	0.0180	0.0148	0.0089	0.0082	50.86%	44.85%
Story12	34.9	0.0167	0.0133	0.0087	0.0081	47.97%	38.63%
Story11	31.5	0.0152	0.0126	0.0088	0.0085	41.78%	32.95%
Story10	28.1	0.0145	0.0128	0.0090	0.0088	37.73%	31.30%
Story9	24.7	0.0148	0.0137	0.0094	0.0090	36.71%	34.48%
Story8	21.3	0.0164	0.0150	0.0103	0.0090	37.29%	39.81%
Story7	17.9	0.0180	0.0163	0.0111	0.0091	38.52%	44.33%
Story6	14.5	0.0191	0.0171	0.0115	0.0092	40.04%	46.45%
Story5	11.1	0.0191	0.0173	0.0114	0.0090	40.13%	47.84%
Story4	7.7	0.0180	0.0165	0.0108	0.0085	40.39%	48.43%
Story3	4.3	0.0158	0.0143	0.0093	0.0075	41.28%	47.99%
Story2	0.9	0.0122	0.0110	0.0072	0.0057	41.19%	48.00%
Story1	-2.5	0.0066	0.0060	0.0037	0.0030	43.04%	50.03%
Base	-6.5	0.0000	0.0000	0.0000	0.0000		

The use of SLB devices leads the greatest benefits for larger earthquakes, such as for the MCE level, when the dissipators are supposed to yield and dissipate energy through their inelastic behavior. Firstly, as noted for the SLE, the structure equipped with SLB shows a significant reduction of the interstory drift (see Table 7.16), which means less

damage to both nonstructural components and – potentially – to structural elements. This last aspect is confirmed considering the collapse prevention (CP) demand on capacity ratios of beams and columns for the two structures at MCE level. In particular, as given in the Table 7.17, the collapse prevention D/C ratios are lower for the structure equipped with SLB, even though the amounts of steel reinforcement in structural elements are considerably smaller if compared to the corresponding ones used in the bare frame structure. This aspect confirms that in the structure with SLB devices the damage is mainly concentrated in the dissipators, while the other structural elements are partially preserved.

Table 7.17 Collapse Prevention D/C ratios for structure with and w/o SLB

Element [-]	Bare frame structure		Structure with SLB	
	Mean D/C for CP [-]	Max D/C for CP [-]	Mean D/C for CP [-]	Max D/C for CP [-]
Beam	0.714	0.999	0.386	0.664
Column	0.238	0.450	0.132	0.269
SLB device			0.626	0.877

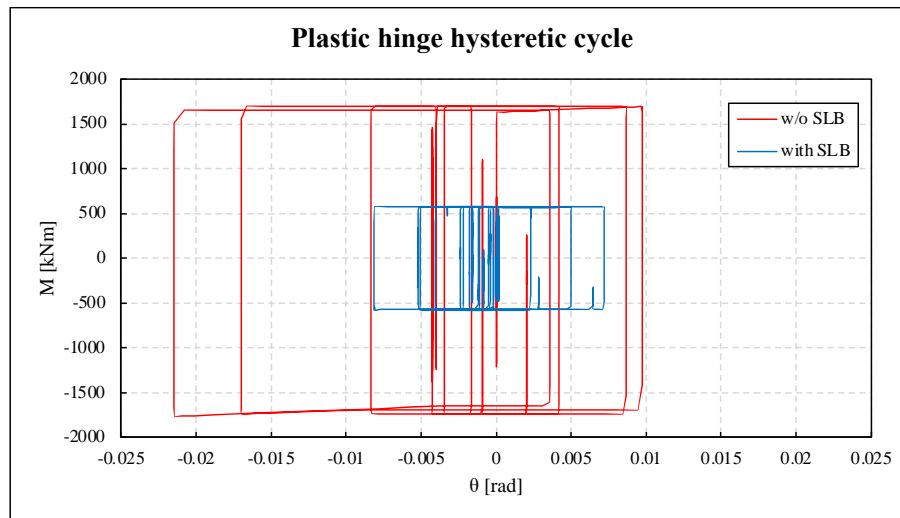
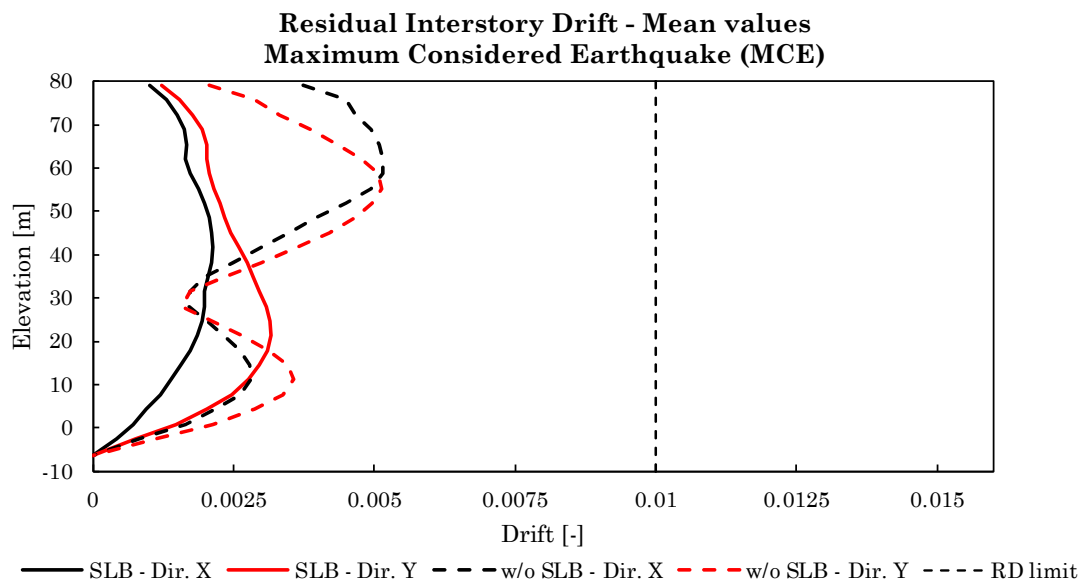


Figure 7.48 Comparison of hysteretic cycles of the most stressed plastic hinges

Lastly, the mean values of residual interstory drift ratios are generally lower for the structure equipped with SLB, as shown in Figure 7.49. This aspect, as explained in section 7.2.1, ensures a better protection against excessive post-earthquakes, in order to provide enhanced performance for tall buildings.



*Figure 7.49 Residual Interstory Drift - MCE*

## 7.7.2 Economic comparison

Paragraph 7.7.1 describes the benefits of the use of SLB devices to the seismic behavior of the structure. However, in order to make the previous results more meaningful, the two proposed solutions need to be compared economically as well. For this reason, Table 7.18 below summarizes the material costs considered for the case study, obtained from a cost estimate of a construction company in Mexico.<sup>3</sup>

*Table 7.18 Material costs for Baia project*

Material	Cost
Concrete C45	199.84 \$/m <sup>3</sup>
Concrete C55	240.75 \$/m <sup>3</sup>
Steel	2.12 \$/kg
SLB device	2,000.00 \$

The first step consists in calculating the quantities of steel and concrete used for the two structures. The amount of concrete used for beams and columns, that is the same for the two solutions because the frame configuration of the initial bare frame structure

<sup>3</sup> It is evident that material costs are subject to continuous variation over time, especially the steel. However, the objective of the comparison is to demonstrate that the two structures have comparable costs, in order to justify also economically the use and benefits of SLB devices

is not changed, has been calculated for each structural element with the following expression:

$$\begin{aligned} V_c &= A_c \cdot \Sigma l_i \\ m_c &= \rho_{conc} \cdot V_c \end{aligned} \quad (7.10)$$

where  $l_i$  is the net length of the i-th structural element having a certain cross section  $A_c$ ,  $\rho_{conc}$  is the concrete density,  $V_c$  and  $m_c$  represent the concrete volume and mass respectively. The calculated amount of concrete is summarized in Table 7.19.

Table 7.19 Amount of concrete for the structures

Section [-]	Total length [m]	$A_c$ [cm <sup>2</sup> ]	$\rho_{conc}$ [ton/m <sup>3</sup> ]	$V_c$ [m <sup>3</sup> ]	$m_c$ [ton]	$m_{c,tot}$ [ton]
TR 50X110	890	5500		490	1175	
TR 55X70	3732	3850		1437	3448	
TR 40X100	268	4000		107	258	
COL 70X125	245	8750		214	514	
COL 70X150	326	10500		343	823	
COL 80X175	72	14000		100	241	
COL 90X100	122	9000		110	264	
COL 90X125	58	11250	2.40	65	156	9298
COL 90X150	119	13500		161	386	
COL 90X175	44	15750		70	168	
COL 100	61	7854		48	115	
COL 120	82	11310		92	221	
COL 140	22	15394		33	80	
COL L 70X150 SD	231	16100		372	893	
COL L 70X180 SD	82	20300		166	398	
COL L 80X180 SD	30	22400		66	159	

The geometric percentage of steel reinforcement for structural elements is obviously different for the two proposed solutions (see Table 7.5 and Table 7.11 for beams, see Table 7.6 and Table 7.12 for columns). Similarly, to what has been done for concrete, the amount of steel used has been calculated as:

$$m_s = \rho_{steel} \cdot (A_s^{mid} \cdot \Sigma l_i^{mid} + A_s^{end} \cdot \Sigma l_i^{end}) \quad (7.11)$$



for the beam, where  $A_s^{mid}$  and  $A_s^{end}$  are respectively the total area of steel reinforcement used in the mid and end sections; while for the columns, where the reinforcement is constant for the entire length of the element, the steel amounts have been calculated as:

$$m_s = \rho_{steel} \cdot A_s \cdot \Sigma l_i \quad (7.12)$$

The calculated steel reinforcement amounts are summarized in Table 7.20 and Table 7.21 for the bare frame structure and in Table 7.22 and Table 7.23 for the structure equipped with SLB devices.

*Table 7.20 Amount of steel reinforcement for bare frame structure - beam sections*

Section [-]	Total length [m]	Total end length [m]	$A_c$ [cm <sup>2</sup> ]	$\rho_l^{end}$ [-]	$A_{s,bot}^{end}$ [cm <sup>2</sup> ]	$A_{s,top}^{end}$ [cm <sup>2</sup> ]	$A_{s,top}^{mid} + A_{s,bot}^{mid}$ [cm <sup>2</sup> ]	$V_s$ [m <sup>3</sup> ]	$\rho_{steel}$ [ton/m <sup>3</sup> ]	$m_s$ [ton]
TR 50X110 0.5%	64	29	5500	0.55%	30	30	61	0.39		3.0
TR 50X110 1%	164	65	5500	1.01%	56	56	61	1.33		10.4
TR 50X110 1.5%	228	90	5500	1.64%	90	90	61	2.46		19.3
TR 50X110 2%	378	148	5500	2.09%	115	115	61	4.79		37.6
TR 50X110 2.5%	56	29	5500	2.68%	147	147	61	1.01		8.0
TR 55X70 0.5%	676	238	3850	0.53%	20	20	41	2.74		21.5
TR 55X70 1%	669	238	3850	1.05%	41	41	41	3.68		28.9
TR 55X70 1.5%	902	324	3850	1.58%	61	61	41	6.29	7.85	49.3
TR 55X70 2%	898	358	3850	2.13%	82	82	41	8.05		63.2
TR 55X70 2.5%	586	226	3850	2.55%	98	98	41	5.90		46.3
TR 40X100 0.5%	22	9	4000	0.51%	20	20	41	0.09		0.7
TR 40X100 1%	39	15	4000	1.01%	41	41	41	0.22		1.7
TR 40X100 1.5%	120	60	4000	1.52%	61	61	41	0.97		7.6
TR 40X100 2%	50	24	4000	2.05%	82	82	41	0.50		3.9
TR 40X100 2.5%	38	18	4000	2.46%	98	98	41	0.44		3.4

*Table 7.21 Amount of steel reinforcement for bare frame structure - column sections*

Section [-]	Total length [m]	$A_c$ [cm <sup>2</sup> ]	$\rho$ [-]	$A_{s,tot}$ [cm <sup>2</sup> ]	$V_s$ [m <sup>3</sup> ]	$\rho_{steel}$ [ton/m <sup>3</sup> ]	$m_s$ [ton]
COL 70X125	245	8750	2.78%	243	5.95		47
COL 70X150	326	10500	3.75%	393	12.84		101
COL 80X175	72	14000	4.45%	623	4.46		35
COL 90X100	122	9000	2.03%	182	2.23		18
COL 90X125	58	11250	2.62%	295	1.71		13
COL 90X150	119	13500	2.67%	361	4.29		34
COL 90X175	44	15750	3.95%	623	2.76	7.85	22
COL 100	61	7854	1.94%	152	0.93		7
COL 120	82	11310	1.34%	152	1.24		10
COL 140	22	15394	3.19%	492	1.06		8
COL L 70X150	231	16100	1.73%	279	6.44		51
COL L 70X180	82	20300	2.70%	549	4.48		35
COL L 80X180	30	22400	3.04%	680	2.01		16

Table 7.22 Amount of steel reinforcement for structure with SLB - beam sections

Section	Total length	$A_c$	$\rho_l$	$A_{s,bot}$	$A_{s,top}$	$A_{s,tot}$	$V_s$	$\rho_{steel}$	$m_s$
[-]	[m]	[cm <sup>2</sup> ]	[-]	[cm <sup>2</sup> ]	[cm <sup>2</sup> ]	[cm <sup>2</sup> ]	[m <sup>3</sup> ]	[ton/m <sup>3</sup> ]	[ton]
TR 50X110 0.5%	890	5500	0.55%	30	30	61	5.41		42.5
TR 55X70 0.5%	3732	3850	0.53%	20	20	41	15.13	7.85	118.8
TR 40X100 0.5%	268	4000	0.51%	20	20	41	1.09		8.5

Table 7.23 Amount of steel reinforcement for structure with SLB- column sections

Section	Total length	$A_c$	$\rho$	$A_{s,tot}$	$V_s$	$\rho_{steel}$	$m_s$
[-]	[m]	[cm <sup>2</sup> ]	[-]	[cm <sup>2</sup> ]	[m <sup>3</sup> ]	[ton/m <sup>3</sup> ]	[ton]
COL 70X125	245	8750	1.16%	101	2.48		19
COL 70X150	326	10500	1.16%	122	3.97		31
COL 80X175	72	14000	1.64%	229	1.64		13
COL 90X100	122	9000	1.13%	101	1.24		10
COL 90X125	58	11250	1.08%	122	0.70		6
COL 90X150	119	13500	1.21%	164	1.95		15
COL 90X175	44	15750	1.87%	295	1.31	7.85	10
COL 100	61	7854	1.03%	81	0.50		4
COL 120	82	11310	1.08%	122	0.99		8
COL 140	22	15394	1.28%	197	0.42		3
COL L 70X150	231	16100	1.23%	198	4.57		36
COL L 70X180	82	20300	2.06%	418	3.41		27
COL L 80X180	30	22400	2.45%	549	1.63		13

In addition, Table 7.24 shows the comparison of the reinforcement amounts used for the two structures.

Table 7.24 Reinforcement design comparison - Bare frame structure vs Structure with SLB

Section	Bare frame structure		Structure with SLB		Comparison	
	$m_s$	$m_{s,tot}$	$m_s$	$m_{s,tot}$	$\Delta m_s/m_{s,bare}$	$(\Delta m_s/m_{s,bare})_{tot}$
[-]	[ton]	[ton]	[ton]	[ton]	[-]	[-]
TR 50X110	78		42		46%	
TR 55X70	209		119		43%	
TR 40X100	17		9		51%	
COL 70X125	47		19		58%	
COL 70X150	101		31		69%	
COL 80X175	35		13		63%	
COL 90X100	18		10		44%	
COL 90X125	13	701	6	365	59%	48%
COL 90X150	34		15		55%	
COL 90X175	22		10		53%	
COL 100	7		4		47%	
COL 120	10		8		20%	
COL 140	8		3		60%	
COL L 70X150 SD	51		36		29%	
COL L 70X180 SD	35		27		24%	
COL L 80X180 SD	16		13		19%	

It should be noted that the use of SLB devices allows a 48% reduction in the amount of steel used for beams and columns. However, for the solution with SLB, in the addition to the devices, also the concrete and steel amounts<sup>4</sup> used for the decoupled supporting walls need to be taken into account. Specifically, for each wall (80 in total) the amount of concrete has been evaluated with the eq. (7.10), while for the steel reinforcement has been assumed an amount equal to 100 kg/m<sup>3</sup>, that satisfy the respect of a device-wall capacity design approach.

Finally, considering the material costs in Table 7.18, the following Table 7.25 summarizes the total costs of the two solutions

*Table 7.25 Economic comparison between the two solutions*

<b>Material</b>	<b>Cost</b>	<b>Bare structure</b>	<b>Struc. with SLB</b>
Concrete C45	199.84 \$/m <sup>3</sup>	406,391.98 \$	406,391.98 \$
Concrete C55	240.75 \$/m <sup>3</sup>	443,158.49 \$	443,158.49 \$
Steel	2.12 \$/kg	1,485,174.67 \$	772,767.38 \$
SLB system		- \$	425,423.92 \$
<b>Total</b>		2,334,725.14 \$	2,047,741.77 \$
<b>Difference</b>			-12.29% \$

In conclusion, it is important to remark that the use of SLB devices does not only lead to an improvement in the seismic behavior of the structure, as explained in section 7.7.1, but could also result in an overall cost savings, as for this case study. Thus, Table 7.25 indicates that the structure with SLB results in a cost saving of 12.29%. However, it must be considered that the overall cost considers just the superstructure and does not include the material costs of the slabs, which, assuming that are similar for the two structures, would certainly reduce the costs difference. In any case, the objective of the comparison was to demonstrate that the two structures have comparable costs as explained previously, and this justify also economically the employment of SLB devices.

<sup>4</sup> These amounts, not specifically listed in the previous tables, have been taken into account in the economic comparison in Table 7.25

---

## 8 CONCLUSIONS

The theoretical study of the SLB device and its application in a real case study (see chapter 7) lead to the following conclusions. The device represents an excellent solution for seismic protection of buildings and is particularly advantageous due to its flexibility in covering a wide range of force capacities, that makes it adaptable to different levels of demand. The basic idea behind the SLB device, as described in chapters 3 and 4, is providing local ductility, while avoiding local buckling in a simple, manufactured controlled and cheap way. One particular feature of the SLB device consists in the fact that these devices do not need to be aligned vertically since the current connection of the latest 3<sup>rd</sup> and 4<sup>th</sup> generations with the support does not transfer axial load. Its employment leads to an overall improvement in the seismic behavior of the structure providing a great energy dissipation capacity due to its hysteretic behavior, which generally results in a reduction of interstory drift and in the concentration of most of the structural damage within the device, preserving the remaining structural elements from damage. Consequently, the use of SLB device generally results in economic savings in the eventual repair costs of structural elements and nonstructural components. In addition, as showed in chapter 7, the use of SLB device combined with the structural design using the Performance Based Seismic Design approach can also result in structural material cost savings if compared with the bare frame structure designed using a traditional Response Seismic Analysis approach. In particular, for the case study analyzed in this thesis, that concerns a new reinforced concrete building located in the city of Acapulco, Mexico, the use of SLB devices leads to an interstory drift reduction up to 37.0 % and 73.0 % at SLE and MCE seismic demand, respectively. In addition, their employment in the structure results in an economic cost saving of 12.29%, considering only the structural amount of materials of the superstructure. Lastly, the maximum and mean collapse prevention D/C ratios are lower for the structure equipped with SLB, even though the amounts of steel reinforcement in structural elements are considerably smaller if compared to the corresponding ones used in the bare frame structure (see section 7.7.1). This aspect confirms that in the structure with SLB devices the damage is mainly concentrated in the dissipators, while the other structural elements are partially preserved.

---

## REFERENCES

Alehashem et al., 2008. *Behavior and Performance of Structures Equipped with ADAS & TADAS Dampers (a Comparison with Conventional Structures)*

American Society of Civil Engineers, 2013. *Seismic Evaluation and Retrofit of Existing Buildings*

Anil K. Chopra, 1995. *Dynamics of structures (1<sup>st</sup> edition)*

Bozzo Guillermo, Alva Rodrigo, Gnazzo Massimino, Dávalos Elizabeth, Bozzo Luis M., 2022. *Evaluación del desempeño de tres tipos de disipadores de energía para la protección sísmica de edificios de gran altura*

Bozzo Guillermo, Alva Rodrigo, Chianese Riccardo, Bozzo Luis M., 2022. *Two complex high rise buildings case studies equipped with SLB seismic devices*

Bozzo Guillermo, 2021. *Una nueva generación de disipadores slb “shear link” para el diseño sismorresistente*

Bozzo Luis M, J. Ramirez, J. Bairan, G. Bozzo, E. Muñoz, 2020. *Precast buildings equipped with SLB seismic devices*

Bozzo Luis M., H. Gonzales, M. Pantoja Medina, E. Muñoz, J. Ramirez, 2019. *Modeling, analysis and seismic design of structures using energy dissipators SLB*

Bozzo Luis M., 2019. *Análisis y diseño utilizando disipadores sísmicos tipo SLB*

Computers & Structures, Inc., 2017. *CSI Analysis Reference Manual*

Constantinou, Soong, Dargush, 1998. *Passive Energy Dissipation Systems for Structural Design and Retrofit*

Federal Emergency Management Agency (FEMA), 1997. *NEHRP Guidelines for the seismic rehabilitation of buildings*

Fenwick R.C. et al., 1992. *P-Delta actions in seismic resistant structures*

Franchioni G., Severn RT., Bairrao R., editors, Report No. 7, 2001. *Experimental investigations on semi-active and passive systems for seismic risk mitigation*

- 
- Golesorkhi et al., 2019. *Performance-Based Seismic Design for Tall Buildings*
- Graham H. Powell, 2010. *Modeling for Structural Analysis, Computers and Structures Inc.*
- Hurtado F., Bozzo Luis M., 2008. *Numerical and experimental analysis of a shear-link energy dissipator for seismic protection of buildings*
- Losanno Daniele, 2015. *Optimization of supplemental damping in civil engineering structures*
- Mazhar H. et al., 2021. *Nonlinear Modelling and Analysis of RC Buildings using ETABS*
- Nuzzo Iolanda, Losanno Daniele, Caterino Nicola, Serino Giorgio, Bozzo Luis M., 2018. *Experimental and analytical characterization of steel shear links for seismic energy dissipation*
- Nuzzo Iolanda, Losanno Daniele, Serino Giorgio, Bozzo Luis M., 2015. *A Seismic-resistant Precast r.c. System equipped with Shear Link Dissipators for Residential Buildings*
- Nuzzo Iolanda, Losanno Daniele, Cilento Fabrizia, Caterino Nicola, 2020. *Analytical and numerical modelling of shear-link device for seismic energy dissipation in frame structures*
- Ozcelik et al., 2017. *The development of the buckling restrained braces with new end restrains*
- Pacific Earthquake Engineering Research Center (PEER), 2017. *Guidelines for Performance-Based Seismic Design of Tall Buildings*
- Pantoja M., Flores M., Bozzo L., Gonzales H., 2020. *Numerical analysis and experimental correlation of uncoupled concrete walls incorporating SLB devices*
- Soong T.T., Spencer Jr B.F., 2002. *Supplemental energy dissipation: state-of-the-art and state-of-the-practice*

## ACKNOWLEDGEMENTS

Prima di tutto, vorrei esprimere la mia più profonda gratitudine al mio relatore, Prof. Giorgio Serino, per il costante aiuto e per la grande disponibilità avuti nei miei confronti durante il percorso che ha portato alla stesura di questa tesi. Il suo supporto è stato fondamentale, a lui va tutta la mia riconoscenza per aver sempre creduto nelle mie capacità.

Special thanks to my co-tutor Prof. Luis Bozzo for his availability, for giving me the opportunity to improve my knowledge and my skills working in his great engineering company and for his help to successfully carry out my thesis work. I would like to express all my gratitude to my co-tutor and friend Prof. Rodrigo Alva, it is also for his constant support and advice during these months if today I am at this point. Lastly, I would like to thank Leonardo, Francisco, Guillermo for their help and availability.

Rivolgo i ringraziamenti più importanti alla mia famiglia, in particolare ai miei genitori e a mia sorella che mi sono stati sempre accanto, con l'infinita pazienza che li contraddistingue. Il loro costante supporto ed incoraggiamento è stato fondamentale per il raggiungimento dei miei obiettivi, senza di loro non ce l'avrei mai fatta. Non finirò mai di ringraziarvi per avermi permesso di arrivare fin qui. Ringrazio di cuore la mia fidanzata Alessandra per tutto il tempo che mi ha dedicato, per esserci sempre stata. Un ringraziamento va a tutti i miei amici, specialmente a Italo, Luigi e Valeria, per i tanti momenti di gioia e spensieratezza vissuti insieme in questi anni. Ci tengo a ringraziare tutti i miei colleghi e amici incontrati in questi anni di università, con cui ho condiviso sia momenti di gioia che di difficoltà. Un ringraziamento speciale a Nadir, Giuseppe V. e Domenico, le prime persone che ho avuto il piacere di incontrare e che costantemente mi hanno supportato in questa nuova avventura, con la consapevolezza che senza di loro tutto ciò non sarebbe stato lo stesso. Ringrazio il mio amico e collega Massimo per aver condiviso con me tanti momenti in questo percorso intenso ed entusiasmante. Un ringraziamento va ai miei amici Emanuele e Giuseppe B. per essere stati sempre presenti in questa ultima fase del mio percorso di studi. Un sentito ringraziamento a Michele, con il quale ho condiviso l'intero percorso di laurea triennale e che negli anni si è dimostrato un vero amico.